

See discussions, stats, and author profiles for this publication at: <https://www.researchgate.net/publication/234075344>

# New developments in classical chaotic scattering

ARTICLE *in* REPORTS ON PROGRESS IN PHYSICS · JANUARY 2013

Impact Factor: 17.06 · DOI: 10.1088/0034-4885/76/1/016001 · Source: PubMed

---

CITATIONS

24

READS

284

## 2 AUTHORS:



Jesús M. Seoane  
King Juan Carlos University  
40 PUBLICATIONS 281 CITATIONS

[SEE PROFILE](#)



Miguel A F Sanjuán  
King Juan Carlos University  
265 PUBLICATIONS 2,338 CITATIONS

[SEE PROFILE](#)

# New developments in classical chaotic scattering

Jesús M Seoane and Miguel A F Sanjuán

Nonlinear Dynamics, Chaos and Complex Systems Group, Departamento de Física, Universidad Rey Juan Carlos, Tulipán s/n, 28933 Móstoles, Madrid, Spain

E-mail: [jesus.seoane@urjc.es](mailto:jesus.seoane@urjc.es)

Received 15 February 2012, in final form 21 September 2012

Published 14 December 2012

Online at [stacks.iop.org/RoPP/76/016001](http://stacks.iop.org/RoPP/76/016001)

## Abstract

Classical chaotic scattering is a topic of fundamental interest in nonlinear physics due to the numerous existing applications in fields such as celestial mechanics, atomic and nuclear physics and fluid mechanics, among others. Many new advances in chaotic scattering have been achieved in the last few decades. This work provides a current overview of the field, where our attention has been mainly focused on the most important contributions related to the theoretical framework of chaotic scattering, the fractal dimension, the basins boundaries and new applications, among others. Numerical techniques and algorithms, as well as analytical tools used for its analysis, are also included. We also show some of the experimental setups that have been implemented to study diverse manifestations of chaotic scattering. Furthermore, new theoretical aspects such as the study of this phenomenon in time-dependent systems, different transitions and bifurcations to chaotic scattering and a classification of boundaries in different types according to symbolic dynamics are also shown. Finally, some recent progress on chaotic scattering in higher dimensions is also described.

(Some figures may appear in colour only in the online journal)

## Contents

<b>1. Introduction</b>	2	<i>4.4. Barbanis potential system</i>	18
1.1. Preliminary background	2	<i>4.5. Three hard-disk scattering system</i>	19
1.2. Basic concepts in chaotic scattering	3	<b>5. Chaotic scattering in other physical systems</b>	20
1.3. Regimes in chaotic scattering	5	<i>5.1. Chaotic scattering in billiards</i>	20
1.4. Chaotic scattering sets from an ergodic point of view	6	<i>5.2. Chaotic scattering in driven barriers</i>	23
1.5. Applications	7	<b>6. Fractal dimension in chaotic scattering</b>	25
<b>2. Formalism in chaotic scattering</b>	10	<i>6.1. Definition and utility of the fractal dimension in chaotic scattering</i>	26
2.1. Inverse chaotic scattering	10	<i>6.2. Algorithms to compute the fractal dimension</i>	26
2.2. Chaotic scattering theory	11	<i>6.3. Fractal dimension of the scattering function</i>	27
2.3. Thermodynamic formalism	11	<b>7. Experimental systems with chaotic scattering</b>	29
2.4. Escape rate formalism	12	<i>7.1. Hydrodynamical flows</i>	29
<b>3. Basins in chaotic scattering</b>	13	<i>7.2. Optical systems</i>	31
3.1. Fractal basins	13	<b>8. Effects of weak perturbations in chaotic scattering</b>	33
3.2. Wada basins	14	<i>8.1. Dissipative chaotic scattering</i>	33
<b>4. Representative physical systems that exhibit chaotic scattering</b>	16	<i>8.2. Effect of noise on chaotic scattering</i>	38
4.1. Hénon–Heiles system	16	<b>9. Additional topics on chaotic scattering</b>	40
4.2. Contopoulos system	17	<i>9.1. Time-dependent Hamiltonian systems</i>	40
4.3. Four hill potential system	18	<i>9.2. Bifurcations to chaotic scattering</i>	41
		<i>9.3. Types of boundaries in chaotic scattering</i>	42

9.4. Characterization of chaotic scattering by symbolic dynamics	43		10. Conclusions	49
9.5. Chaotic scattering in higher dimensions	45		Acknowledgments	50
			References	50

## 1. Introduction

### 1.1. Preliminary background

In this review, we provide an account of the most important topics related to the phenomenon of chaotic scattering and we provide information about the new research and findings carried out in the last two decades. Chaotic scattering is a physical phenomenon that can be seen as a manifestation of transient chaos [1–3] or as Tél and Gruiz define in [2], the conservative limit of transient chaos.

A typical scattering process is described by a Hamiltonian of the form

$$H(\mathbf{q}, \mathbf{p}) = H_0(\mathbf{q}, \mathbf{p}) + V(\mathbf{q}), \quad (1)$$

which becomes a free Hamiltonian  $H_0$  at large distances, i.e. such that the potential vanishes fast enough when the particles are separated. It means:  $V(\mathbf{q}) \rightarrow 0$ , as  $\mathbf{q} \rightarrow \infty$ .

As a consequence, particles of the collision move in free motion before and after the collision events with possible rotations or vibrations around their center of mass. These free trajectories are described by the Hamiltonian  $H_0$  [4].

The Hamiltonian  $H$  is supposed to conserve energy because we assume that there is no time-dependent external field in the collision region. When the scattering process involves two or more beams of particles, linear and angular momenta are also conserved. When scattering occurs between a beam and an infinitely heavy solid, only the energy is preserved.

On the other hand, each of the Hamiltonians  $H$  and  $H_0$  define a flow in the phase space  $\mathbf{H} = (\mathbf{q}, \mathbf{p})$  which are denoted by  $\Phi^t$  and  $\Phi_0^t$ , respectively. They leave invariant the energy shells  $H = E$  and  $H_0 = E$ , respectively. This flow  $\Phi^t$  is defined taking into account the differential equation  $\dot{\mathbf{X}} = \mathbf{F}(\mathbf{X})$ . This equation induces a one-parameter continuous group, called the *flow*,  $\mathbf{X} = \Phi^t \mathbf{X}_0$ . This flow is in general a nonlinear function of time  $t$  and of the initial conditions  $\mathbf{X}_0$ .

Here, we briefly explain the dynamics in chaotic scattering. One of the simplest examples of this problem deals with the motion of a particle in a potential  $V(\mathbf{r})$ , where  $\mathbf{r} = (x, y, z)$  is the position vector in which  $\mathbf{r}$  plays the role of  $\mathbf{q}$  according to the previous notation, for which  $V(\mathbf{r})$  is zero outside some finite region from the scattering influence. The particle moves along a straight line sufficiently far from the scattering region. That particle moves towards the scattering region from outside it and interacts with the scatterer leaving the scattering region. This phenomenon can be seen in figure 1. The incident particle has a velocity parallel with respect to the  $x$ -axis at a vertical displacement  $y = b$ . After interacting with the scatterer, the particle moves off to infinity with its velocity vector forming an angle, which can be called  $\phi$ , with respect to the  $x$ -axis. The quantities  $\phi$  and  $b$  are the

scattering angle and the impact parameter, respectively. One of the key problems in scattering phenomena is to investigate the character of the functional dependence between  $\phi$  and  $b$ . The interesting point is that this relationship is qualitatively different for the cases where the dynamic in the scattering region is chaotic or nonchaotic.

We start with a well known example of a 2D potential (see [5]), as shown in figure 2. Figure 3 shows different pictures of the output variable,  $\phi$ , versus the input variable,  $b$ , for the potential given by the equation:

$$V(x, y) = x^2 y^2 \exp[-(x^2 + y^2)]. \quad (2)$$

This potential consists of four hills whose peaks are located at  $(x, y) = (\pm 1, \pm 1)$ , as shown in figure 2. When the energy,  $E$ , of the particle is larger than the maximum potential energy at the peaks, denoted  $E_m$ , the scattering is nonchaotic. This is easy to check by looking at figure 3(a) where we can observe that the relation between the impact parameter,  $b$ , and the scattering angle,  $\phi$ , is a simple smooth curve. This explains very well the nonchaotic behaviour in which the system is not sensitive to the initial conditions. Figure 3(b) shows a numerical plot of the impact parameter,  $b$ , and the scattering angle,  $\phi$ . The speckled appearance in this finite resolution plot qualitatively shows the chaotic motion of the particle shot in this situation. There are several regions in which the scattering angle,  $\phi$ , changes drastically with the impact parameter,  $b$ ; it is difficult to clearly distinguish the different regions. In order to improve the resolution of this picture we pick such a region and, blowing up its horizontal scale to improve the resolution, we see, in figure 3(c), that the speckled regions still remain. Figures 3(d) and (e) show further blowups of the previous pictures and a good resolution of them still fails. These pictures suggest that there are values of the impact parameter,  $b$ , for which the scattering angle,  $\phi$ , varies by an amount of order one on an arbitrarily fine scale in  $b$ . These pictures explain, qualitatively, the chaotic behaviour of the scattering problem for certain values of the energy. It is easily observed that a lot of singularities exist in the discontinuities in the function  $\phi(b)$ , as shown in figures 3(b)–(d). As is well known, to define chaotic scattering requires a fractal set of singularities in the scattering functions, that is, the relation between the impact parameter,  $b$ , and the scattering angle,  $\phi$  [6]. These singularities are caused by the existence of a chaotic saddle [3] in phase space whose location in position space is the interaction region. The singularities in the scattering functions indicate those initial conditions which are placed on the stable manifolds of the chaotic saddle. From the singularity structure of the scattering function, it is possible to reconstruct the important chaotic measures of the saddle [7]. It is noteworthy to indicate that the self-similar structures in the scattering functions are not necessarily a definite indication of true topological chaos in

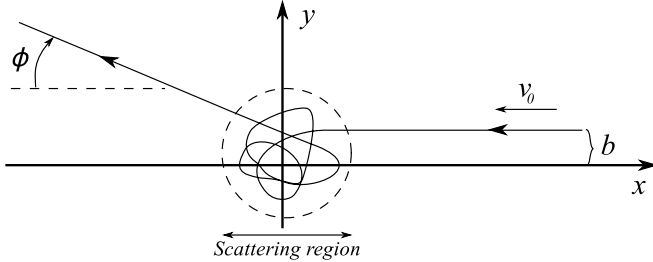


**Figure 1.** Picture of a typical scattering process in physics. The dashed curve denotes the scattering region. The transient chaos is observed in the trajectory inside the scattering region.

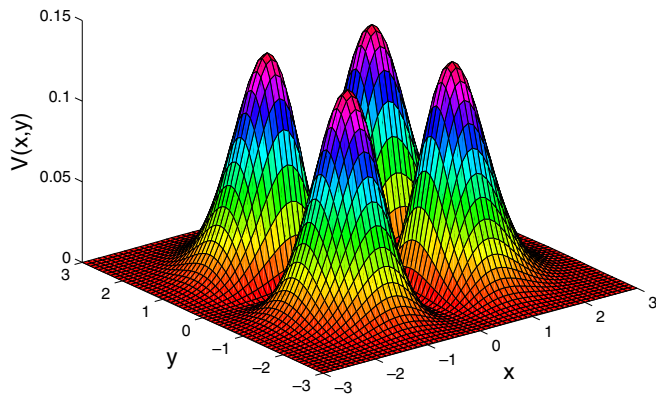


**Figure 2.** Contour plot of the four hill potential. A trajectory inside the four hill potential suffers collisions between the walls and, typically, leaves from the potential influence.

phase space. To demonstrate these difficulties, the authors of [8] construct an example of a compact scatterer without topological chaos, which nevertheless has an infinite number of singularities in the scattering function. Moreover, these singularities are arranged in a self-similar pattern having an infinite number of accumulation points. This structure is not a true fractal [9–12] but this subtle difference is hard to detect. In any case, the hallmark of chaotic scattering is the set of singularities of the scattering function with a fractal character.

The source of the singularity can be seen in principle by following a trajectory from an input at which the scattering function is singular. Such an orbit enters the scattering region, but never exits, continuing to bounce around in the scattering region forever. For instance, in the four hill potential,  $V(x, y) = x^2 y^2 e^{-(x^2+y^2)}$ , for which figure 3 was drawn, an impact parameter value very near to a singular  $b$  value might lead to an orbit that bounces several times around the hills, say 200 times, before exiting from the scattering region. A very small change in the impact parameter  $b$  might then result in say 201 bounces. This small change only makes a small relative change in the number of bounces, from 200 to 201, but the extra bounce totally changes the output parameter, say the scattering angle. This sensitive dependence on initial conditions and the related fractal structure can be seen very clearly in the two-dimensional three-disk problem originally described by Eckhardt in [13] and studied in great detail by Gaspard and Rice (see [14]) and by Poon *et al* in [15].

## 1.2. Basic concepts in chaotic scattering

Here, we describe some of the important and relevant concepts in chaotic scattering.

- **Scattering region.** The region in the physical space in which the particles interact with the potential or the massive object.
- **Escape time.** The time that a particle spends in the scattering region, once it has been shot towards it from outside, before escaping to infinity. This is also called the delay time. The delay time can also be defined as the time that one particle spends in a region that contains the scattering region before exiting. Both definitions are equivalent.

Delay-time statistics are one of the fundamental aspects of chaotic scattering. Imagine we pick  $b$  values at random in some interval. We then examine the resulting orbit for each value and determine the time  $T$  that this orbit spends in the scattering region. The fraction of orbits with a delay time between  $T$  and  $T + dT$  is  $P(T)dT$ . We will see along this review that for large  $T$  the time delay statistics decay exponentially,  $P(T) \sim \exp(-T/\tau)$ , or algebraically,  $P(T) \sim T^{-\alpha}$ , depending of the scattering regime. The distribution of escape times can depend on where the particles are injected [16–18].

- **Differential cross section.** This is a fundamental characteristic of any scattering process; it is a hypothetical area which describes the likelihood of the particles to be scattered. Figure 4 shows this for the four hill problem [6]. The appearance of a multiplicity of singularities is obvious and typically is the hallmark of a chaotic set. In nonchaotic cases, the differential cross section is typically either smooth or its singularities are restricted to a set of dimension zero. Specifically, if one sees a Cantor set of singularities in the cross section, one may safely conclude that the scattering is chaotic; however, if one observes a smooth differential cross section with no singularities, the scattering dynamics may or may not be chaotic. This concept gives some of the most basic phenomenology of chaotic scattering.

- **Delay-time function or scattering function.** This function represents the distributions of the escape times of particles from the scattering region as a function of one of the characteristic parameters of the system. In chaotic scattering problems, the scattering function contains both smooth parts and discontinuities which are characteristics in a fractal set [19]. This can be observed in figure 5. The scattering function  $\Sigma$  [20, 21] is defined by

$$X_{\text{out}} = \Sigma(X_{\text{in}}) = \lim_{t \rightarrow \infty} \Phi_0^{-t/2} \circ \Phi^t \circ \Phi_0^{-t/2}(X_{\text{in}}). \quad (3)$$

This function is interpreted as follows. The point  $X_{\text{in}}$  is taken within the collision region of the phase space and is supposed to belong to an incoming trajectory of the free Hamiltonian  $H_0$ . The purpose of this scattering function is to emulate the collision process undergone by this incoming trajectory and hence to determine the corresponding outgoing trajectory. After a long lapse of time, the point  $\Phi_0^{-t/2}(X_{\text{in}})$  can be taken as the initial

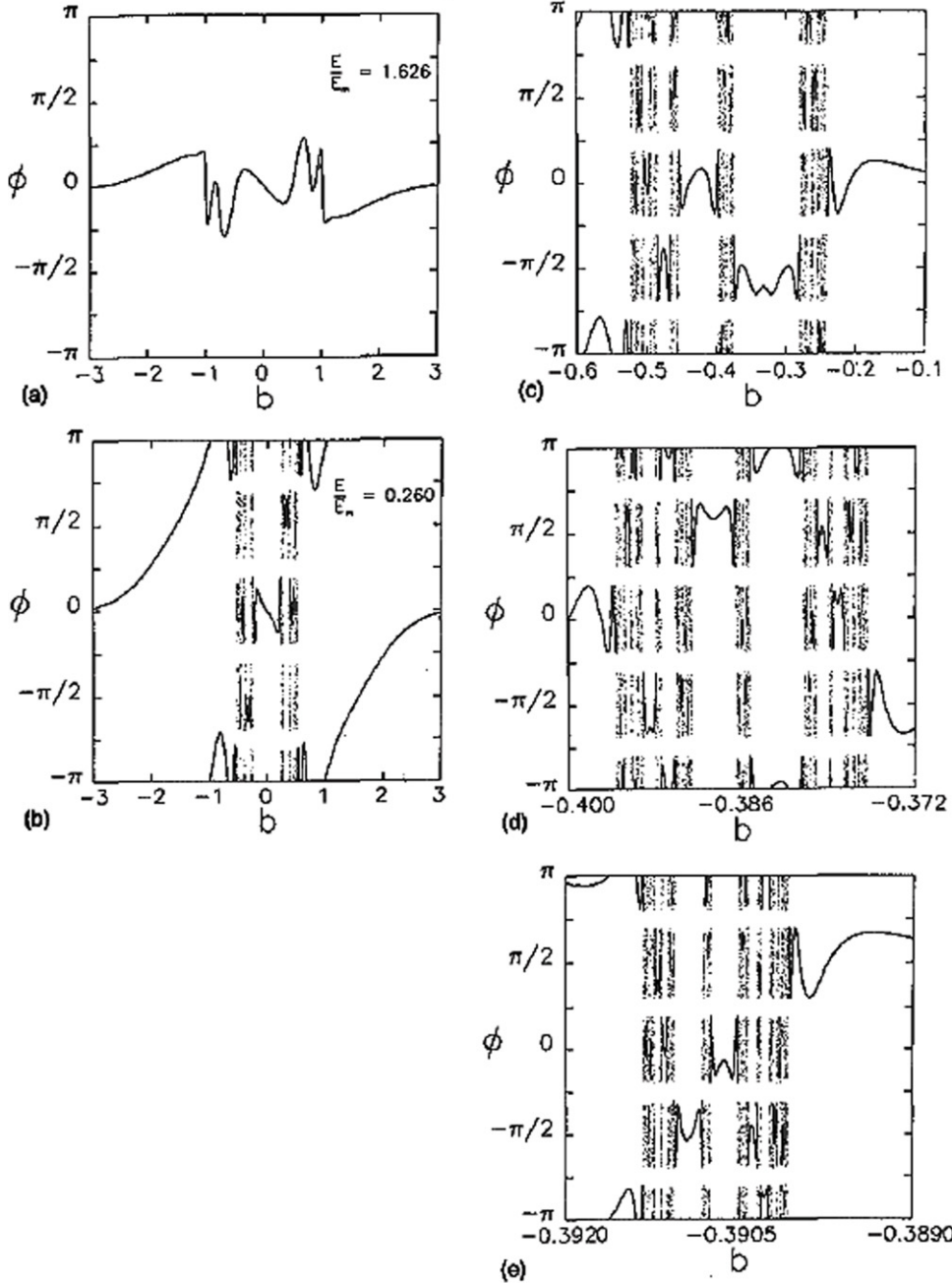


**Figure 3.** Different plots of the scattering angle  $\phi$  versus the impact parameter  $b$  for the four hill potential (a) for  $E > E_m$ , and (b) for  $E < E_m$ . (c), (d) and (e) show successive blowups of a small region in  $b$  for the case  $E < E_m$ . Reproduced with permission from [5]. Copyright 1990 Elsevier.

condition of the actual trajectory of the collision under the full Hamiltonian  $H$ . The final point after the collision will thus be obtained by evolving the initial condition under the full Hamiltonian  $H$  during the time  $t$  (where  $t$  is the number of iterations  $n$ ):  $\Phi^t \circ \Phi_0^{-t/2}(X_{\text{in}})$ .

- **Basin of attraction and exit basin.** The basin of attraction is a set of initial conditions that leads to an attractor or fixed point [22] (in that case the fixed point is a stable point). In the same way, we define the exit basin [23] as the set of initial conditions that lead to a certain exit. A typical picture of this kind of structure is plotted in figure 6.
- **Stable and unstable manifold.** We define stable and unstable manifolds of steady states and periodic orbits of

smooth dynamical systems according to [3]. The *stable manifold* of steady states or periodic orbits is the set of points  $x$  that approaches the steady state or the closed curve traced out by the periodic orbit. Similarly, the *unstable manifold* of a steady state or periodic orbit is the set of points  $x$  that approaches the steady state or the closed curve traced out by the periodic orbit, assuming invertibility if we are dealing with a map. Typically they are denoted by  $W^s$  (the stable manifold) and  $W^u$  (the unstable manifold).

On the other hand [24], given a map  $f$ , the set of initial conditions that converge to the saddle point  $p$  is called the *stable manifold* of  $p$ . In the same way, the unstable

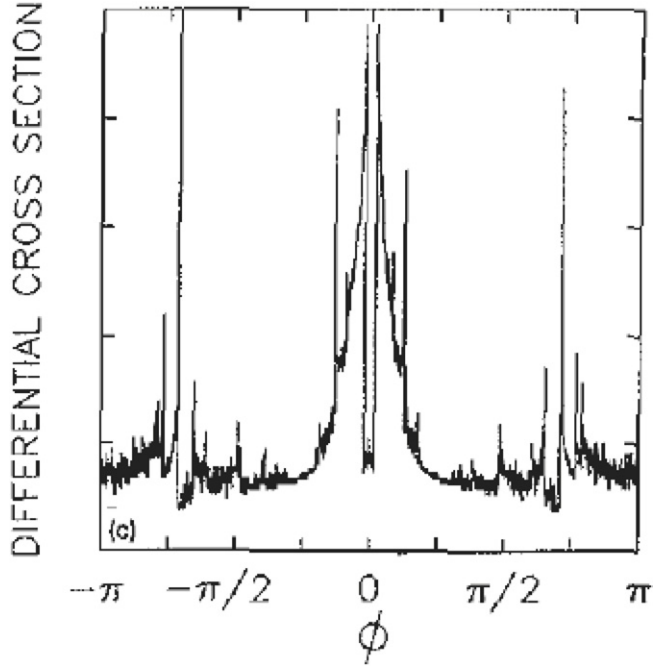


**Figure 4.** Picture of the differential cross section for the four hill potential scattering system. The singularities in the differential cross section typically denote the existence of chaotic motions. Reproduced with permission from [6]. Copyright 1993 American Institute of Physics.

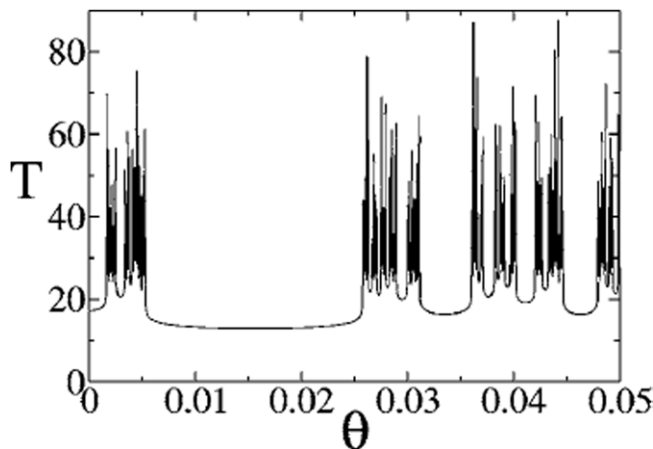


**Figure 5.** Typical delay-time or scattering function in which both smooth parts and singularities are present denoting the sensitivity to the initial conditions, the hallmark of chaotic motions. Reproduced with permission from [19]. Copyright 2003 American Institute of Physics.

manifold of a saddle point  $p$  is the set of points  $v$  such that  $|f^{-n}(v) - f^{-n}(p)| \rightarrow 0$  as  $n \rightarrow \infty$ .

Furthermore, in chaotic scattering problems, the chaotic saddle contains orbits that will never escape from the scattering region for both  $t \rightarrow \infty$  or  $t \rightarrow -\infty$ . The orbits that constitute the chaotic set are unstable periodic orbits [3]. This set is formed by the intersection of its stable and unstable manifold. As these two manifolds are invariant sets, their intersection is also invariant; therefore, every orbit that starts in one point belonging to the chaotic set, never leaves the set. This set is called a *chaotic*

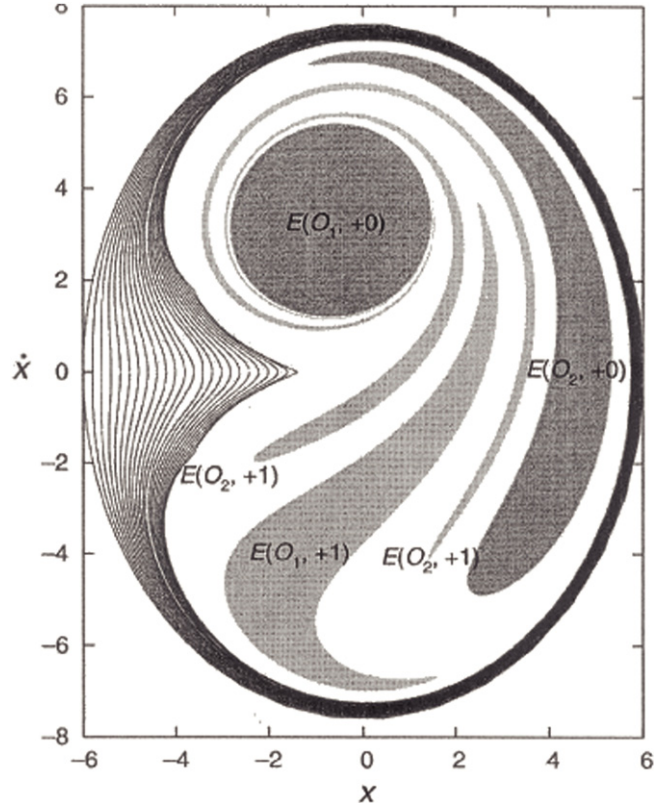


**Figure 6.** This figure represents the typical exit basins in phase space of the Contopoulos system [25].  $O_i$  curves mean the corresponding Lyapunov orbits associated with the corresponding exit. Reproduced with permission from [26]. Copyright 2005 New York Academy of Sciences.

*invariant set*. A plot of the invariant set is shown in figure 7. Furthermore, the chaotic saddle contains lots of nonperiodic orbits as well as unstable periodic orbits.

### 1.3. Regimes in chaotic scattering

The dynamics in chaotic scattering processes can take place basically through two different regimes: hyperbolic and nonhyperbolic. In Hamiltonian systems, regular motions, i.e. motions on various Kol'mogorov–Arnol'd–Moser (KAM) tori [27–31], are also fundamental. Depending on whether there are KAM tori coexisting with chaotic saddles in the phase space, chaotic scattering may be characterized as either *hyperbolic* or *nonhyperbolic*. On the other hand, KAM islands are generally typical of conservative systems. They are unaccessible regions in the phase space where an orbit cannot escape from them [3]. From the chaotic scattering point of view, KAM islands appear in a nonhyperbolic regime. Typically, when the system becomes hyperbolic, KAM islands are destroyed.

In hyperbolic chaotic scattering, all periodic orbits are unstable and there are no KAM islands in the phase space. In this case, the particle-decay law is exponential. To understand this, consider an ensemble of initial particles randomly distributed in the scattering region. As time goes on, particles begin to escape from the region, so the number of particles in the region (or the survival probability of a

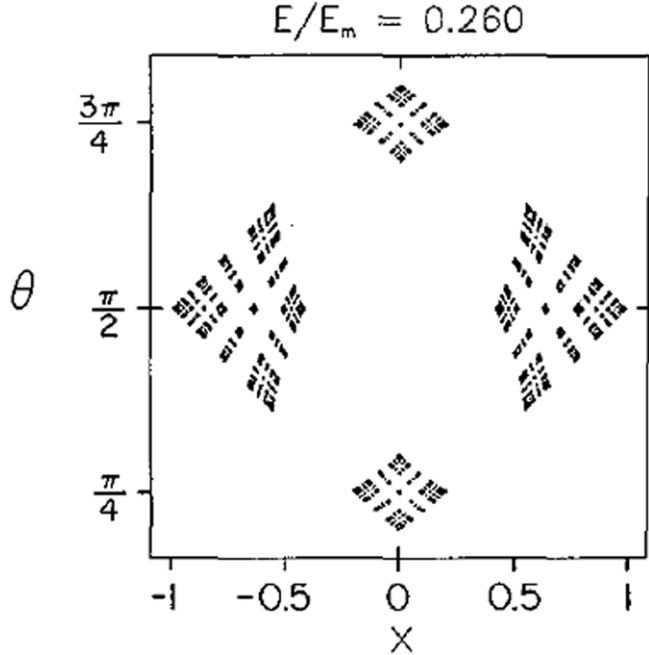


**Figure 7.** Picture of the chaotic invariant set for the four hill potential in the surface of section  $y = 0$ . Reproduced with permission from [6]. Copyright 1993 American Institute of Physics.

particle) decreases with time. When chaotic saddles are the only dynamical invariant sets in the scattering region so that all periodic orbits are unstable, this decrease in the survival probability is necessarily exponential.

On the other hand, in this regime the invariant set is hyperbolic and of zero Lebesgue measure. The scattering function is also defined only on the scattering orbits and on the stable (or unstable) manifolds of the invariant set, at the exclusion of the invariant set itself. The invariant set is not reached from outside except at infinite time.

The invariant set plays an active role in half-collisions as in dissociation processes where the initial conditions are taken inside the domain  $U$ , namely the scattering region.

In nonhyperbolic chaotic scattering, KAM islands coexist with chaotic saddles [30], which typically results in an algebraic decay in the survival probability of a particle in the scattering region. In general, in nonhyperbolic chaotic scattering associated with two degree-of-freedom systems, there exist entire regions of the phase space which do not play any role in the scattering process beside a phase-space exclusion [32]. These regions are the elliptic island of the invariant set, namely  $S$  where trajectories are indefinitely trapped [33, 34]. The time to escape from these regions is infinite. The escape-time function is not defined over these regions of positive area. Therefore, these regions do not belong to the domain of definitions for the scattering function, which is only defined for ongoing trajectories.

In systems with three or more degrees of freedom, there is no topological constraint preventing trajectories escaping from *inside* the invariant tori. This property is at the origin of the *Arnold diffusion*, which is a very slow transport phenomenon taking place in phase-space regions where quasiperiodic motions are abundant [35, 36]. The time to escape from these

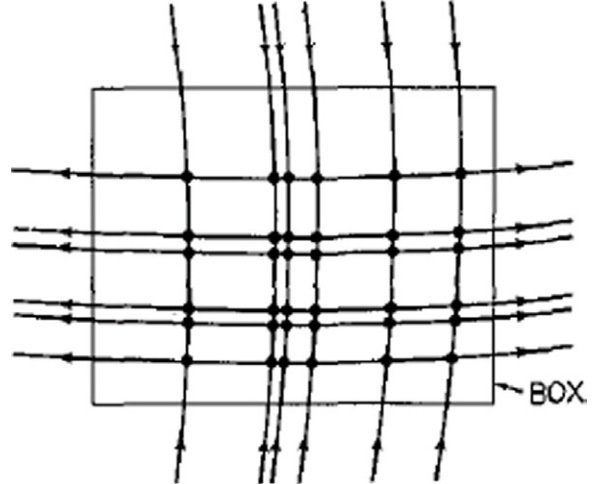


**Figure 8.** Plot of the Poincaré section of a chaotic invariant set. The roughly parallel lines denote the intersections between the stable and unstable manifolds. Reproduced with permission from [6]. Copyright 1993 American Institute of Physics.

regions may often be extremely long without being infinite [14]. As long as the escape time exists, the scattering function also exists.

Trajectories which spend a finite time in the collision region  $U$  and then exit  $U$  are called *scattering orbits*. For such trajectories, the scattering function is well defined because the outgoing trajectory exists as the image of the ingoing trajectory under the map of equation (3); the delay time is finite.

Moreover, there also exist trajectories which are asymptotic to a trapped trajectory and which remain trapped in  $U$  for all future times. This is the case if the ingoing trajectory belongs to the stable manifold of the invariant set  $S$ . In this case, the outgoing trajectory does not exist and the delay time is infinite. On the other hand, by reversing time, we can also discuss the existence of the inverse scattering function  $\Sigma^{-1}$ , which is defined on the scattering orbits but not on the unstable manifold of the invariant set, where the delay time of the reversed process is infinite.

#### 1.4. Chaotic scattering sets from an ergodic point of view

Systems with two degrees of freedom and hyperbolic chaotic invariant sets allow a rather complete theoretical picture. We review here some results for this case in order to introduce in a better way the most important properties of chaotic scattering.

As mentioned in section 1.1, we can regard the chaotic scattering set  $S$  as a chaotic saddle, that is, the intersection of the stable and unstable manifolds of the invariant set of orbits that bounce around in the scattering region. This is illustrated schematically in a Poincaré surface of section in figure 8 (see [37]). Now, assume  $B$  to be a rectangle containing  $S$ . We consider that under the action of the Poincaré map  $f$  [37], all points in  $B$  except for those on the invariant set and its stable manifold leave  $B$  and never return. This part of  $B$  must be mapped out of  $B$ , and its Lebesgue measure, say area, remaining in  $B$  must decay. We randomly sprinkle a large number  $N_0$  of initial points in  $B$ . After  $t$  iterates (becoming

$t$  the time or number of iterations  $n$ ),  $N_t$  points remain. The quantity  $\tau$  of the fraction of orbits with delay time or escape time  $T$ ,  $P(T) \sim \exp(-T/\tau)$ , is:

$$\frac{1}{\tau} = \lim_{t \rightarrow \infty} \lim_{N_0 \rightarrow \infty} \frac{1}{t} \ln \left( \frac{N_0}{N_t} \right). \quad (4)$$

If  $t$  is large, the  $N_t$  points remaining at time  $t$  must have started near the stable manifold. After  $t$  iterates, these points now line up along the unstable manifold. In fact, for any large time  $t$ , one finds that the remaining points essentially lie in thin strips covering the unstable manifold segments in  $B$ . Iterating these strips backward in time to  $t_0$ , the strips along the unstable manifold map to strips along the stable manifold. Since  $f$  is area-preserving and the dimensions of the box  $B$  are of order one, we see that the thickness  $l_i^{(t)}$  of the  $i$ th strip along the stable manifold at time  $t$  is of the same order as the thickness of the unstable manifold strip from which it originates.

We can operationally define the natural measures of a set  $A$  for the stable and unstable manifolds defined previously as

$$\mu_s(A) = \lim_{t \rightarrow \infty} \lim_{N_0 \rightarrow \infty} \frac{N_s(A)}{N_t}, \quad (5)$$

$$\mu_u(A) = \lim_{t \rightarrow \infty} \lim_{N_0 \rightarrow \infty} \frac{N_u(A)}{N_t}, \quad (6)$$

respectively. Here  $N_s(A)$  denotes the number of the remaining  $N_t$  trajectories in  $B$  whose initial conditions lie in  $A$ , while  $N_u(A)$  denotes the number of the remaining  $N_t$  trajectories in  $B$  lying in  $A$  at time  $t$ . Similarly, we define the natural measure of the chaotic set  $S$  itself as

$$\mu(A) = \lim_{t \rightarrow \infty} \lim_{N_0 \rightarrow \infty} \frac{N_\xi(A)}{N_t}, \quad (7)$$

where  $N_\xi(A)$  is the number of orbits which do not leave  $B$  by time  $t$  and which lie in  $A$  at time  $\xi t$ , where  $\xi$  verifies  $0 < \xi < 1$ .

Lyapunov exponents  $\lambda_1 > \lambda_2$  associated with the natural measure on the chaotic invariant set can be defined by considering the Jacobian matrix of the partial derivatives  $Df^t(x)$  of the  $t$  times iterated map  $f^t$  for the  $N_t$  initial points  $x$  whose orbits have not left  $B$  at time  $t$ . The matrix reads

$$\lim_{t \rightarrow \infty} \lim_{N_0 \rightarrow \infty} \langle \text{adj}[Df^t(x)] Df^t(x) \rangle_{N_t}^{1/2t}, \quad (8)$$

where  $\text{adj}$  denotes the adjoint and  $\langle \cdot \rangle_{N_t}$  denotes an average over the  $N_t$  remaining initial conditions, which has eigenvalues  $\exp(\lambda_{1,2})$ . Since  $f$  is area-preserving, then  $\lambda_1 = -\lambda_2$ .

The information dimension of the stable and unstable manifold measures are equal and are given in terms of the Lyapunov exponents and the characteristic decay time  $\tau$  by,

$$d_{s,u} = 2 - \frac{1}{\tau \lambda_1}, \quad (9)$$

as shown in [38, 39].

The information dimension  $d_1$  of the chaotic invariant set is

$$d_1 = d_u + d_s - 2 = 2 \left( 1 - \frac{1}{\tau \lambda_1} \right), \quad (10)$$

where the left-hand side identity results from the fact that  $S$  is the intersection of its stable and unstable manifold. The metric entropy of the natural measure is (see [38, 39]),

$$h_\mu = \lambda_1 - 1/\tau. \quad (11)$$

Pierre Gaspard used this equation to study the connection between the statistical treatment of diffusive transport and the dynamics of chaotic scattering, which is shown in [40].

Multifractal properties of the measure  $\mu$  are readily available from numerical calculations of the set of strip  $l_i^{(t)}$  as shown in [41], where the following partition is introduced:

$$\sum_i l_i^{(t)\beta} \sim \exp[-\beta F(\beta)t]. \quad (12)$$

Here  $F(\beta)$  plays the analogous role of the free energy density and  $\beta$  is similar to the inverse temperature. The function  $F(\beta)$  yields a convenient characterization of ergodic properties of the system. In particular, the decay time is given by

$$F(1) = \tau^{-1}, \quad (13)$$

and the dimension spectrum  $d_q$  of the measure  $\mu$  is given by the solution of:

$$\hat{\beta}(q) F(\hat{\beta}(q)) = q/\tau, \quad (14)$$

where  $\hat{\beta}(q) = q - \frac{1}{2}(q-1)d_q$ . Note that the factor  $1/2$  follows from the fact that the dimension spectrum is the same  $d_q/2$  along both the stable and the unstable manifold due to the Hamiltonian character. The metric entropy is given by the equation:

$$h_\mu = F'(1). \quad (15)$$

In view of equations (9) and (11), the Lyapunov exponent  $\lambda_1$  is obtained as the derivative of  $\beta F(\beta)$  taken at  $\beta = 1$ . Similar results can be obtained using a partition function based on averages of finite-time Lyapunov numbers (for details see [42, 43]).

Another very fruitful approach to the ergodic properties of the chaotic scattering set  $S$  is based on the dense set of periodic orbits embedded in  $S$ . Again, a relevant partition function can be defined, this time as a sum over all the periodic orbits of the given period  $T$ . In principle, all this works well for large values of  $T$ . In practice, it is difficult to obtain orbits with large periods. The periodic orbit formulation is particularly important in problems related to quantum chaotic scattering as has been formulated, for instance, in [44].

### 1.5. Applications

In this section, we discuss some examples of physical applications where chaotic scattering is relevant.

**1.5.1. Celestial mechanics.** One of the first physical situations dealing with chaos was the study of Poincaré of the three-body problem, that is, the interaction of three gravitationally interacting objects. Even the one-dimensional three-body problem [45] has large phase-space regions connected with chaotic scattering. One classical result is due

to Sitnikov [28] who investigated a version of the restricted three-body problem. When two heavy masses move on Kepler ellipses around their center of mass and a third body of negligible mass is restricted to move on the line through the center of mass but perpendicular to the plane of ellipses, Sitnikov was able to rigorously show that the light body motion is chaotic even if it escapes from the vicinity of the two other masses. Another approach was carried out by Petit and Hénon [46]. They considered the case of two small bodies moving around a very heavy mass. In the planar problem, initially one has the two small bodies moving in a common plane on circles of different radii around the central mass. In the case of close encounters complicated motion can take place, but with the exception of a set of initial conditions of zero measure, the small particles separate again. This phenomenon is relevant for the moons of large planets or particles in planetary rings.

The paper by Boyd and McMillan [47] studies the chaotic scattering of an incoming star on a binary system. From the physical point of view the problem is of interest with respect to the heating mechanism for globular clusters. The scattering interaction can result in a more tightly bound binary, thus transferring gravitational energy to kinetic energy.

Other important contributions of chaotic scattering to Celestial Mechanics is that scattering trajectories from time-dependent billiards have been shown to reproduce many aspects of gravitational orbits [48].

**1.5.2. Charged particle trajectories in electric and magnetic fields.** Charged particle motion in electric and magnetic fields is an important aspect of a variety of fields including particle accelerators, electromagnetic wave generators and plasma physics in general. Chernikov and Schmidt discuss in [49] the acceleration of a charged particle in a uniform magnetic field in the presence of large amplitude travelling electromagnetic waves. They show that a very strong and efficient particle acceleration can be produced. Moreover, as a consequence, the process constitutes a chaotic transient of a similar nature to the ones appearing in chaotic scattering. As another example, we mention work on the interaction particles with the central plasma sheet in the magneto tail of the Earth's magnetosphere. The magnetic field in this region can be modeled as:

$$\mathbf{B}(x, z) = B_0 \tanh(z/\delta) \mathbf{x}_0 + B_n z_0, \quad (16)$$

where  $\mathbf{x}_0$  and  $\mathbf{z}_0$  are unit vectors and  $\delta$ ,  $B_0$  and  $B_n$  are constants. For  $|z| \gg \delta$  the field is uniform and particles spiral about the field. Since  $B_n \neq 0$  the guiding center of a particle spiraling along the field can move toward the layer  $|z| \sim \delta$ ; particle motion inside this layer can be chaotic. The dependence of the particle trajectory exiting the layer on the particle motion in the homogeneous field region before entering the region is a chaotic scattering problem. This last result was predicted theoretically. The basis of the solution to this problem is that the particle velocity distribution function for ions would display resonant peaks corresponding to resonances in the chaotic scattering problem. Recent space probe measurements beautifully confirm these predictions, as shown in [50].

**1.5.3. Magnetic field line trajectories.** In plasmas, magnetic field line trajectories, given by the equation

$$\frac{d\mathbf{x}}{ds} = \mathbf{B}(\mathbf{x}) \quad (17)$$

are often important to determine the physical properties of the system. Equation (17) represents a parametric variable measuring distance along the magnetic field line. Since  $\nabla \cdot \mathbf{B} = 0$ , equation (17) is analogous to the motion of a passive particle convected by an incompressible fluid (see section 1.5.4), the work by Lau and Finn [51] on reconnection of three-dimensional magnetic fields in solar plasmas, has shown that chaotic scattering for the conservative dynamical system provides the essential ingredient necessary for understanding these kind of problems. In magnetic reconnection, the topology of the magnetic field configuration changes and magnetic energy is converted into heat. However, in infinitely conducting plasmas, field lines are frozen into the plasma and changes in the topology are then ruled out [52]. Thus, for field lines to reconnect in a highly conductive situation, as in plasma above the surface of the Sun, an energy dissipation mechanism must be found. In [51] the authors consider a situation where typical magnetic lines leave and then return to the surface of the Sun. Some of these lines take longer to return and they find that there is a fractal set which takes forever to return. This is clearly the same phenomenon as mentioned in the previous applications. The necessary dissipation is associated with these infinitely long times to accelerate electrons along these magnetic field lines; electrons can then gain large energies.

**1.5.4. Hydrodynamical processes.** It has long been known that the dynamics of ideal linear vortices is chaotic if the number of participating vortices is greater than three (see [53]). When vortices are started far away from each other, they can come close due to their mutual interaction. For an infinite homogeneous fluid, a bounded configuration for all of the participating vortices does not exist; the distance between some of them will sooner or later grow unboundedly. Such processes are examples of scattering and, in case of four or more vortices, they are typically chaotic. The motion of two pairs of vortices has been studied in detail, for instance in [54]. The authors pointed out that in the course of the interaction, the pairs exchange partners for a finite amount of time. The new pairs have different vorticities and move, as long as they are far away from each other, on approximately circular orbits. Close encounters of these couples strongly perturbs the orbits, but this metastable configuration of two couples can last very long, until a new collision finally leads to an exchange again. This results in the recovery of the two original pairs of vortices, which then leave each other along straight line orbits. This is in complete qualitative agreement with the experiments made in [55]. The motion in the metastable configuration is chaotic and the process exhibits all properties of chaotic scattering mentioned in the previous subsection.

It is also well known that the motion of a passive tracer particle in a simple nonstationary, say time periodic, velocity field can be chaotic, as shown in [56]. Incompressibility

implies the Hamiltonian character of the Lagrangian dynamics. If the nonstationarity of the flow is restricted to a central region outside of which the velocity field is practically stationary, the Lagrangian advection problem in an incompressible fluid provides another example of scattering motion. As pointed out in [57], the tracer dynamics in the space of ideal vortices is integrable (for instance, in the case of three vortices). The transport by the vortical flow generated by a pair of vortices in a wavy-walled channel has been investigated in, among others [58].

Another broad class of problems is related to viscous flows. The passive particle motion in any open incompressible flow can also be an example of chaotic scattering (see [59]). In [60], the authors showed that particles advected by a flow generating a von Kármán street behind a cylinder can be trapped behind the cylinder and exhibit a sensitive dependence on the initial conditions. This is the region where a strange set exists, which is responsible for the chaos of the scattering process. The work [61] investigates the important role of hydrodynamical boundary conditions in making the particle dynamics nonhyperbolic.

**1.5.5. Models of chemical reactions.** In many chemical reactions the number of molecules in the initial and finite states is the same, i.e. no chemical complex is created. Nevertheless, intermediate complexes of finite average lifetime might be present.

In the simplest case, one has initially two atoms, say *A* and *B*, bound in a molecule and a third atom *C* interacting with the other atoms. A reaction takes place when these two components collide with each other. The qualitatively different outcomes of the interaction lead either to the creation of new molecules *AC* or *BC* and free atoms *B* or *A* or the survival of molecule *AB* and atom *C*. This system is an example of a three-body problem; it is not integrable even in restricted geometries like one-dimensional motion.

Rankin and Miller found [62] that small changes in the initial conditions lead to drastic differences in the final states, so that a nonreactive trajectory might exist in the vicinity of a reactive one or vice versa. Later work [63] showed that this property persists to the smallest numerically accessible scales. Noid, Gray and Rice pointed out [64] the underlying fractal structure in the scattering process. The importance of unstable periodic orbits to the understanding of this chemical reaction has been emphasized in [65]. So far, it has become clear that there is typically an infinity of unstable periodic orbits [66] forming the backbone of a nonattracting chaotic set. Most recent investigations use all the tools and concepts on dynamical systems that are used in chaotic scattering problems, as shown in [67]. Since chaotic motion is present as long as all atoms are close to each other, the average lifetime of chaotic trajectories  $\tau$  can be interpreted in classical models of chemical reactions as the average lifetime of the intermediate complex. In this way, the contribution of Koch and Bruhn [68] deals with a model of chemical reactions.

Another interesting development is the control of chaos in chemical reactions (see, for example, [69]), which means that a certain type of nonchaotic motion can be stabilized by

appropriately choosing an external perturbation. This opens up the possibility of stabilizing metastable complexes. On the other hand, the search of periodic orbits for unbounded molecular systems as  $FH_2$  molecular system is carried out in [70].

**1.5.6. Atomic and nuclear physics.** The classical dynamics of two atoms with two electrons has much similarity to that of *A–B–C* chemical reactions with the essential difference that the interaction is of a long range type due the Coulomb force. Much attention has been focused on the problem of Helium. It has long been believed that the classical Helium atom would be unstable, apart from a set of initial conditions of measure zero, and would spontaneously autoionize. Some years ago, Richter and Wintgen [71], and later Yamamoto and Kaneko [72] have shown that the phase space is stable around certain periodic orbits corresponding to, e.g., asymmetrical stretching motions of the two electrons around the nucleus (see [73]). Nevertheless, only a small part of the phase space corresponds to a stable regular motion [71]. Outside this region, there exists an infinite number of unstable periodic orbits embedded in a nonattracting chaotic set; therefore, nearly the entire phase space can be explored by means of scattering processes. As the first investigations indicate [74], the tori around stable periodic orbits can be successfully used for carrying out a semiclassical quantization. In [75] Yuan and Gu investigated the scattering of an electron on a Helium ion.

Another interesting phenomenon connected with both the chemical reactions and atomic processes is the interaction of the constituents with an external electromagnetic field. Even if the motion is simple in the field free case, external driving generically destroys integrability and leads to fragmentation or ionization. The study of such systems has also attracted recent interest and serves as a useful model for the dissociation of molecules (see [76]) or ionization of atoms [77]. The contribution shown in [78] is devoted to a periodically driven scattering system and points out that parabolic orbits also generate a power law decay. Scattering experiments are essential in studying the nuclear structure, too. Therefore, it is natural that chaotic scattering also has relevance to this branch of physics, as shown in [79, 80].

**1.5.7. Atomic transport in optical lattices.** Another interesting application of chaotic scattering, which can be treated from a classical point of view, is the problem of atomic transport in an optical lattice. The transport properties of cold atoms in optical lattices depend on the lattice and atomic parameters and can be very diverse. The optical lattice is a periodic structure of micrometer-sized potential wells, which is created by a laser standing wave made of two counterpropagating laser beams. Most of the experimental and theoretical works on the atomic transport in optical lattices have been done in the context of laser cooling of atoms [81]. A cold atom in an optical lattice can be trapped in the potential wells and it can move over many wavelengths in dependence on whether its energy is below or above the potential barrier. Some of these problems have been studied in [82–88].

There are too many other applications of chaotic scattering which are beyond the scope of this review, since they are not in the context of classical chaotic scattering. For example, the study of chaotic scattering in quantum systems has been carried out by many researchers in [89–92]. In classical hyperbolic scattering, all of the periodic orbits are unstable and the particle-decay law is exponential. As a result, the magnitude squared of the autocorrelation function of the quantum  $S$ -matrix elements is Lorentzian, where the classical escape rate determines its half-width [93, 94]. The Lorentzian form has been observed experimentally [95]. For nonhyperbolic chaotic scattering, there are nonattracting chaotic sets coexisting with KAM tori in the phase space [96], leading to an algebraic particle-decay law. In this case, the fine-scale semiclassical quantum fluctuations of the  $S$ -matrix elements with energy difference is *enhanced* as compared to the hyperbolic case [96]. Scattering echoes of [92] apply not only to quantum mechanics but also to classical mechanics. The application to graphene systems has been the focus of analysis in [97, 98].

Works in other typical fields such as physics of ultracold neutrons [99], radiation field [100], Bose–Einstein condensates [101], open vase-shaped cavity [102], nearest level spacing statistics in open chaotic systems [103], modulation of quantum transport by transient chaos [104] and the beam splitter setup for guided atomic matter waves [105], among others, have been also explored. A dynamical approach to nonequilibrium transport has been carried out from a scattering point of view, which is applicable at both classical and quantum scattering in terms of the Landauer formula [106] for the transport phenomena [107].

## 2. Formalism in chaotic scattering

In this section we are going to provide some of the most important theoretical aspects in chaotic scattering.

### 2.1. Inverse chaotic scattering

The inverse chaotic scattering problem is seen as the task to reconstruct information about the Hamiltonian or the potential from the scattering data without having access to direct observations in the scattering region [108, 109]. However, for chaotic systems this might not be the only useful strategy. If we are interested in properties of the chaotic invariant set, then the reconstruction of first the Hamiltonian and then the chaotic set from it, is a deviation which introduces unnecessary sources of error and ambiguity. Therefore, it is attractive to have methods to extract the properties of the chaotic set directly from the scattering data. Essentially, this means the reconstruction of properties of the horseshoe in some appropriate Poincaré section. The key problem to be solved is to give a connection between the time delay of any trajectory and the number of steps in the Poincaré map that this trajectory has performed. For systems with one degree of freedom and a periodic time dependence, this problem has been investigated in detail and partly solved [110]. Once we know the number of steps a trajectory has performed, we obtain the hierarchical level of any interval of continuity of the scattering functions and this

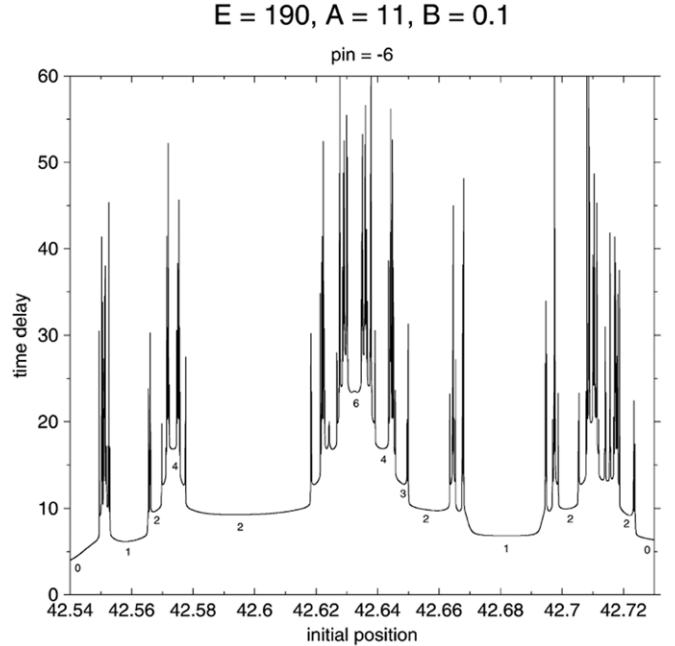


**Figure 9.** Plot of the delay-time function for parameter values  $c = 1$ ,  $\omega = 2\pi$ ,  $A = 11$ ,  $B = 0.1$ ,  $E = 190$ ,  $p_{\text{in}} = -6.0$ . The most important intervals of continuity are labeled by their hierarchical level. Reproduced with permission from [112]. Copyright 2003 Elsevier.

enables us to apply thermodynamic methods to extract all information concerning to chaotic properties of the system as shown in [111].

This general strategy for inverse chaotic scattering problems has been modified by Tapia *et al* [112] in a work dealing with inelastic scattering where one open translational degree of freedom is coupled to one internal vibrational degree of freedom. The complete procedure of this reconstruction method is explained in [112], where the Hamiltonian is:

$$H = \frac{p^2}{2} + H_{\text{in}}(I) + V(q, \phi). \quad (18)$$

For the interaction  $V(q, \phi)$  the asymptotic condition is  $\lim_{t \rightarrow \infty} q \cdot V(q, \phi) = 0$ .

On the other hand, the Hamiltonian of the internal vibration is written as follows:

$$H_{\text{in}} = \omega I - B \frac{I^2}{2}, \quad (19)$$

where  $B$  is the anharmonicity parameter. This Morse model has been used to describe a vibrational degree of freedom of a molecule [113].

Figure 9 shows the typical delay-time function in a chaotic scattering problem which has been obtained from the equation of motion. The parameter values are:  $\omega = 2\pi$ ,  $B = 0.1$  and  $E = H = 190$ . We clearly see a fractal pattern of singularities in the delay function and the task is the reconstruction of its hierarchical organization according to [112]. The results of the reconstruction are shown in figure 10. This figure represents a complicated image of the line of initial conditions. Since we have a chaotic system, this mapping from initial to

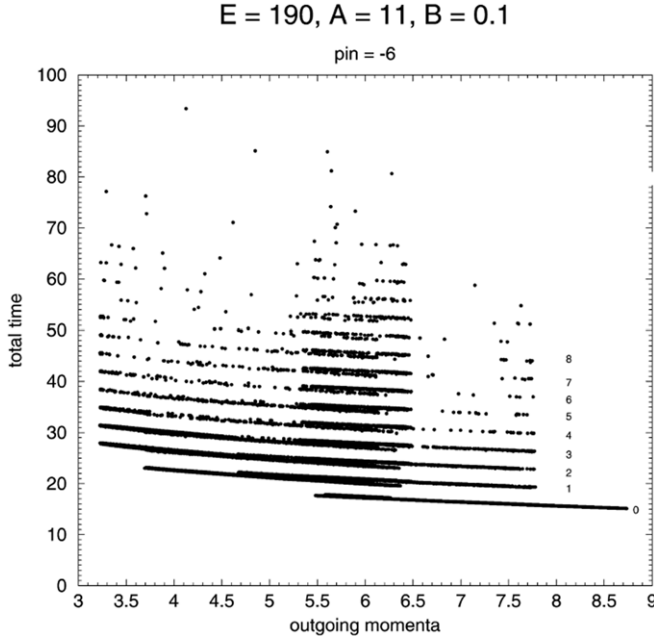


**Figure 10.** This picture shows all occurring values of the total time plotted versus the final momentum for the same trajectories used in figure 9. All points are organized into clearly separated strips which are numbered consequently according to the increasing time value. Reproduced with permission from [112]. Copyright 2003 Elsevier.

final conditions is a fractal map and in reality each strip in the plot has a fractal internal structure. For comparison, the corresponding horseshoe is depicted in figure 11 which is rather complicated [114].

## 2.2. Chaotic scattering theory

After introducing the background on chaotic scattering in previous sections, we provide some theoretical aspects on chaotic scattering [32].

Scattering processes are usually conceived in a statistical approach. For instance, a cross section cannot be determined by a single collision but by a statistical ensemble of the collisions with a uniform distribution of the incoming impact parameters. In this regard, a natural relation appears between scattering theory and the Liouvillian dynamics [32].

Many different processes may be considered in scattering theory, for instance elastic or inelastic collisions [4].

The scattering processes are fundamentally quantum mechanical but in many circumstances the wavelength is so small that the collisions may be considered as classical. If collision processes such as the Coulomb scattering are essentially integrable, on the other hand, the generality of chaotic behaviour in classical mechanics suggest that the majority of collision processes are classically chaotic. When the scattering becomes chaotic the differential cross section may be expected to be a very complex function of the incoming trajectories, while if the scattering is nonchaotic the differential cross section is a smooth curve.

One of the relevant contributions to the classical scattering theory is the contribution of Lax and Phillips [115]. These authors have considered a scattering operator in analogy

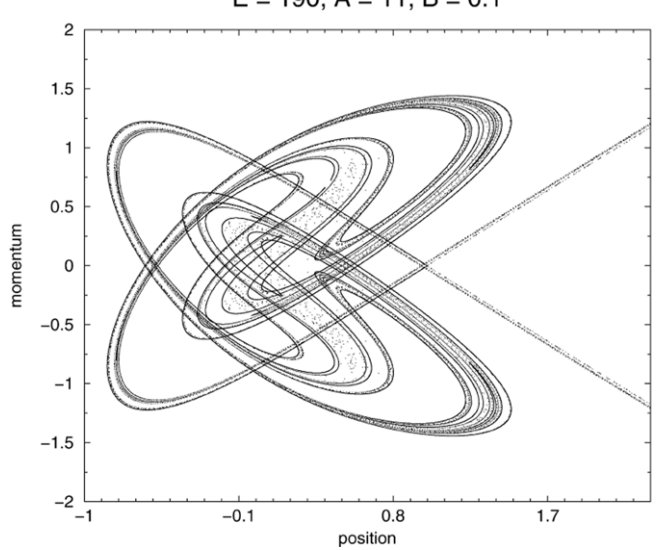


**Figure 11.** This plot shows the horseshoe corresponding to the parameter values used for figures 9 and 10. They are  $c = 1$ ,  $\omega = 2\pi$ ,  $A = 11$ ,  $B = 0.1$ ,  $E = 190$ ,  $p_{in} = -6.0$ . Reproduced with permission from [112]. Copyright 2003 Elsevier.

with the quantum scattering theory. However, in contrast with quantum scattering theory, their work concerns the scattering of statistical ensembles of classical trajectories instead of individual quantum wavefunctions. The theory is developed from the spectral properties of the Koopman operator [116] based on the assumption of a Lebesgue continuous spectrum. Such conditions are satisfied for systems like the disk scatterers, which have a hyperbolic repeller of axiom-A type [117].

Koopman operators are associated with the Hamiltonian flow in the form

$$\hat{U}^t g((X)) = \exp(-\hat{L}t)g(X) = g(\Phi^t X), \quad (20)$$

where Möller-type operators [117] are defined as

$$\hat{W}_\pm = \lim_{\varepsilon \rightarrow \infty} \hat{U}^{\pm t} \hat{U}_0^{\mp t}. \quad (21)$$

A scattering operator is defined as

$$\hat{S} = \hat{W}_+^{-1} \hat{W}_-. \quad (22)$$

This operator maps the ingoing probability density onto the outgoing one in terms of the scattering function of equation (3) and reads

$$f_{out}(X) = \hat{S} f_{in}(X) = f_{in}(\Sigma^{-1} X). \quad (23)$$

## 2.3. Thermodynamic formalism

The thermodynamic formalism of Bowen, Ruelle and Sinai [118–120], or large-deviation formalism, is quite convenient to study statistical properties of phase-space trajectories of systems with smooth potential energies and that obey Hamiltonian mechanics. One of the purposes of this formalism [121] is to use statistical properties of the trajectories in order to construct invariant probability measures. These

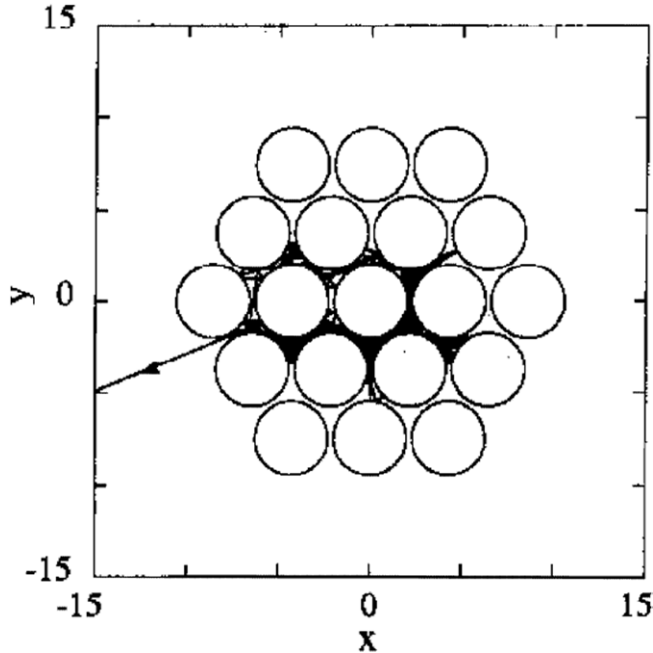


**Figure 12.** Plot of a trajectory of a particle escaping after several collisions from a hexagonal scatterer of periodic type formed by two shells of disks. The initial condition is located on the central disk at angle  $\phi = \pi/4$ . Reproduced with permission from [122]. Copyright 1995 American Physical Society.

measures in turn can be used to compute phase-space averages, which are needed for computing the effects of the chaotic scattering phenomena of physical interest here. The large-deviation formalism that we use goes beyond a linear or quadratic deviation of some quantity from its reference value. For instance, the chaotic behaviour of a system depends upon the exponential separation of the trajectories in the phase-space. Large-deviation formalism is designed to treat such circumstances. The central quantity of interest in thermodynamic formalism is an invariant probability measured on the set of phase-space trajectories. Gaspard and Dorfman [121] have constructed a probability measure where they define the topological pressure. In this context, the thermodynamic formalism is considered in time instead of space in contrast to equilibrium statistical mechanics. The topological pressure plays a role in dynamical systems theory very similar to that of the free energy for statistical mechanical systems. In addition, it is also relevant for establishing an important connection between the invariant probability measure on the constant energy surface. This connection lies at the core of thermodynamic formalism, which is quite clear according to the methods shown at [118–120].

#### 2.4. Escape rate formalism

In order to introduce escape rate formalism, we show in figure 12 a typical trajectory in a hexagonal scatterer [32]. The trajectory undergoes many collisions inside the scatterer and finally it exits the scatterer and escapes to infinity in free motion. By reversing time, the trajectory would be a typical ingoing trajectory of a scattering experiment. In this subsection, we consider an ensemble of initial conditions taken

inside the scatterer and we show the time evolution of all of them.

Although most trajectories escape from the scatterer, a few exist which remain trapped inside it. They play a very important role because they control the escaping dynamics. For instance, the periodic orbits bouncing on the line between the centers of two nearby disks remain trapped in the scatterer forever. Besides periodic orbits, there also exist nonperiodic orbits which are trapped in the scatterer as soon as the scatterer contains three disks, as shown in section 4. All the trapped orbits are unstable with strictly positive Lyapunov exponents and they form a fractal set of zero Lebesgue measure in the phase space [3]. Each trapped orbit has a stable and an unstable manifold which are associated with the negative and positive Lyapunov exponents. Time-reversal symmetry maps the stable manifold onto the unstable manifold. Because the trapped orbits are unstable, the set of trapped orbits is repelling and is accordingly called the fractal repeller  $J_L$ . The existence of this fractal repeller is typical of chaotic scattering phenomena.

Evidence for the fractal repeller is provided by the escape-time function shown at figure 13. The escape-time function therefore has singularities on the fractal set formed by the closure of the stable manifolds of the fractal repeller  $C_l[W_s(J_L)]$ .

On the other hand and from a phenomenological point of view [32], the escape rate can be calculated by the diffusion equation

$$\frac{\partial \rho}{\partial t} = D \nabla^2 \rho, \quad (24)$$

where  $\rho(r, t)$  is the number of particles per unit volume in the gas and  $D$  the diffusion coefficient, where the Laplacian operator acts on the position variable.

Indeed, when the scatterer becomes large enough with respect to the interdisk distance, the motion in the scatterer is essentially controlled by the diffusion equation. At the border  $C_L$  where the particles escape from the scatterer, the density should be considered as being equal to zero because the particles disappear from the diffusion process by escaping to infinity. This is what is called an absorbing boundary. Therefore, the time evolution of the particle density is obtained by solving the diffusion equation with absorbing boundary conditions

$$\rho|_{C_L} = 0. \quad (25)$$

We expect an exponential decay of the probability density,  $\rho \sim \exp(-st)$ , where  $s$  is the decay rate and its value is [32]

$$s_j = -D \left( \frac{\chi_j}{L} \right)^2, \quad (26)$$

where  $\chi_j$  are the eigenvalues associated with the Helmholtz equations,  $(D \nabla^2 - s_j) \phi_j = 0$  with  $\phi_j|_{C_L} = 0$ , and its specific first value for the hexagonal structure is  $\chi_1 = 2.67495$  [123] and  $L$  is the scaling factor of the coordinates transformation  $(x, y) \rightarrow (Lx, Ly)$ .

As a consequence of these observations, the diffusion coefficient can be estimated by this method which is alternative to the methods based on the Einstein and the Green–Kubo formulae [124]. We refer to this method as a first passage method because the diffusion coefficient is related to the statistics of the times of the first passage for the diffusion particles [125].

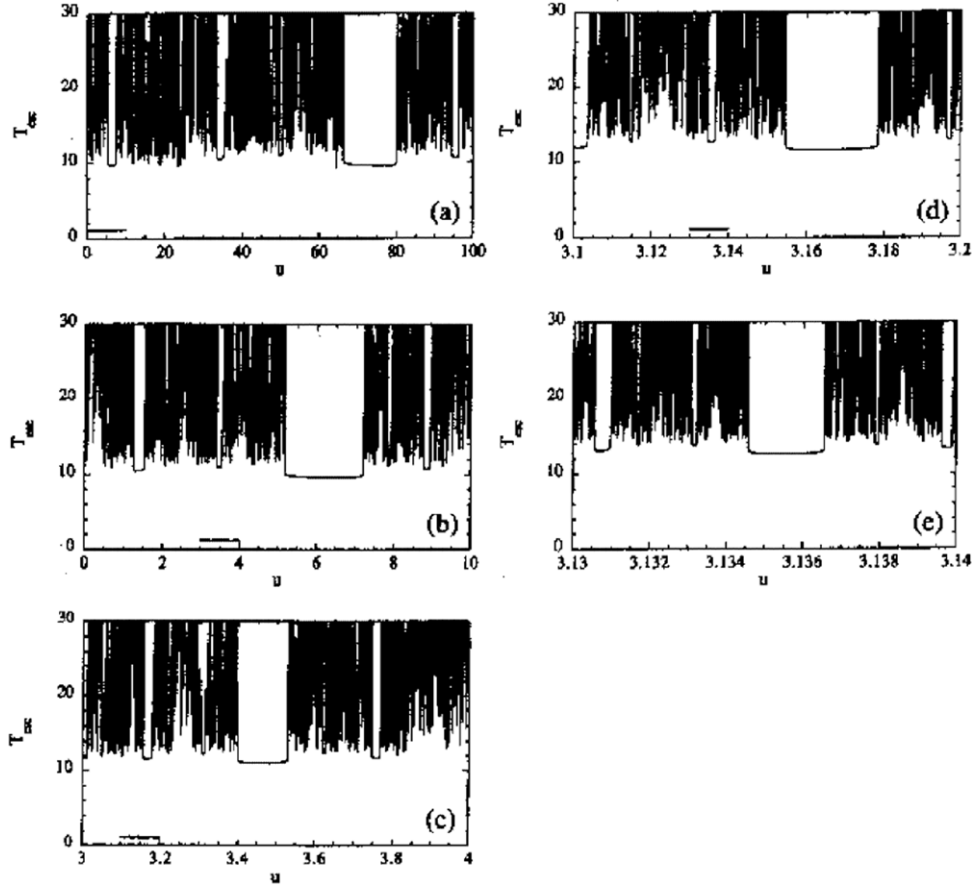


**Figure 13.** Plot of the escape-time function for the scatterer of figure 12 for the angle  $\phi = \pi/4$ , showing the intervals of continuity which provide the mark of the deterministic dynamics on these small scales. The comparison between the different intervals makes the scaling behaviour very similar. Reproduced with permission from [122]. Copyright 1995 American Physical Society.

### 3. Basins in chaotic scattering

In this section, we show the typical phase-space structure in chaotic scattering phenomena in which both fractal and Wada basins are very common.

#### 3.1. Fractal basins

The term *fractal* was coined by Benoit Mandelbrot in 1975 [127], which was taken from the Latin *fractus*. Fractal structures are very typical in nonlinear dynamics [126]. As we mentioned in previous sections, a basin of attraction is defined as the set of points that, taken as initial conditions, are attracted to a specific attractor. When there are two different attractors in a certain region of the phase space, two basins exist which are separated by a basin boundary. This basin boundary can be a smooth curve or can be instead a fractal curve.

Fractal basins have been reported in numerous researches related to many different fields of science. They are present in dissipative systems [128, 129], Hamiltonian systems [15], multi-species competition [130], predator-prey models [131], modeling of electronic systems [132], brain dynamics [133] and chaotic scattering [23], among others.

Fractal structures are quite typical in chaotic scattering since scattering destinations of the particles can take place through different paths. If the system is sensitive to the

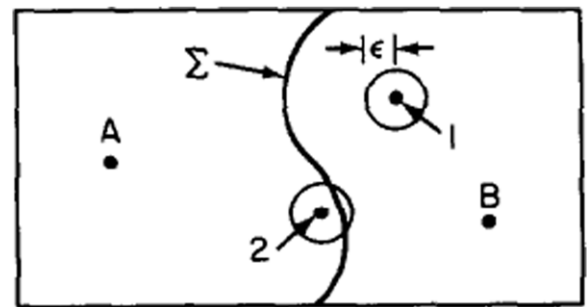


**Figure 14.** A scheme of phase space divided by the basin boundary  $\Sigma$  into basins of attraction for the two attractors  $A$  and  $B$ . Reproduced with permission from [191]. Copyright 1985 Elsevier.

initial conditions, our phase-space structure is very complex with points of different basins mixed. Specifically, in chaotic scattering systems, the fractalization typically occurs in the boundaries between the basins [3].

The importance of studying the structure of basin boundaries can be seen in the following example (see figure 14). In this picture, points 1 and 2 represent two such measured initial conditions. While the orbit generated by initial condition 1 is definitely attracted to  $B$ , initial condition 2 is uncertain in that it may be attracted to either  $A$  or  $B$ . Typical dynamical systems exhibit this behaviour. Another

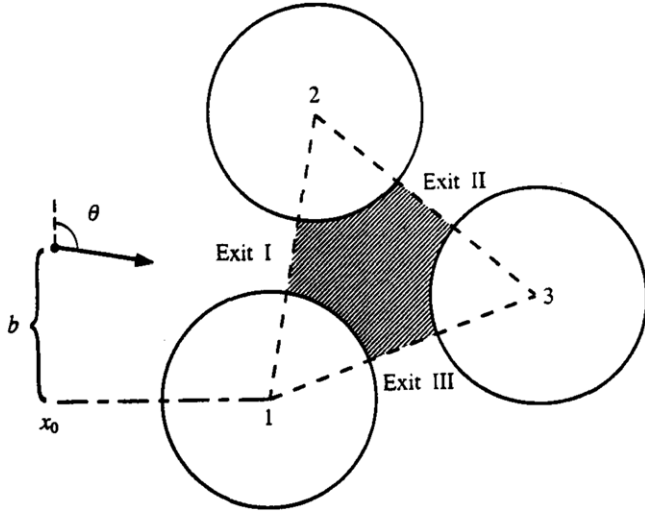


**Figure 15.** Picture showing the scattering scheme in the three-disk system in which permanent collisions take place before escaping from the dark region. The shadow part corresponds to the scattering region. Reproduced with permission from [15]. Copyright 1996 World Scientific.

reason for the interest in fractal basin boundaries is that as a system parameter is varied, a chaotic attractor can be suddenly destroyed in a collision with the basin boundary. As a consequence, and for values of the parameter beyond the crisis point, long chaotic transients occur [134], which can be a feature in chaotic scattering. Several standard dynamical systems possess fractal basin boundaries [135–137] and it is also the case of systems with chaotic scattering, as we show in this review paper. To illustrate it in this section, we provide one physical system with fractal basin boundaries. For that purpose, we choose the three-disk system.

**3.1.1. Fractal basins in the three-disk system.** We show the occurrence of fractal basins in chaotic scattering in one typical example, the three-disk system [32]. The dynamics of this system will be explained in detail in the next sections. In any case, its dynamics can be easily imagined by checking figure 15. The variable  $y = b$  is the impact parameter and  $\theta$ , the angle with respect to the  $y$ -axis; they are the two input variables.

On the other hand, a color-code is used to distinguish the different exits for which the initial conditions leave the scattering region. Initial conditions escaping through exit I, II and III are denoted in red, green and blue colors, respectively.

Figure 16 shows the exit basins associated with the different exits. It appears that there is always a cluster of two or three colors near the boundaries. This gives a clear indication that the basin boundaries are fractal.

### 3.2. Wada basins

In the previous subsection we have shown that fractal structures in the phase space are very typical in chaotic scattering phenomena. In these cases, the dynamics of the system can be very complex. We show here that, in some physical circumstances, the phase-space structure can be even more

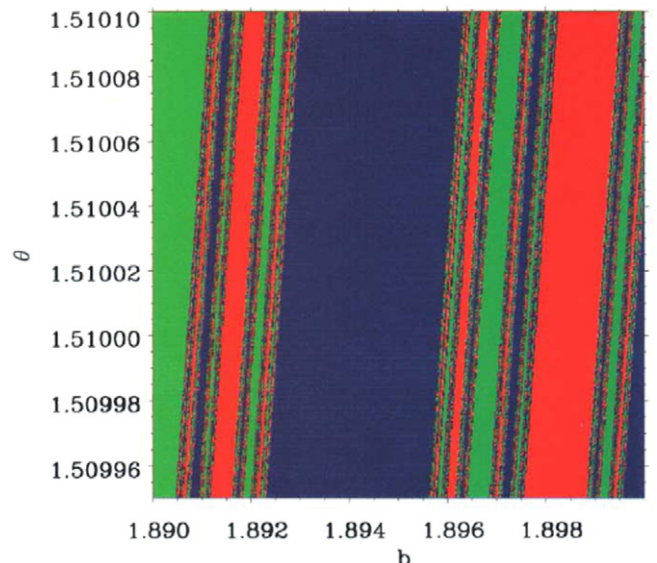


**Figure 16.** Exit basin for the three-disk system. The initial conditions escaping through exit I are plotted in red. Red and blue colors denote the initial conditions escaping through exits II and III, respectively. Reproduced with permission from [15]. Copyright 1996 World Scientific.

complex. This situation exists when the final destination of the initial conditions can take place through three or more different paths. In that case, we say that these basins have the Wada property, since the basin boundary contains points of three or more different basins.

To imagine a Wada basin boundary, take the map of the continental United States and consider the boundaries between the states. Almost all boundary points are common to two states, but there are a few dozen points which are common to three states and there exists a single boundary point that is shared by four states (the Four-State Corner bordering Arizona, Utah, Colorado and New Mexico. See figure 17).

In the three-disk system as a model of a nonlinear dynamical system with this kind of behaviour, this situation can arise where the set of boundary points common to more than two basins of attraction is fractal. Historically, the Dutch mathematician Luitzen E J Brouwer was the first (1910) to conceive the construction of three nonoverlapping regions in the plane, each connected with the property that every boundary point of any region is a boundary point of all three regions. In 1917 the Japanese topologist Kumiko Yoneyama extended the notion of regions to open sets and attributed the example to his teacher Takeo Wada: ‘Lakes of Wada’ [138].

Mathematically, a basin is Wada if any boundary point also belongs to the boundaries of at least two other basins [139, 141–147], i.e. every open neighborhood of a point belonging to a Wada basin boundary has a nonempty intersection with at least three different basins. If a dynamical system possesses Wada basins, the degree of unpredictability of destinations can be more severe than the case where there are fractal basin boundaries with only two destinations [15, 23, 128]. Wada basin boundaries in chaotic scattering have been recently observed experimentally with a simple optical system [148]. The common occurrence of Wada basin boundaries in



**Figure 17.** Picture of a USA map showing the Four-State Corner. Reproduced from Wikipedia Commons under the GNU Free Documentation License [http://en.wikipedia.org/wiki/Text\\_of\\_the\\_GNU\\_Free\\_Documentation\\_License](http://en.wikipedia.org/wiki/Text_of_the_GNU_Free_Documentation_License).

nonlinear dynamical systems was first pointed out by Kennedy and Yorke in 1991 [139]. On the other hand, a recent numerical study of the existence of Wada basins in the parameter plane has been carried out in [140]. In this last work, the authors state regions of unpredictability in the parameter space depending whether the basins associated are Wada or not.

For two-dimensional invertible maps or equivalently, three-dimensional flows, the mechanism for Wada basin boundaries is well understood, thanks to the rigorous mathematical work by Kennedy, Nusse and Yorke [139, 146]. In particular, Kennedy and Yorke proved a theorem [139] which states that, if  $p$  is a periodic point on the basin boundary, if the following two conditions are satisfied: (1) its unstable manifold intersects every basin, and (2) its stable manifold is dense in each of the basin boundaries, then the basins have the Wada property. This can be intuitively understood by referring to figure 18, where there are a number of  $K$  coexisting basins denoted by  $B_1, B_2, \dots$  and  $B_K$ .

Suppose  $p$  is a periodic point on the boundary of  $B_1$ , which is accessible to  $B_1$ . Let  $W^s(p)$  and  $W^u(p)$  be the stable and the unstable manifold of  $p$  (note that  $W^s(p)$  is the basin boundary of  $B_1$ ). Now arbitrarily choose a point  $x \in W^s(p)$  and imagine a circle  $C_\epsilon(x)$  of radius  $\epsilon$  centered at  $x$ . Since  $W^u(p)$  intersects every basin,  $C_\epsilon(x)$  must contain points of every basin, which can be seen by considering a one-dimensional curve segment  $D_k$  in the basin  $B_k$ , which intersects  $W^u(p)$ , for  $k = 1, \dots, K$ . Under inverse iterations of the map, the images of the curves will be arbitrarily close to the stable manifold of  $p$  and therefore be in  $C_\epsilon(x)$ . In fact, this is guaranteed mathematically by the

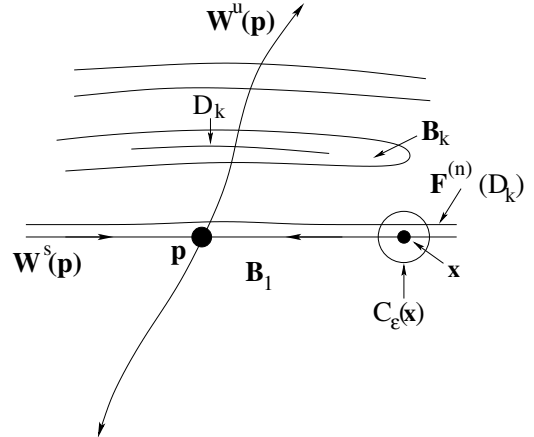


**Figure 18.** Schematic illustration of the Kennedy–Yorke theorem establishing the Wada property. Reproduced with permission from [19]. Copyright 2006 American Institute of Physics.

$\lambda$ -lemma due to Palis [149], which states that there exists a positive integer  $n$  such that  $(F^{-1})^{(n)}(D_k) \cap C_\epsilon(x)$  is nonempty. We thus see that the boundary of  $B_1$  must be the boundary of all other basins. Since  $W^s(p)$  is dense in each of the basin boundaries, all boundaries must be common to all basins and hence the Wada property.

As we indicated previously, the Wada property has been shown in several dynamical systems. In chaotic scattering problems, this property has been shown in the Hénon–Heiles system and in the dissipative Hénon–Heiles system, as we will show in the next sections. In order to illustrate this property

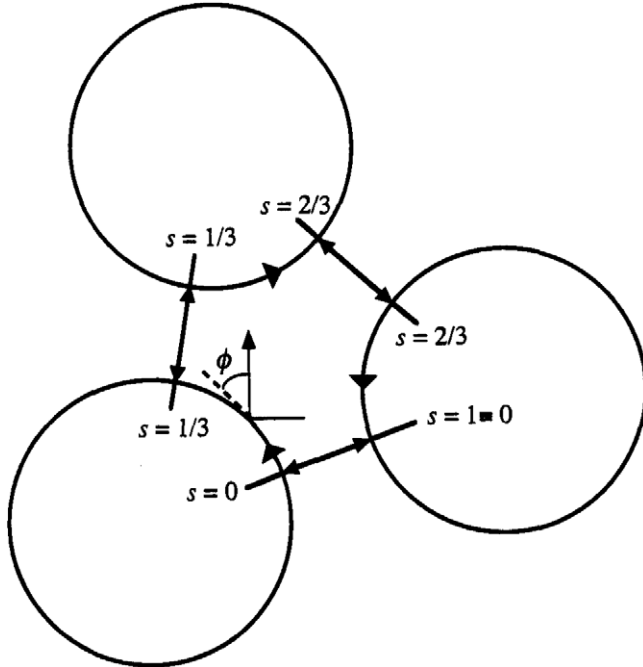


**Figure 19.** Plot of the parametrized coordinates  $(s, z)$ . Reproduced with permission from [15]. Copyright 1996 World Scientific.

in other chaotic scattering systems, we show that the basins of the three-disk problem discussed in the previous subsection has the Wada property, as well.

**3.2.1. Wada basins in the three-disk system.** In order to confirm that the basin boundaries of the three-disk system possesses the Wada property [15], we introduce a surface of the section corresponding to the surfaces of the three scattering disks. For this purpose, the position of the particle in the surface of the section when it is in the scattering region is parametrized by the arc length  $s$  measured in a counterclockwise direction along the three arcs contained in the region, as shown in figure 19. To uniquely specify the course of the trajectory, the variable  $z = \cos \phi$  is introduced, where  $\phi$  is the angle the trajectory makes with respect to the forward tangent immediately after impact.

In this coordinate system, the fixed points are located at:  $(0, 0)$ ,  $(1/3, 0)$  and  $(2/3, 0)$ . The picture of this surface section is shown in figure 20.

We can observe intuitively that these basins have the Wada property since the basin boundaries have points of every basin. However, we have to compute the unstable manifold of the fixed point  $(1/3, 0)$  in order to check this property. For that purpose, the algorithm explained in [150] is a good method for its computation. It is clear, according to figure 21, that the unstable manifold crosses all three boundaries and therefore the Wada property is satisfied.

#### 4. Representative physical systems that exhibit chaotic scattering

We present here a number of examples of dynamical systems from Celestial Mechanics, Atomic Physics and Fluid

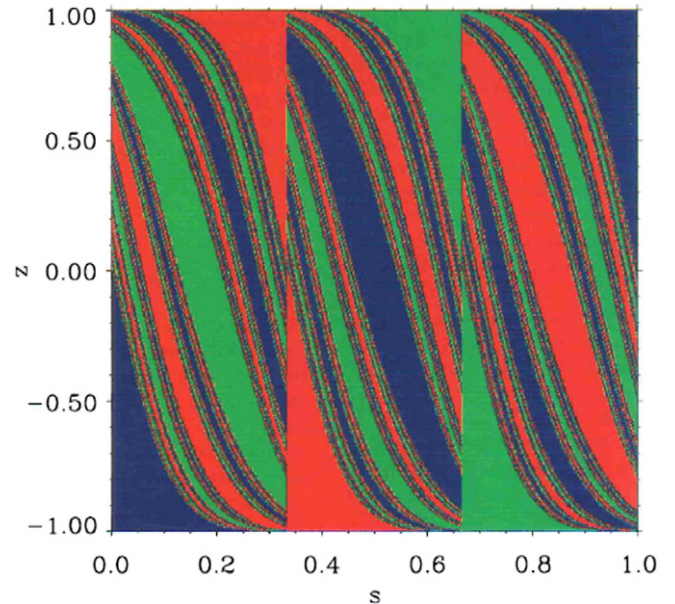


**Figure 20.** Plot of the basin boundary structure in  $(s, z)$  coordinates. Reproduced with permission from [15]. Copyright 1996 World Scientific.

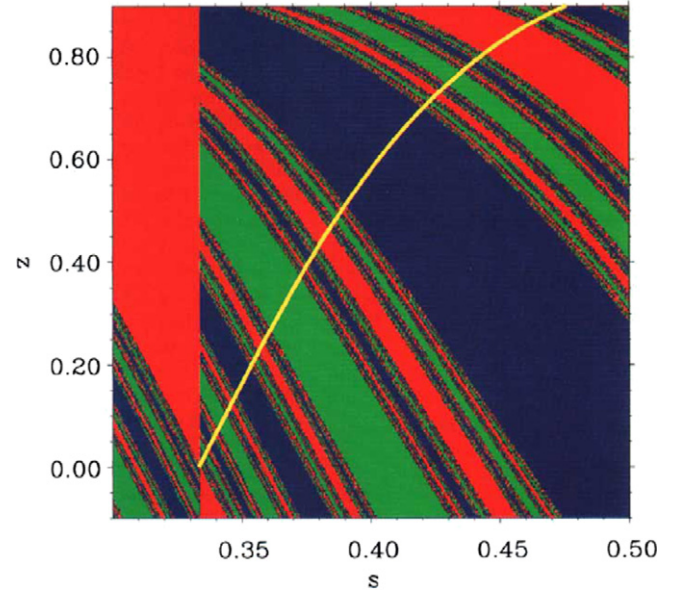


**Figure 21.** This figure shows a segment of the unstable manifold crossing all basins for which the Wada property is satisfied. Reproduced with permission from [15]. Copyright 1996 World Scientific.

Dynamics to illustrate chaotic scattering and its physical significance.

##### 4.1. Hénon–Heiles system

The Hénon–Heiles system is described by the Hamiltonian

$$H = \frac{1}{2}(\dot{x}^2 + \dot{y}^2) + \frac{1}{2}(x^2 + y^2) + x^2y - \frac{1}{3}y^3, \quad (27)$$

which defines the motion of a particle with a unit mass in the two-dimensional potential

$$V(x, y) = \frac{1}{2}(x^2 + y^2) + x^2y - \frac{1}{3}y^3. \quad (28)$$

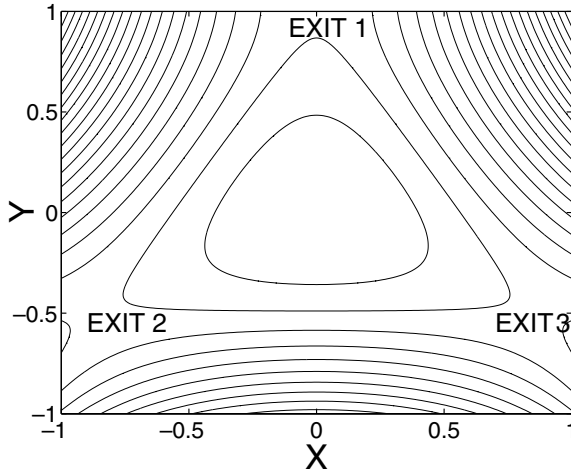
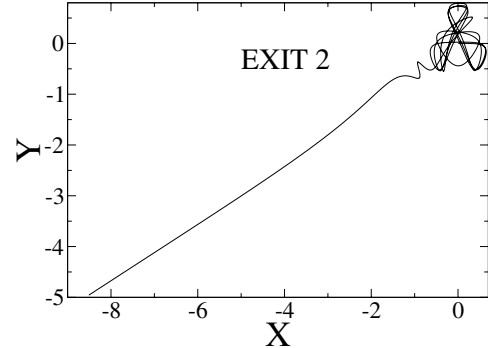


**Figure 22.** Representative contours of the Hénon–Heiles potential. Closed curves correspond to energy  $E < E_e = 1/6$ . There are three symmetric destinations for scattering particles.

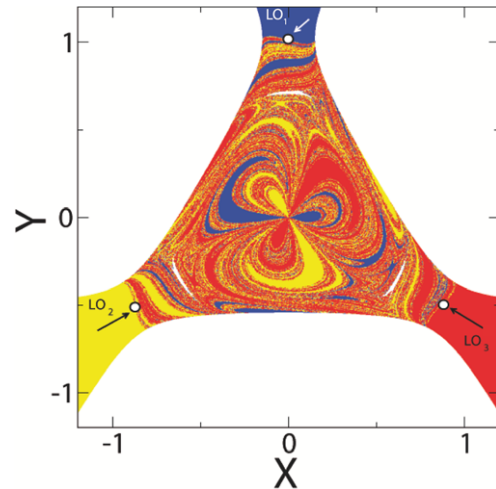
The system was originally proposed in 1964 to address the question of whether more than two constants of motion exist in the dynamics of a galaxy model [151]. Since then it has become a paradigmatic model for studying nonlinear and chaotic dynamics in *time-independent* Hamiltonian systems.

Figure 22 is a contour plot of the potential, equation (28), where the presence of a  $2\pi/3$  rotational symmetry with respect to the center of the potential at the origin can be seen. Particles initiated near the center with energy  $E < E_e = 1/6$  are confined in the vicinity because of the surrounding, classically impenetrable potential barrier, generating bounded orbits in the phase space. Particles with an energy larger than  $E_e$  can get into and out of the central region; the corresponding trajectories are unbounded (scattering trajectories). We thus focus on the energy regime of  $E > E_e$ . The triangular-like region about the center in figure 22 thus constitutes the scattering region whose size depends on the particle energy. As shown in the figure, there are three symmetric channels in the physical space through which particles can typically exit the scattering region. Figure 23 shows a typical scattering trajectory through one of the exits. At every opening, there exists an unstable periodic orbit, the *Lyapunov orbit*, where trajectories crossing it outwards will escape from the system and never return to the scattering region [152]. An interesting dynamical consequence of the existence of multiple coexisting escaping channels is that, asymptotically, scattering trajectories through different exits approach distinct scattering destinations. Regarding these destinations as ‘attractors’, complicated basin structures, e.g., Wada basins, can arise. An example of Lyapunov orbits and complicated basin structures is shown in figure 24.

On the other hand, this system has been the focus in the last few years as a prototype model to study bifurcations and chaos in Hamiltonian systems [153]. This kind of analysis has also been carried out by Blesa *et al* in [154]. Besides, a thorough study of the fractal structures in the phase space of this system has been carried out in [155, 156]. Finally, we can mention that a complete study of the threshold law for escaping from the scattering region in the Hénon–Heiles system has been



**Figure 23.** A typical scattering trajectory in the Hénon–Heiles system with  $E = 0.2$ , where the particle escapes through exit 2 as illustrated in figure 22.



**Figure 24.** Exit basins of the Hénon–Heiles Hamiltonian in physical space ( $x, y$ ) for energy  $E = 0.2$ . Colors blue, yellow and red denote the orbits escaping through exits 1–3, respectively. The Lyapunov orbits are denoted with black and white arrows. Reproduced with permission from [23]. Copyright 2001 American Physical Society.

developed by Zhao and Du in [157], where the authors find a nice analytic formula for the escape rates of the Hénon–Heiles system above the threshold value,  $E_e$ .

#### 4.2. Contopoulos system

The Contopoulos system is described by the Hamiltonian

$$H = \frac{1}{2}(\dot{x}^2 + \dot{y}^2) + \frac{1}{2}(x^2 + y^2) - xy^2, \quad (29)$$

which defines the motion of a unit mass particle in the two-dimensional potential

$$V(x, y) = \frac{1}{2}(x^2 + y^2) - xy^2. \quad (30)$$

Representative contours of the potential are shown in figure 25. Depending on the energy value  $E$ , the system can exhibit different types of dynamical behaviours. In fact, there exists a threshold energy value,  $E_e = 0.12$ , where the scattering dynamics are characteristically different below and above  $E_e$  [25, 158, 159]. For  $E < E_e$ , the system is effectively closed in the sense that particles originated from the central

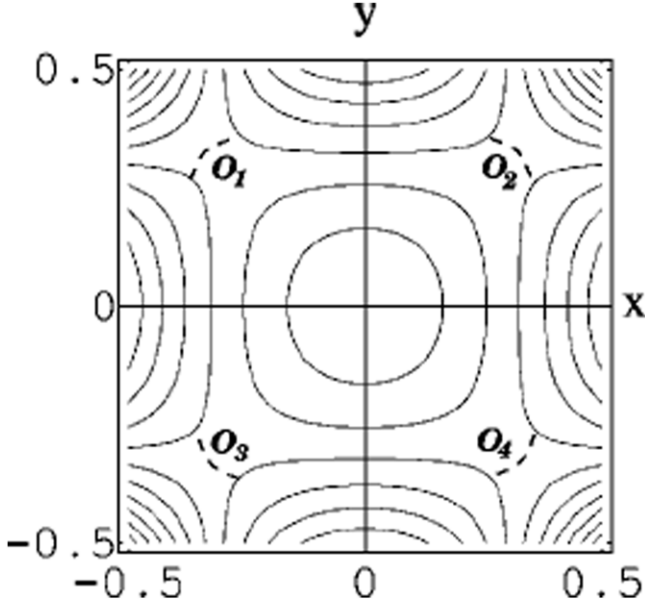


**Figure 25.** Contours of the Contopoulos potential. Depending of the energy values bounded or unbounded motions (with four exits). Reproduced with permission from [159]. Copyright 1999 American Institute of Physics.

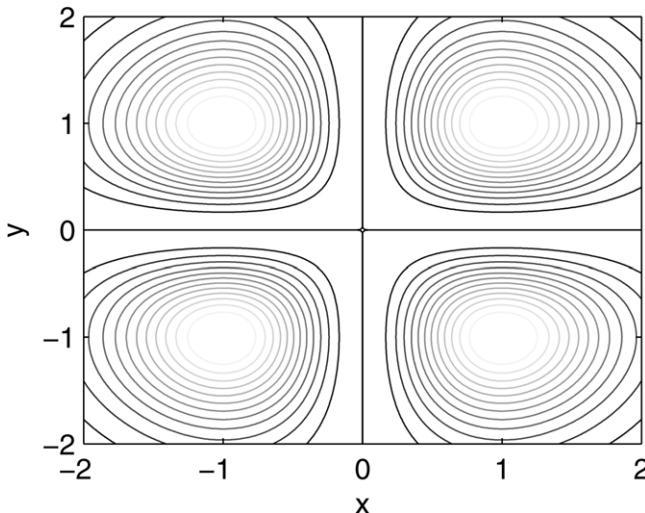


**Figure 26.** Contour plot of the four hill potential system.

potential region (the scattering region) are confined there forever. However, for  $E > E_e$ , the equipotential curves are open, allowing particles to escape from the scattering region, as indicated by the escaping channels in figure 25.

#### 4.3. Four hill potential system

The four hill potential system is described by the Hamiltonian

$$H(x, y) = \frac{1}{2}(\dot{x}^2 + \dot{y}^2) + x^2 y^2 \exp[-(x^2 + y^2)], \quad (31)$$

which defines the motion of a unit mass particle in the two-dimensional potential given by

$$V(x, y) = x^2 y^2 \exp[-(x^2 + y^2)], \quad (32)$$

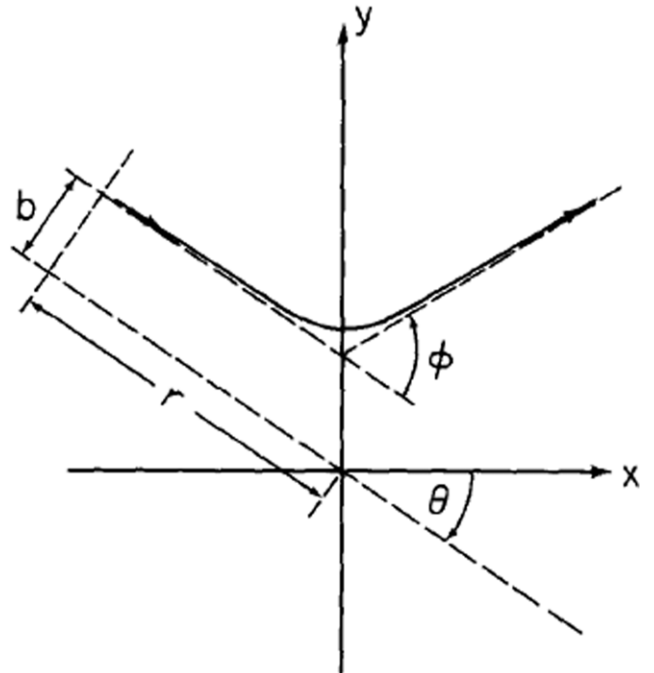


**Figure 27.** Illustration of a typical scattering trajectory in the four hill potential system. Reproduced with permission from [5]. Copyright 1990 Elsevier.

The system possesses a  $\pi/2$  symmetry and it has been used as a prototypical model to reveal the abrupt bifurcation route to chaotic scattering [5]. Representative equipotential curves are shown in figure 26.

The potential function has four local maxima of equal height  $E_m = e^{-2}$ , symmetrically located at  $(x, y) = (\pm 1, \pm 1)$ , respectively. All trajectories originated in the scattering region (approximately defined by some region that encompasses the four maxima), except a set of measure zero, approach infinity asymptotically. A representative scattering trajectory is shown in figure 27.

The system does not possess any Lyapunov orbits, so the escape of a scattering trajectory can be conveniently regarded as its exiting the region defined by  $x^2 + y^2 > r^2$ , where  $r$  is some distance from the center of the scattering region to the region where the potential is negligible. Features of chaos in the scattering dynamics can be seen from the scattering function in figure 28, which exhibits singularities on all scales. In fact, there is a fractal set of singularities in the scattering function [5], as in any system that exhibits chaotic scattering.

#### 4.4. Barbanis potential system

The Barbanis system is a paradigmatic model in Chemistry [160], which has been used extensively to model the phenomenon of fluorescence excitation of benzophenone [161] and also in quantum analysis and simulations [162]. The potential and Hamiltonian functions (for unit mass) are

$$V(x, y) = \frac{1}{2}(x^2 + y^2) - x^2 y^2, \quad (33)$$

and

$$H = \frac{1}{2}(\dot{x}^2 + \dot{y}^2) + \frac{1}{2}(x^2 + y^2) - x^2 y^2, \quad (34)$$

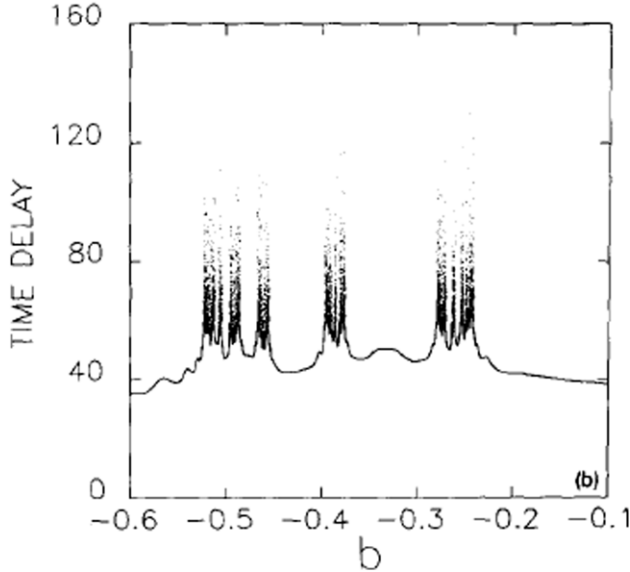


**Figure 28.** For the four hill potential system, a typical scattering function containing an infinite set of singularities which constitutes a fractal set. Reproduced with permission from [5]. Copyright 1990 Elsevier.

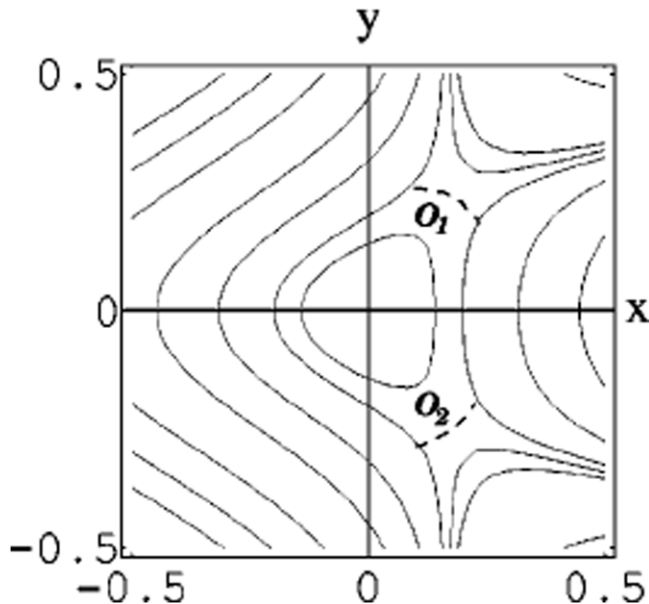


**Figure 29.** Contour plot of the Barbanis potential. Depending on the energy values, bounded or unbounded motions (with two different paths for escaping) exist. Reproduced with permission from [159]. Copyright 1999 American Institute of Physics.

respectively. As for the Hénon–Heiles and Contopoulos systems, the Barbanis potential has a threshold energy value  $E_c = 1/8$  above which particles can escape [163]. The system exhibits two distinct escaping channels. Figure 29 shows several contours of the potential function and the Lyapunov orbits ( $O_1$  and  $O_2$ ) associated with the escaping channels (dotted lines). A representative heteroclinic orbit approaching the two Lyapunov orbits and a homoclinic orbit approaching one of the Lyapunov orbits are shown in figure 30.

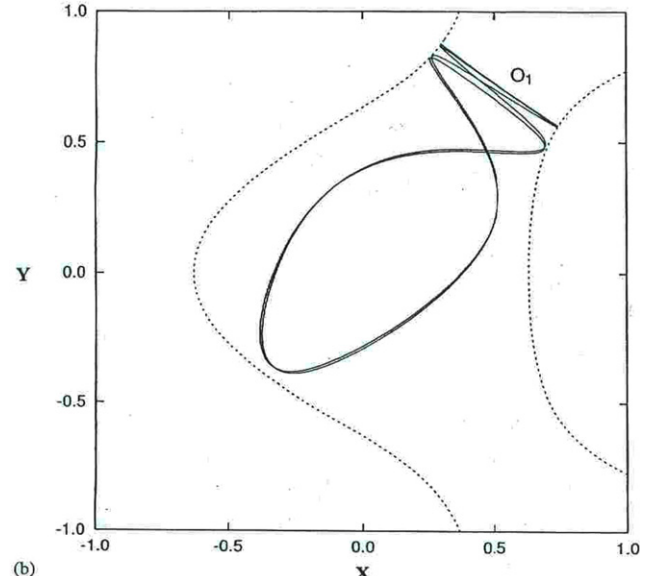
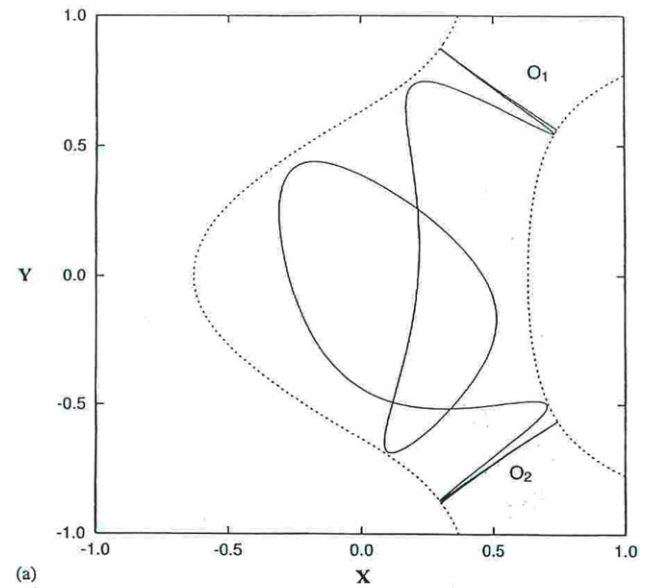


**Figure 30.** For  $E > E_c$  in the Barbanis scattering system, (a) a heteroclinic orbit approaching the two Lyapunov periodic orbits  $O_1$  and  $O_2$ , and (b) a homoclinic orbit approaching the Lyapunov orbit  $O_1$ . Reproduced with permission from [159]. Copyright 1999 American Institute of Physics.

#### 4.5. Three hard-disk scattering system

This is one of the simplest systems exhibiting chaotic scattering [32], the dynamics of which can be understood in a physically intuitive manner by studying one-, two- and eventually three-disk systems. The three-disk system can also be used to gain insights into the dynamics of unimolecular reactions [14, 164–166].

For a single circular disk, every trajectory is of the scattering type: coming from infinity, hitting the disk and returning to infinity. The scatterer has a rotational symmetry so that the angular momentum is preserved. The scattering cross section is determined by the diameter of the disk:  $\sigma = 2a$ . Suppose the coordinate system is such that the center of the disk is the origin. For particles moving toward the disk parallel

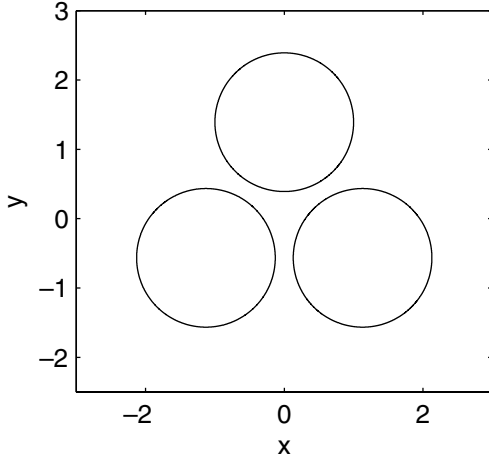


**Figure 31.** A three hard-disk chaotic scattering system.

to the  $x$ -axis from  $x < 0$  with an impact parameter  $b$ , the deflection angle  $\Theta$  is given by  $b = a \sin \phi = a \cos \frac{\Theta}{2}$ , since  $\Theta = \pi - 2\phi$ . Setting  $d\sigma = |db|$ , we can obtain the differential cross section according to the formula [167]:

$$\frac{d\sigma}{d\Theta} = \frac{a}{2} \left| \sin \frac{\Theta}{2} \right|. \quad (35)$$

There are in fact no orbits that can be trapped at a finite distance so that no dynamical invariant set (e.g. repellers) can exist in the single-disk system.

Now consider a two-disk scattering system, which is similar to the one-disk system but it exhibits new and interesting properties. Let  $r$  be the distance between the centers of the two disks. The system has no rotational symmetry so that angular momentum is no longer conserved. The total cross section varies between  $2a$  and  $4a$  depending on the direction of the incident beam. There is, however, the possibility that trajectories can undergo an infinite number of collisions between the disks (for  $r > 2a$ ) and get trapped in the region between the two disks. These are the unstable periodic orbits. There are variants of the two-disk system, such as a wire or grating. In each case, the repeller consists of similar types of unstable periodic orbits and their images by reflection or translation. Such systems can model electronic mesoscopic circuits [168, 169].

A three-disk system in which the disk centers form an equilateral triangle of side  $r$  is shown in figure 31. Typical scattering functions from this system are shown in figures 32(a) and (b), which contain a fractal set of singularities, giving rise to sensitive dependence on initial conditions. In fact, there exists a chaotic repeller (objects that are repellent in all possible directions in the phase space [1]) that contains a countably infinite number of unstable periodic orbits and an uncountably infinite number of chaotic trajectories, physically due to the defocusing nature of the scattering from any single disk. The fractal patterns can be seen experimentally by light scattering from a set of spherical mirrors, which generates by reflection a hierarchical structure of images [170, 171].

## 5. Chaotic scattering in other physical systems

In this section we show some chaotic scattering phenomena appearing in other typical physical systems.

### 5.1. Chaotic scattering in billiards

One of the most typical physical systems in which chaotic scattering can take place is the case of billiards [172–174]. Billiard systems consist of a particle which can move freely except for specular reflections at rigid walls [175]. Furthermore, this kind of system presents a lot of experimental implementations which are quite relevant in the field. Precise billiard experiments have used microwaves in metal [174, 176] and superconducting [173] cavities and with wave guides [177], visible light reflected from mirrors [178], phonons in quartz blocks [179], atoms interacting with laser beams [180, 181], etc, among others. Billiards can be classified as closed and open. Closed billiard systems exhibit energy level distributions and scarring of wave functions as predicted by semiclassical [182] and random matrix [183] theories. Open billiard systems exhibit phenomena such as fractal conductance fluctuations [180]. For both closed and open systems, the behaviour depends crucially on the classical dynamics, which can be tuned to be integrable, chaotic or mixed [180, 181, 184]. The escape rate is a characteristic of open billiards which is both experimentally accessible [180, 181] and important for transport properties of many systems. In order to understand the dynamical behaviour of this type of system, we introduce two paradigmatic models for both closed and open systems which are of interest in chaotic scattering.

**5.1.1. Closed billiards.** Here we focus on the case where the billiard shape changes in time according to a certain law [185]. Such a driven billiard not only leads to a higher dimensional phase space of the scattering processes but also to a nonconservation time evolution of the energy. Driven billiards represent prototype models for the evolution of ensembles of particles in a closed driven environment where multiple scattering off the driven boundary takes place (as occurs in the scattering region) thereby leading to a dynamical nonequilibrium state. Extremely little is known on the properties of such systems. The few existing investigations deal with aspects such as Fermi acceleration [186] and principal structures of the corresponding phase space [186]. The interest on the escape rates of driven billiards was addressed in [185]. In that work, the classical scattering dynamics and the time evolution of ensembles of particles in a harmonically driven elliptical billiard was studied.

The decay of the escape rate is traced back to the underlying scattering mechanism by identifying two fundamental scattering processes being key ingredients for the time evolution. The escape rate behaves asymptotically as  $N_c \sim t^{-w_c}$  and it can be shown that the decay constant  $w_c$  can be changed continuously by varying the driven amplitude  $C$ , according to the law  $C \sin(\omega t + \delta)$ . Furthermore, phenomena such as a pulsed escape, demonstrate the richness of the

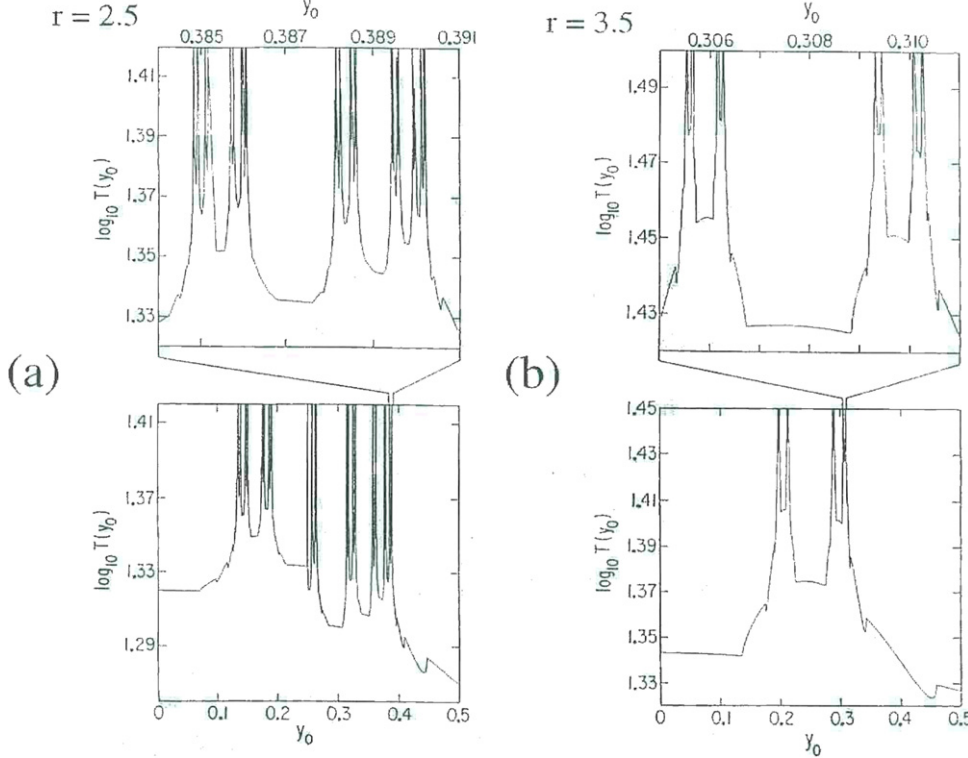


**Figure 32.** Typical scattering function of the three-disk system for (a)  $r = 2.5$  and (b)  $r = 3.5$ , where  $a = 1$  and the impact parameter is  $y_0$ . Reproduced with permission from [32]. Copyright 1998 Cambridge University Press.

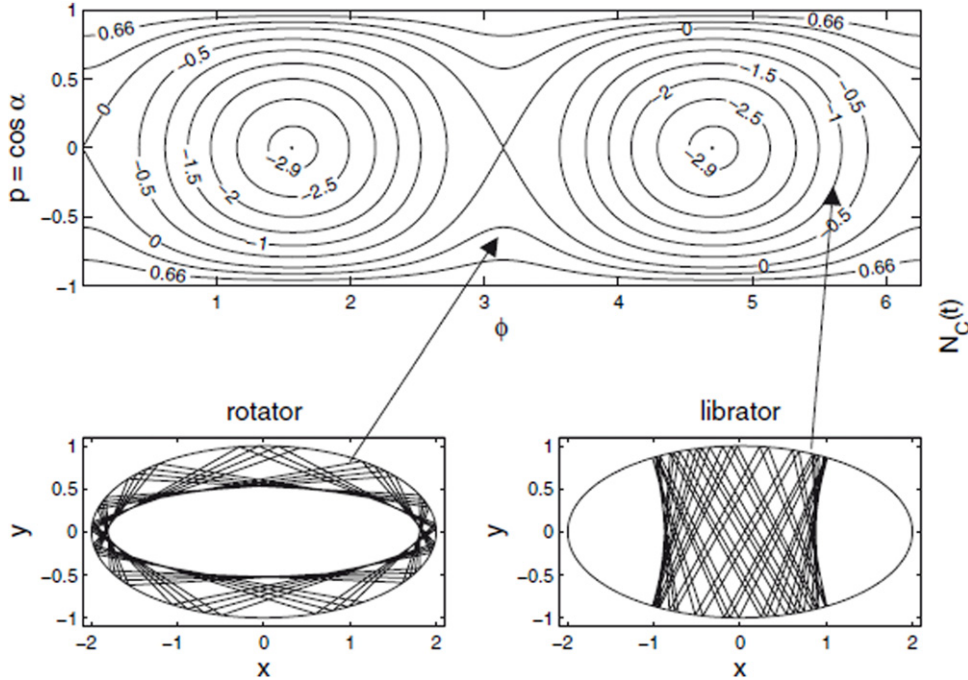


**Figure 33.** Picture showing the phase space of the ellipse, the invariant curves are the contour lines of  $F(\phi, p)$  (upper part) and typical trajectories in coordinate space (lower part). Reproduced with permission from [185]. Copyright 2007 European Physical Society.

properties of driven billiards and suggest specifically the driven ellipse as a prototype system for the nonequilibrium evolution of ensembles that experience multiple scattering processes with moving targets.

The dynamics of an ellipse is completely integrable [187, 188], as shown in the Poincaré surface of section depicted

in figure 33. In addition to the energy, there is a second constant of motion that reads

$$F(\varphi, p) = \frac{p^2(1 + 1(1 - \varepsilon^2) \cot^2 \varphi) - \varepsilon^2}{1 + (1 - \varepsilon^2) \cot^2 \varphi - \varepsilon^2}, \quad (36)$$

restricting the orbits to invariant curves in the phase space, where  $\varepsilon = \sqrt{1 - B^2/A^2}$  is the eccentricity and  $p = \cos \alpha$

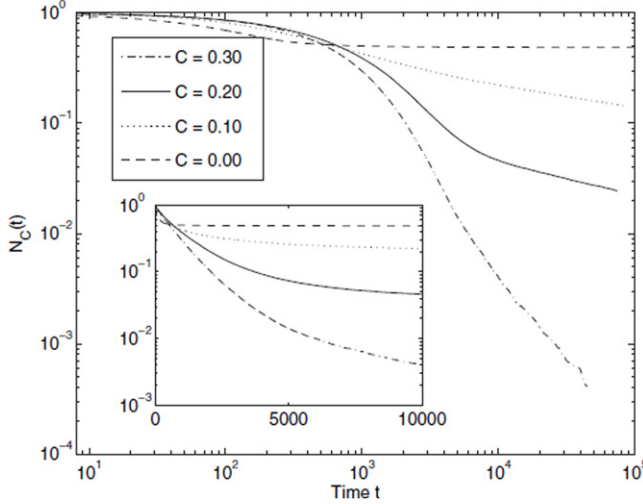


**Figure 34.** Fraction of remaining particles  $N_c(t)$  of the IVE as a function of time for different values of the driving amplitude  $C$ . The inset represents a semi-logarithmic plot. Reproduced with permission from [185]. Copyright 2007 European Physical Society.

and  $F(\varphi, p)$  is the angular momenta about two foci [189]. Two kinds of orbits can be observed in the ellipse, called librators and rotators, as shown in figure 33. Librators cross the  $x$ -axis between the two foci and touch repeatedly a confocal hyperbola. Rotators travel around the ellipse, eventually exploring every value of  $\varphi$ , repeatedly touching a confocal ellipse. They have values of  $F$  between zero and one.

One of the important issues in this kind of problem is the estimation of the escape rate of the orbits from the elliptical billiard. For that purpose, we suppose that the billiard has a small hole at the very right of the ellipse. In [185] they shot a large number of particles, say  $10^6$ , with initial conditions uniformly randomly distributed in  $\varphi, \alpha$  space. The decay approach to the saturation value  $N_s(\varepsilon)$ , which is caused by particles travelling on librator orbits that are not connected with the hole [181]. The numerical results obtained for the intermediate velocity ensemble (IVE),  $|v_0| \approx \omega C$ , are shown in figure 34. On the other hand, the analytical dependence of  $N_s(\varepsilon)$  is given by [190]

$$N_s(\varepsilon) = \frac{1}{\pi^2} \int_0^{2\pi} \arccos \sqrt{\frac{\varepsilon^2}{1 + (1 - \varepsilon^2 \cot^2 \varphi)}} d\varphi. \quad (37)$$

One can therefore conclude that varying  $\varepsilon$  allows us to control the total number of particles being emitted.

We present now the case of a time-dependent ellipse in which we apply harmonic oscillations to the boundary of the ellipse according to [185]. The decay rate of the particles, for the high velocity ensemble (HVE),  $|v_0| \gg \omega C$ , is represented in figure 35. A short time exponential decay is followed by a transient and the long time behaviour ( $t > 10^4$ ) is to a good approximation algebraic,  $N_c(t) \sim t^{-\omega_c}$ . We can observe, for high values of  $t$ , a saturation in the decay rate curve.

**5.1.2. Open billiards.** There are many chaotic scattering situations wherein a scattered orbit may leave the scattering region in different identifiable ways. In such cases, we refer

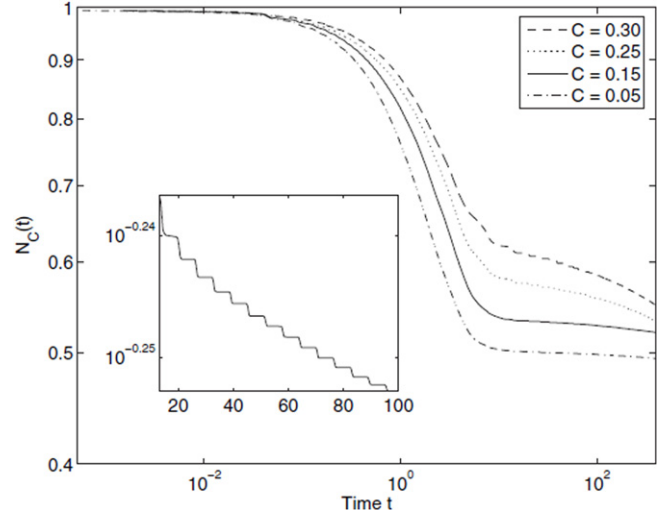


**Figure 35.** Fraction of remaining particles  $N_c(t)$  for the HVE,  $2\pi$  oscillations of the decay are shown in the inset. Reproduced with permission from [185]. Copyright 2007 European Physical Society.

to the collection of initial conditions, whose subsequent orbits exit the scattering region in the same way, as the basin for that type of exit. The boundary of those exits can be fractal [3, 191].

The experimental study of basin boundaries has proven difficult because these sets are nonattracting; typical initial conditions near these sets lead to orbits which tend towards regions of state space far from the basin boundaries. However, this observation is possible in systems called optical billiards [178]. These systems consist of polished, reflective surfaces. One example is illustrated in figure 36. In this configuration, each of the spheres of radius  $d$  is not in contact with the other spheres. The distance between the centers of the touching spheres is  $d$ , while the distance between the nontouching spheres is  $l$  with  $d < l < \sqrt{2}d$ . A similar configuration to this one has been proposed as a device for distributing infrared networking signals [192].

Now, we describe the dynamics of this system since it is a prototype model for chaotic scattering for these cases [178].

The measure of the fractal dimension of the basin boundaries [3] for five differently configured optical billiards by analyzing the digital images of these billiards, are shown in figure 37. We note that the basin boundaries seen in configurations 1–4 exhibit a different topology. This fact can be easily appreciated by seeing the different values of the fractal dimension that correspond to different topologies.

In this configuration, we can define the scattering region as the region that is within the tetrahedron whose edges connect the sphere centers but outside the spheres. In general, all orbits that are bounded for all forward and backward time,  $t \rightarrow \pm\infty$  are contained within the scattering region. The set of all orbits is ergodic<sup>1</sup> and forms what we shall refer to as the chaotic invariant set [23] of our scatterer. If an orbit enters the scattering region and then leaves it, it never

<sup>1</sup> An ergodic process is one for which statistical measures such as mean and standard deviation are constant in time, and the statistics are the same for any chosen time series. It means that an ergodic orbit fulfills the phase space after a long time, although ergodic does not imply chaos necessarily [193].

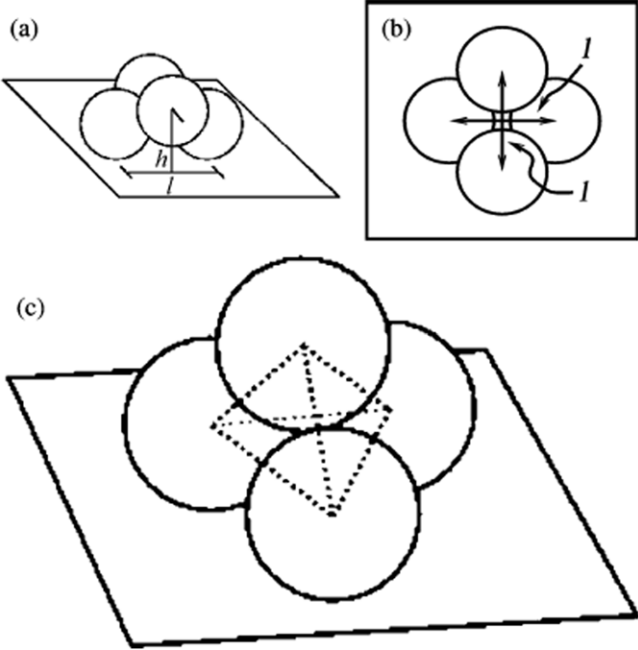


**Figure 36.** Schematic of configurations of spheres used in this experiment. Reproduced with permission from [178]. Copyright 2001 Elsevier.

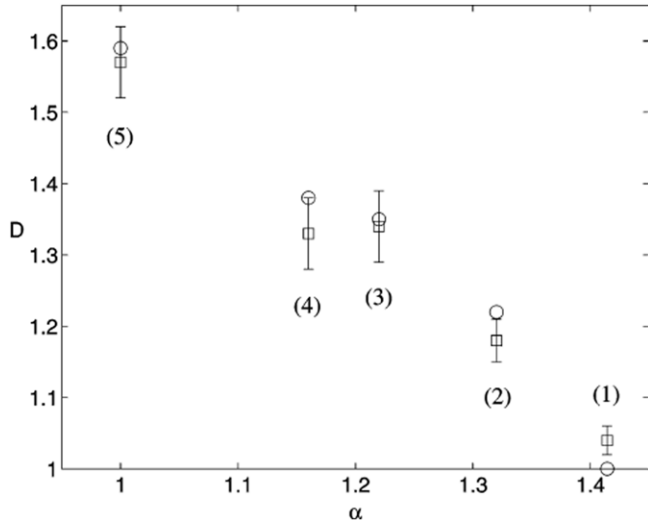


**Figure 37.** Fractal dimension versus  $\alpha \equiv l/d$ . Each value of  $\alpha$  represents one configuration. Reproduced with permission from [178]. Copyright 2001 Elsevier.

returns. A ray entering the scattering region has multiple ways to exit. In particular, there are four exits for the configuration of figure 36(b) corresponding to exits through the four faces of the regular tetrahedron, while for figure 36(a) there are two exits.

In order to study the phase-space structure, the computation of the basin boundaries elucidates the results obtained on the fractal dimension. The authors in [178] found that the basins and their boundaries appear qualitatively similar; the fractal dimension determined previously agree closely in all the configurations according with figure 37.

Some of the basin boundaries in the phase space are shown in figure 38. In this picture the black points represent the initial conditions that exit downward from the billiard and the white

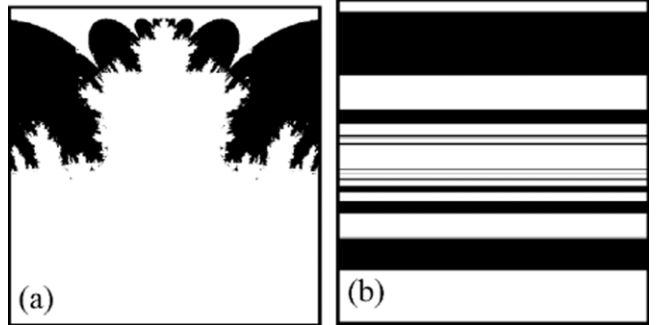


**Figure 38.** Basins in phase space  $(x, \dot{x})$  in a simulation where  $\alpha = 1.22$ . White points represent the initial conditions escaping from the billiard and black points represent the initial conditions trapped in the billiard walls. Reproduced with permission from [178]. Copyright 2001 Elsevier.

points represent the initial conditions that exit upward from the billiard.

### 5.2. Chaotic scattering in driven barriers

One of the typical problems in chaotic scattering concerns driven potential barriers; this implies time-dependent potential systems and they will be described later in section 9.1.

Harmonically driven barriers appear in many areas in modern physics, particularly in mesoscopic electronic semiconductor devices [106, 194, 195] and other microstructures and nanostructures driven by external voltages or applied laser fields. They also play a role in ultra-atomic wave packets exposed to optical barriers and photoinduced dynamics in strong laser fields or dissociation processes of molecules on solid surfaces. The strong external driving of the system typically leads to nonlinear quantum effects and chaos in the corresponding classical system. Two paradigmatic potentials have been investigated in detail in the literature, the driven potential and the driven potential barrier. In the following, we give a short overview of known features of this kind of system according to [196].

An early study of a vertically oscillating rectangular potential barrier, i.e. a potential with a harmonically oscillating height appears in [197] aimed to derive an expression for the tunneling time through potential barriers. Particles interacting with a driven potential barrier can absorb or emit quanta of  $\hbar\omega$ , where  $\omega$  is the driving frequency. This leads to frequency-dependent resonances in the tunneling probability through the vertically oscillating barrier, as shown in [198] for a rectangular barrier and a raised cosine potential.

Although several works deal with the tunneling through a laterally driven square barrier, the classical dynamics in this system is largely unknown. In this section, we cover the study of the phase-space structure for classical particles through a laterally driven potential [199] which is relevant in scattering processes. The aim of this part of the review is to add a comprehensive survey of the periodically driven square with an oscillating position in the classical regime. In order to show some evidence on the phase-space structure we are going to describe the model used in [196].

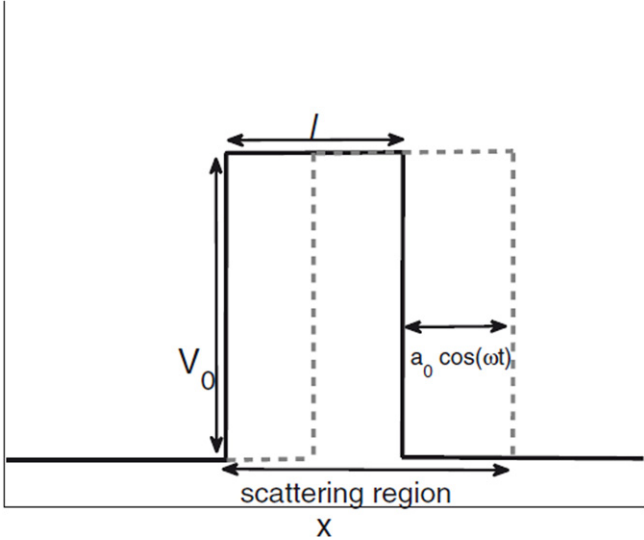


**Figure 39.** The ac-driven potential barrier. Reproduced with permission from [196]. Copyright 2008 American Physical Society.

**5.2.1. Driven barrier model.** The classical system consists of a one-dimensional laterally oscillating potential of a finite and constant height  $V_0$  and width  $l$ , as shown in figure 39.

The driving function is assumed to be harmonic, with a driving amplitude  $a_0$  and frequency  $\omega$  and reads as follows:

$$V(x, t) = V_0 \Theta \left( \frac{l}{2} - |x - a_0 \cos(\omega t)| \right). \quad (38)$$

Although the dynamics of the system are continuous, the forces acting on the particle are point-like and the particles move ballistically between collisions with each of the edges of the barrier. Therefore, it is sufficient to describe the dynamics in terms of a discrete mapping between collisions. After an appropriate change of coordinates [196], we obtain

$$v_{n+1} = v_b(t_{n+1}) + \text{sign}[v_n - v_b(t_{n+1})] \times \sqrt{[v_n - v_b(t_{n+1})]^2 \pm \frac{2}{m} V_0}, \quad (39)$$

if the particle is transmitted and

$$v_{n+1} = 2v_b - v_n, \quad (40)$$

if the particle is reflected, where  $v_b(t) = -a_0 \omega \sin(\omega t_{n+1})$  is the barrier velocity at the time of the collision  $t_{n+1}$  and the sign  $\pm$  depends on whether the particle is transmitted into the barrier ( $-$ ) or leaves the barrier ( $+$ ). The time  $t_n$  is mapped on the time  $t_{n+1}$  of the next collision of the particle with one of the barrier's edges. Therefore,  $t_{n+1}$  is the smallest solution of

$$x_b(t_{n+1}) = x_n + v_n(t_{n+1} - t_n), \quad (41)$$

where  $x_b$  can be each edge of the barrier,  $x_b = a_0 \cos(\omega t)$  or  $x_b = a_0 \cos(\omega t) + l$ .

The only parameter left in the mapping is  $V_0/V_\omega$ , where  $V_\omega = m a_0^2 \omega^2 / 2$  is the maximum kinetic energy that a particle can have in the barrier's frame of reference. The second parameter,  $l/a_0$ , is the barrier's thickness measured in units of the amplitude. If we scale the energy in units of  $V_\omega$ , the system is completely described by the parameters  $V_0$  and  $l$ .

**5.2.2. Phase-space structure.** In this subsection we show the structures in the phase space in terms of the Poincaré surface by mapping all collisions of the particle with either side of the barrier to the Poincaré section.

For this purpose, the entire phase space is covered with a fine grid of initial conditions to guarantee that all relevant structures are being shown in the Poincaré sections. The resulting Poincaré section is plotted in figure 40(a). The system's parameters are typical for an experimental setup using semiconductor structures driven by external voltages or applied laser fields [200, 201].

The phase space of the ac-driven barrier has four stable KAM islands whose center is a stable periodic orbit of period 4. This means that, through the driving, the repulsive potential can trap particles in a small part of the phase space. This kind of dynamical trapping works only for a harmonic driving law. The periodic orbit at the center of the island is stable because it lies symmetrically around the inflection points of the harmonic driving function. An enlargement of the fourth island in figure 40(a) is plotted in figure 40(b) and shows the typical structure of an elliptic fixed point surrounded by a stable island of quasiperiodic orbits and chains of subislands.

The Poincaré section of figure 40(a) is not unique because it shows all collisions, with both edges of the barrier and in both directions. Structures 1 and 4 correspond to collisions with the left-hand edge, structures 2 and 3 correspond to collisions with the right-hand edge. The four regular islands are symmetrical, the first and the second structures are identical to the third and fourth with their phases increased by  $\pi$  and the sign of their velocity inverted.

The trajectory of the central periodic orbit of the stable island, plotted in figure 41(a), is the following: starting from the left of the barrier at point 4 with zero velocity, the particle is hit by the barrier at point 1. The trajectories of the quasiperiodic orbits can be understood as a perturbation of the periodic orbit described above. A typical trajectory of such an orbit is plotted in figure 41(b).

The curve representing the maximum barrier potential allowing for periodic orbits as a function of the barrier's thickness is plotted in figure 42.

**5.2.3. Scattering dynamics.** The phase-space structure presented in the previous subsection has relevant effects on scattering processes. Due to the existence of a KAM island in the phase space, the ac-driven barrier is a chaotic scatterer [3]. To simulate the scattering process, the authors in [196] place an ensemble of particles with a uniformly distributed velocity  $v_{\text{in}}$  far outside of the scattering region as in typical scattering processes. Typical trajectories for both acceleration and deceleration cases are shown in figures 43(a) and (b).

We can observe that the dynamics are very sensitive to the initial conditions, as we can observe in figure 44 in which we observe the phase-space structure [202].

On the other hand, it is known that in most systems which exhibit chaotic scattering, singularities in the scattering function have a divergent dwell time (delay time or escape time). This can be easily understood since scattering is infinitely sensitive to perturbations of the initial conditions

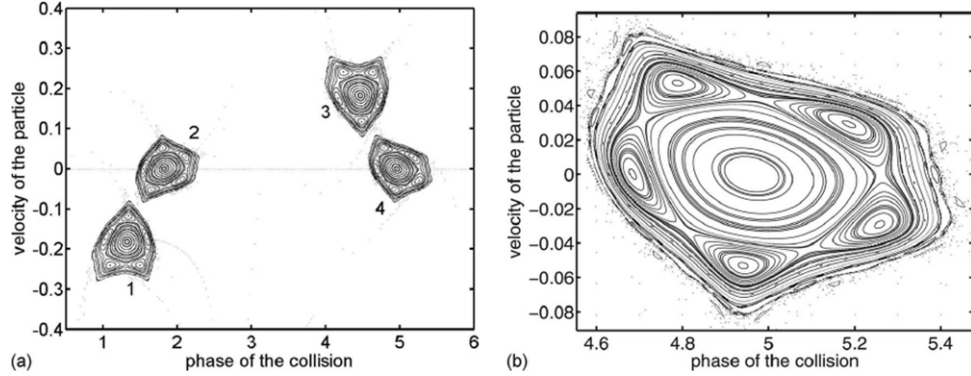


**Figure 40.** (a) Typical Poincaré section showing trapped particles. (b) Zoom of figure 40(a) showing trapped particles. Reproduced with permission from [196]. Copyright 2008 American Physical Society.

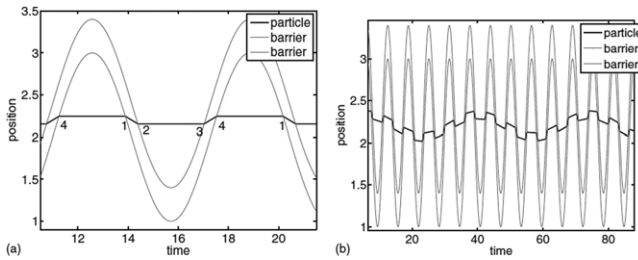


**Figure 41.** Time series of trapped particles. The black line represents the particle, the two gray lines represent the edges of the barrier. Reproduced with permission from [196]. Copyright 2008 American Physical Society.

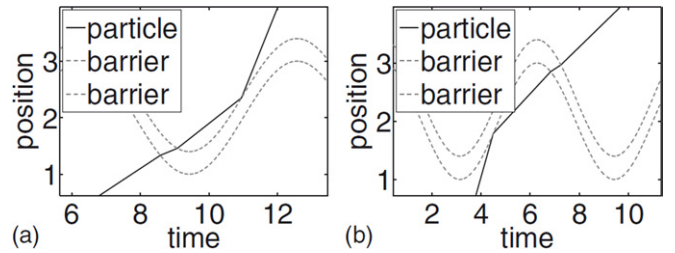


**Figure 43.** Typical trajectories for (a) acceleration case and (b) deceleration case. Reproduced with permission from [196]. Copyright 2008 American Physical Society.

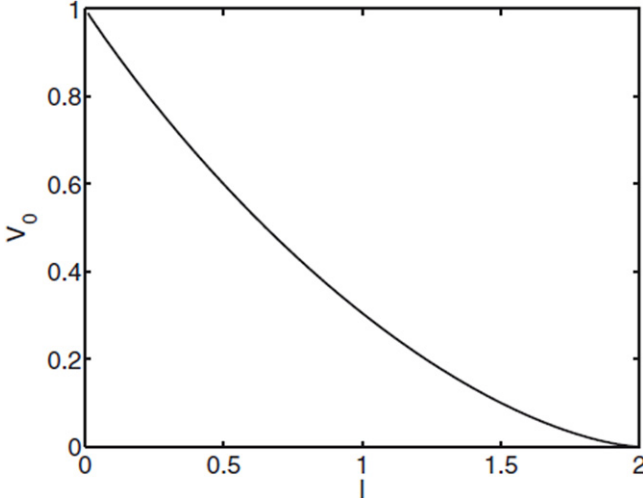


**Figure 42.** Maximum barrier potential allowing for periodic orbits as a function of the barrier's thickness. Reproduced with permission from [196]. Copyright 2008 American Physical Society.

leading to singularities, which can only be the case if the interaction time in continuous systems or the number of interactions in discrete systems between target and particle diverges as well [32].

The dwell times of sticky particles have a typical probability distribution. Figure 45 shows the distribution of dwell times for a total of more than  $10^{10}$  initial conditions randomly chosen. The dwell-time function or scattering function distribution (also called the delay-time function

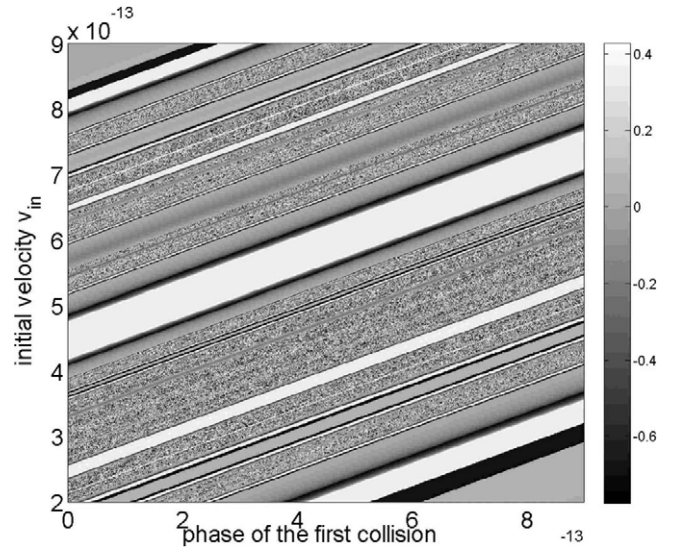


**Figure 44.** Typical fractal structure of the driven barrier model. Reproduced with permission from [196]. Copyright 2008 American Physical Society.

distribution) can be approximated by a power law  $P(t_d) \sim t_d^\gamma$  becoming  $\gamma = -2.5$ . This distribution of dwell times is typical in nonhyperbolic chaotic scattering problems due to the existence of KAM islands in the phase space [191].

## 6. Fractal dimension in chaotic scattering

One of the most important aspects of a set is its dimension. In this section, we provide some classical techniques to

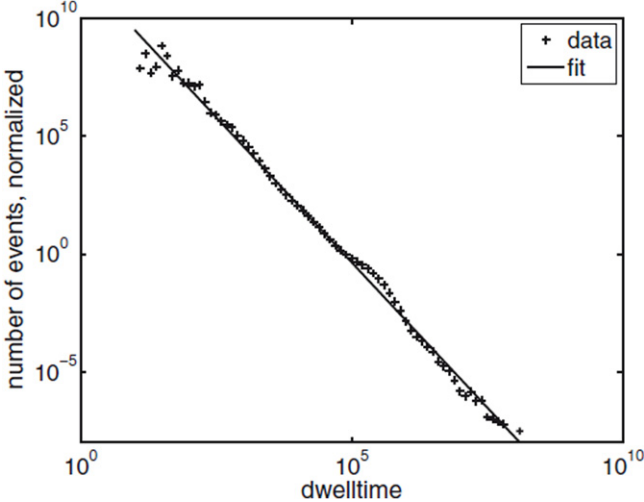


**Figure 45.** Picture of the distribution of the sticking times in which we can observe a power law with exponent  $\gamma = -2.5$ . Reproduced with permission from [196]. Copyright 2008 American Physical Society.

estimate the fractal dimension of the typical sets appearing in chaotic scattering phenomena. We also provide some algorithms for the computation of the dimension and describe the typical procedure to estimate the fractal dimension in chaotic scattering problems.

### 6.1. Definition and utility of the fractal dimension in chaotic scattering

One common definition to estimate the dimension of a fractal set is the box-counting dimension [3, 24, 203].

The box-counting dimension provides a relatively simple way to compute the dimension of a set. On the other hand, there are certain kinds of sets in which their dimensions are not integers. Such sets are named fractal by Benoit Mandelbrot [204], while, in the context of dynamics, attracting sets with fractal properties have been named strange attractors [205].

The definition of dimension was originally given by Felix Hausdorff [206]. This definition is somewhat more involved than the box-counting dimension, but it has some specific advantages. For typical invariant sets encountered in chaotic dynamics, both the box-counting dimension and the Hausdorff dimension are commonly thought to be equal [138].

Concerning the box-counting dimension, we assume that we have a set which lies in an  $N$ -dimensional Cartesian space. We then imagine covering the space by a grid of  $N$ -dimensional cubes of edge  $\varepsilon$ . We then count the number of cubes  $N(\varepsilon)$  needed to cover the set. We do this for successively smaller values of  $\varepsilon$ . The box-counting dimension is given by

$$D_0 = \lim_{\varepsilon \rightarrow 0} \frac{\ln N(\varepsilon)}{\ln(\frac{1}{\varepsilon})}. \quad (42)$$

As an example, consider the case of some simple sets lying in a two-dimensional Cartesian space as shown in figure 46. The three geometrical sets shown in that picture are: a set of two points (a), a curve segment (b) and in (c) the area inside a closed

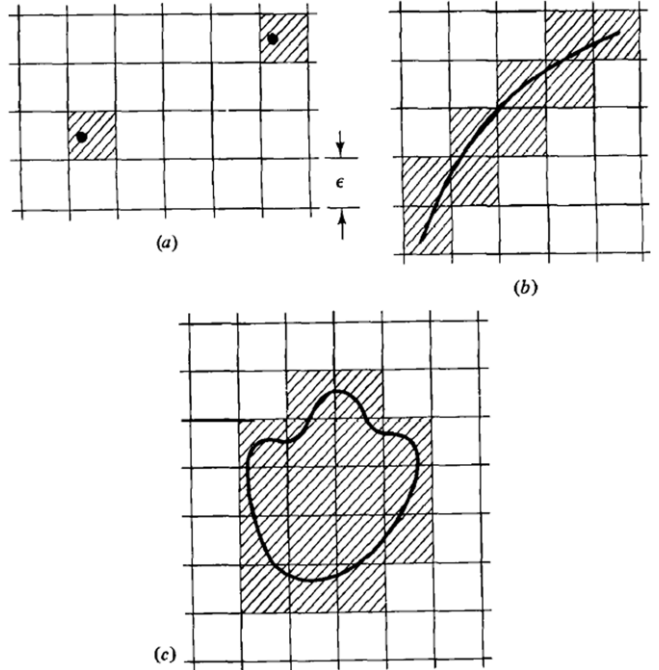


**Figure 46.** Illustration of  $N(\varepsilon)$  for sets consisting of (a) two points , (b) a curve segment, and (c) the area inside a closed curve. Reproduced with permission from [3]. Copyright 2002 Cambridge University Press.

curve. The squares required to cover the sets are shown cross-hatched in the figure. In the case of figure 46(a),  $N(\varepsilon) = 2$  independent of  $\varepsilon$ , therefore  $D_0 = 0$ . On the other hand, in the case of figure 46(b),  $N(\varepsilon) \sim l/\varepsilon$  obtaining that  $D_0 = 1$ . Similarly, for the area  $N(\varepsilon) \sim A/\varepsilon^2$  obtaining that  $D_0 = 2$ . Hence, we see that the box-counting dimension yields correct dimension values for simple nonfractal sets. In the case of a fractal set, for example the Cantor set [207], the box-counting dimension of the middle third Cantor set can be estimated in the following manner. We consider a sequence of  $\varepsilon_n$  of  $\varepsilon$ -values converging to zero as  $n$  approaches infinity. According to equation (42), we have that  $D_0 = \lim_{\varepsilon_n \rightarrow 0} \ln N(\varepsilon_n) / \ln(1/\varepsilon_n)$ . The most convenient choice for  $\varepsilon_n$  is  $\varepsilon_n = (1/3)^n$ . By construction of the Cantor set, we then have  $N(\varepsilon_n) = 2^n$  and therefore  $D_0 = \ln 2 / \ln 3 = 0.63$ .

Hence, we obtain for the dimension a number between zero and one, indicating that the set is a fractal. In general we have that  $N(\varepsilon) \sim \varepsilon^{-D_0}$ , where the number of cubes needed to cover the set increases with  $\varepsilon$  in a power law function with exponent  $D_0$ , where  $D_0$  is the fractal dimension of the set. This method is one of the most typical ways to compute dimensions of fractal sets.

### 6.2. Algorithms to compute the fractal dimension

In chaotic scattering problems, fractal basin boundaries are very typical and common. One of the typical algorithms to compute the dimension of the fractal basin boundaries is by using the uncertainty algorithm [191]. For that purpose, we plot figure 14 in order to describe in one example the procedure for the estimation of the uncertainty dimension. This picture shows two attractors A and B and a simple smooth

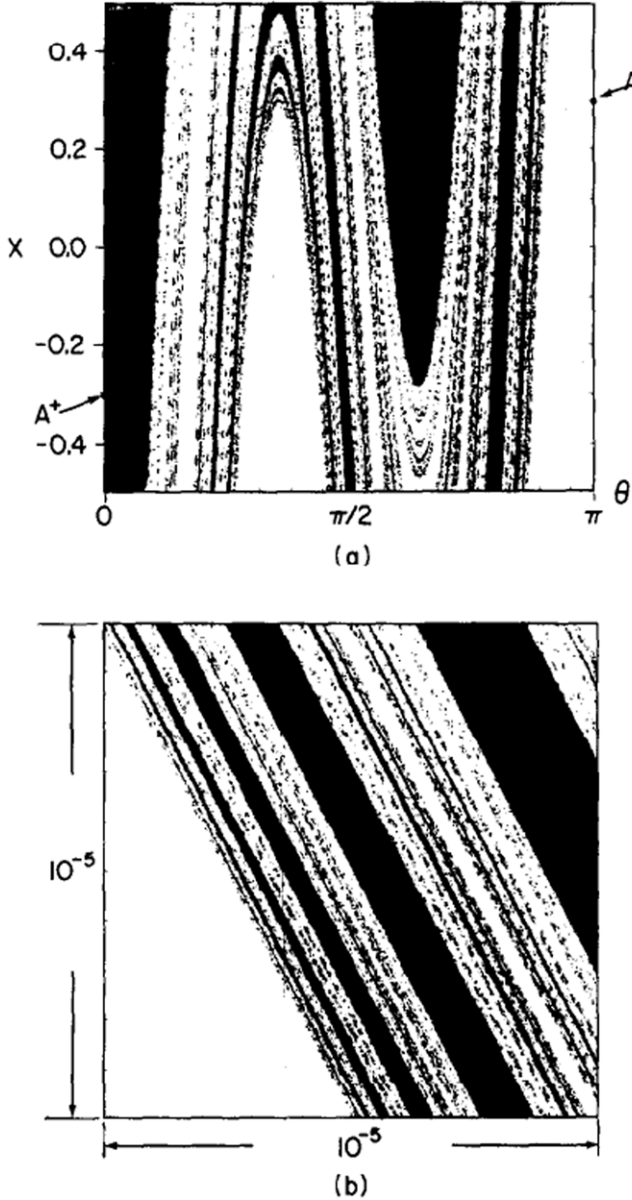


**Figure 47.** (a) Basins of attraction for the two attractors in white and black color, respectively. (b) Magnification of picture (a). Reproduced with permission from [191]. Copyright 1985 Elsevier.

one-dimensional basin boundary separating the finite volume of the phase space; the uncertainty region for initial conditions with uncertainty  $\varepsilon$  is simply determined by thickening the basin boundary by the amount  $\varepsilon$ . Any initial condition in this strip can change from the basin of A to that of B, or vice versa, if perturbed by an amount  $\varepsilon$  or less. The area of this region is proportional to  $\varepsilon$ ; as  $\varepsilon$  is reduced, the *uncertainty fraction* of phase space satisfies  $f(\varepsilon) \sim \varepsilon$ .

For  $f(\varepsilon) \sim \varepsilon$  to be well defined in cases where the phase space of the system is infinite, we shall restrict the initial conditions to lie in some fixed finite subregion of the phase space which contains the basin boundary as shown in figure 47(a). In such a case, the magnitude of  $f(\varepsilon)$  depends on the choice of the subregion. We are interested in the scaling of  $f(\varepsilon)$  as  $\varepsilon$  becomes small. It is believed that this behaviour is independent of the subregion selected. It means that the

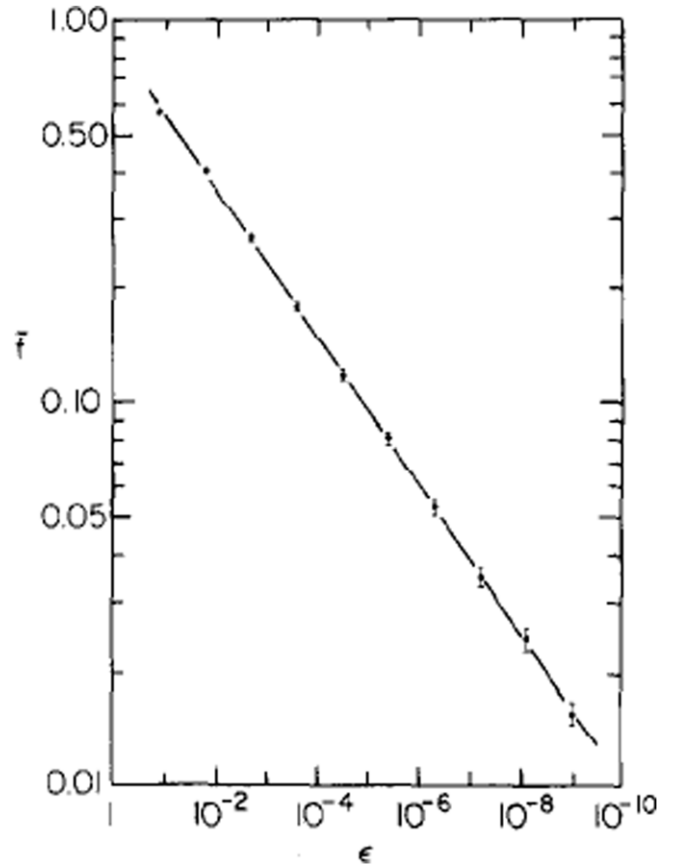


**Figure 48.** Log–log plot of  $f$  versus  $\varepsilon$  for the phase space shown in figure 47. Reproduced with permission from [191]. Copyright 1985 Elsevier.

exponent  $\alpha$  in the equation  $f \sim \varepsilon^\alpha$  is independent of the subregion.

As an example, we consider the phase-space region shown in figure 47 and examine the dependence of the *uncertain fraction* of the phase space  $f(\varepsilon)$  on the uncertainty  $\varepsilon$  [191]. The variation of  $f(\varepsilon)$  versus  $\varepsilon$  for this system is plotted in figure 48. The log–log plot indicates a power law behaviour with exponent 0.2,  $f(\varepsilon) \approx 0.9 \approx \varepsilon^{0.2}$ .

The consequences of such a relationship are remarkable. For an error of 0.125 in the initial conditions the final states of approximately 59% of the initial conditions could not be predicted with certainty. Therefore, we expect such a power law behaviour,

$$f(\varepsilon) \sim \varepsilon^\alpha,$$

to be common in dissipative dynamical systems. The uncertainty exponent  $\alpha$  is related to the dimension of the basin boundary in this way,

$$\alpha = D - d,$$

where  $D$  is the dimension of the phase space and  $d$  is the dimension of the basin boundary.

This expression reduces to the linear relation previously obtained in cases where the basin boundary is a smooth curve. In general, since the basin boundary divides the phase space,

its dimension  $d$  must satisfy  $d \geq D - 1$ . Thus, the existence of noninteger dimension boundaries allows for values  $0 < \alpha \leq 1$ .

Finally, this method is very useful to estimate dimensions in chaotic scattering problems. One of the specific algorithms is explained in the next subsection.

### 6.3. Fractal dimension of the scattering function

One of the most common ways to estimate the fractal dimension in chaotic scattering problem is by computing the fractal dimension of the set of singularities of the scattering function [202].

In fact, an important result in nonhyperbolic chaotic scattering concerns the fractal dimension of the set of singularities in the scattering function. Lau *et al* [202] argue, with numerical support, that the dimension is  $D = 1$ . This unity of the fractal dimension is a direct consequence of the algebraic-decay law associated with nonhyperbolic chaotic scattering, which can be seen intuitively by considering a zero Lebesgue measure Cantor set that has  $D = 1$ , through the following construction. Start with the unit interval  $[0, 1]$  and remove the open middle third interval. From each of the two remaining intervals remove the middle fourth interval.

Then from each of the four remaining intervals remove the middle fifth, and so on. At the  $n$ th stage of the construction, there are  $N = 2^n$  subintervals, each of length:  $\varepsilon_n = [2/(n+2)]2^{-n}$ . The total length of all subintervals  $\varepsilon_n N \sim n^{-1}$  goes to zero *algebraically* as  $n \rightarrow \infty$ . In order to cover the set with intervals of size  $\varepsilon_n$ , the required number of intervals is  $N(\varepsilon) \sim \varepsilon^{-1}(\ln \varepsilon^{-1})^{-1}$ . The box-counting dimension of the set is then

$$D = \lim_{\varepsilon \rightarrow 0} \frac{\ln N(\varepsilon)}{\ln \varepsilon^{-1}} = 1.$$

Note that  $D$  is the exponent of the dependence  $N(\varepsilon) \sim 1/\varepsilon^D$ , to which the weak logarithmic dependence does not contribute. However, it is the logarithmic term which is responsible for ensuring that the Lebesgue measure is zero:  $\varepsilon N(\varepsilon) \sim (\ln \varepsilon^{-1})^{-1} \rightarrow 0$  as  $\varepsilon \rightarrow 0$ . More generally, if at each stage a fraction  $\eta_n = \alpha/(n+c)$ , where  $\alpha$  and  $c$  are constants, is removed from the middle of each of the  $2^n$  remaining intervals, then

$$N(\varepsilon) \sim \frac{1}{\varepsilon} \left( \ln \frac{1}{\varepsilon} \right)^{-\alpha}. \quad (43)$$

An interesting observation is that the slope of the curve  $\ln N(\varepsilon)$  versus  $\ln \varepsilon^{-1}$ , which is  $d \ln N(\varepsilon)/d(\ln \varepsilon^{-1})$ , is always less than 1 for small  $\varepsilon$ , but it approaches 1 logarithmically as  $\varepsilon \rightarrow 0$ . Thus, the result  $D = 1$  still holds. A practical implication is that for fractals whose general characters are similar to this example, an accurate numerical estimation of the dimension will require going to very small scales. As the scale is decreased, the numerically determined value of the dimension will increase toward 1.

The relevance of the above construction of the Cantor set to chaotic scattering can be seen, as follows [202]. Consider particles launched from a line segment straddling the stable manifold of the chaotic saddle. There is then an interval of input variables which leads to trajectories that remain in the scattering region for at least a duration of time  $T_0$ . By time  $2T_0$

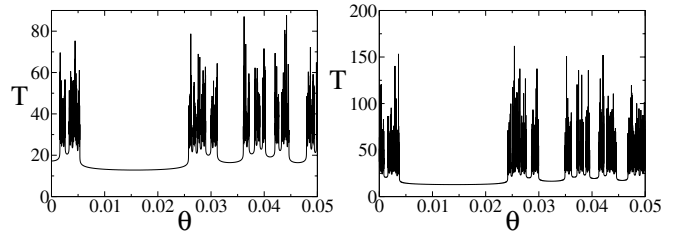


**Figure 49.** Typical delay-time function for the conservative (left) and the weakly dissipative (right) Hénon–Heiles system with chaotic scattering ( $E = 0.19$ ,  $\alpha = 10^{-4}$  and  $\beta = 10^{-4}$ ).

a fraction  $\eta$  of these particles have left. If the initial conditions of these escaping particles are all located in the middle of the original interval, there are then two equal-length subintervals of the input variable which lead to trajectories that remain at least for time  $2T_0$ . By time  $3T_0$  an additional fraction  $\eta$  of the particles, whose initial conditions are located in the middles of the two subintervals remaining at time  $2T_0$ , escape. There are then four subintervals, particles initiated from which can remain in the scattering region for at least  $3T_0$ , and so on. The resulting set is a Cantor set of Lebesgue measure zero on which particles never escape. The box-counting dimension of the Cantor set is given by

$$D = \frac{\ln 2}{\ln [(1-\eta)/2]^{-1}}.$$

If the scattering is hyperbolic, particles escape exponentially from the scattering region:  $P(t) \sim e^{-\gamma t}$ , where  $P(t)$  is the survival probability of a particle and the decay rate  $\gamma$  is determined by the fraction  $\eta$  as:  $\gamma = T_0^{-1} \ln(1-\eta)^{-1}$ . While the above picture reflects the hyperbolic dynamics relatively accurately, for nonhyperbolic dynamics it is more complicated, even with modifications. In particular, because of the algebraic decay in nonhyperbolic chaotic scattering:  $P(t) \sim t^{-z}$ , the fraction  $\eta$  is no longer a constant: it varies at each stage of the construction of the Cantor set. At the  $n$ th stage ( $n$  large), the fraction  $\eta_n$  is approximately given by:  $\eta_n \approx -T_0 P^{-1} dP/dt \approx z/n$ , which yields equation (43) and hence a Cantor set with dimension 1, where  $\alpha$  in equation (43) is identified to be the algebraic-decay exponent  $z$ .

In the dissipative case, the scattering dynamics become hyperbolic with an exponential decay. The dimension of the Cantor set immediately decreases from unity as a dissipation parameter is turned on. This observation was verified numerically using a two-dimensional map [208].

Figures 49(a) and (b) show, for  $E = 0.19$  in the conservative and the dissipative (with the dissipative force proportional to the velocity in the form  $(\alpha \dot{x}, \beta \dot{y})$ , with  $\alpha = 10^{-4}$  and  $\beta = 10^{-4}$ ) case, respectively, the delay-time function for scattering trajectories. To generate these figures,  $n = 250$  particles are chosen at  $y = 0$  with the initial direction  $\theta$  varying systematically from 0 to 0.05. We observe typical features of chaotic scattering in both cases: the functions contain both smooth parts and discontinuities and, in fact, they are singular on a fractal set. At the scale shown, the two plots exhibit qualitatively similar features. However, the fractal dimensions of the set of singularities in the two functions are markedly

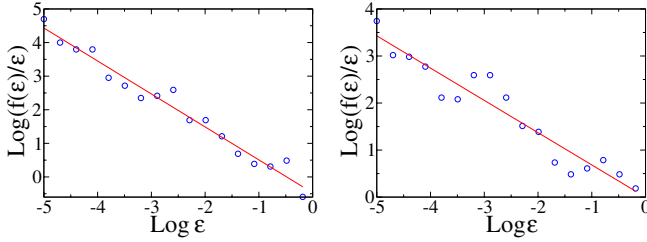


**Figure 50.** For  $E = 0.19$  in the Hénon–Heiles system so that there is chaotic scattering, algebraic scaling of  $f(\epsilon)/\epsilon$  with  $\epsilon$ . The absolute value of the slope from a linear fit gives a good estimate for the fractal dimension of the set of singularities in the delay-time function. We obtain  $D = 0.97 \pm 0.01$  for the conservative case and  $D = 0.71 \pm 0.02$  for the weakly dissipative case. Reproduced with permission from [19]. Copyright 2006 American Institute of Physics.

different, with the dimension value close to and less than unity in the conservative and dissipative case, respectively. To demonstrate this, we use the uncertainty algorithm [191] to numerically calculate the fractal dimension. In particular, for a fixed value of the ‘uncertainty’  $\epsilon$ , we randomly choose an initial condition  $\theta_0$  and compute  $|T(\theta_0) - T(\theta_0 + \epsilon)|$ . If  $|T(\theta_0) - T(\theta_0 + \epsilon)| > h$ , where  $T$  is the delay time and  $h$  is a positive number, we say that  $\theta_0$  is uncertain with respect to  $\epsilon$ . Otherwise  $\theta_0$  is certain. Many random initial conditions can be chosen, which yield  $f(\epsilon)$ , the fraction of the uncertain initial conditions. The quantity  $f(\epsilon)/\epsilon$  typically scales with  $\epsilon$  as

$$f(\epsilon)/\epsilon \sim \epsilon^{-D},$$

where  $D$  is the uncertainty dimension that is believed to have the same value as the box-counting dimension for typical dynamical systems [209]. Figures 50(a) and (b) show, for the Hénon–Heiles system in the conservative and the dissipative ( $\alpha = 10^{-4}$  and  $\beta = 10^{-4}$ ) case,  $f(\epsilon)/\epsilon$  versus  $\epsilon$  on a logarithmic scale, where the constant  $h$  is chosen (arbitrarily) to be  $h = 0.01$ . For figure 50(a), the estimated slope from a least-squares linear fit is  $D = 0.97 \pm 0.01 \approx 1$ . While for figure 50(b), the estimated slope is  $D = 0.71 \pm 0.02 < 1$ . Thus, the result that the fractal dimension decreases immediately from unity in the presence of weak dissipation, established previously exclusively for discrete-time maps, holds true for continuous-time Hamiltonian chaotic scattering systems as well.

On the other hand, in the case of noisy systems [210], the value of the fractal dimension is very close to one as typically happens in the stochastic systems. Finally, one of the major routes to chaotic scattering is through an abrupt bifurcation by which a nonattracting chaotic saddle is created as a system parameter change through a critical value [211]. In this situation, the fractal dimension can change discontinuously at the bifurcation point.

## 7. Experimental systems with chaotic scattering

In this section we provide some examples of experimental results in which chaotic scattering phenomena appear.

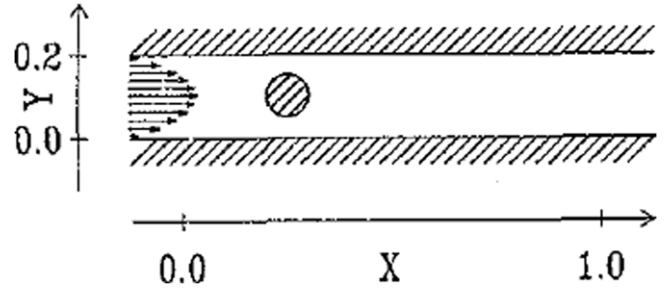


**Figure 51.** Classical geometry of the channel and the cylinder obstacle. Reproduced with permission from [212]. Copyright 1993 American Institute of Physics.

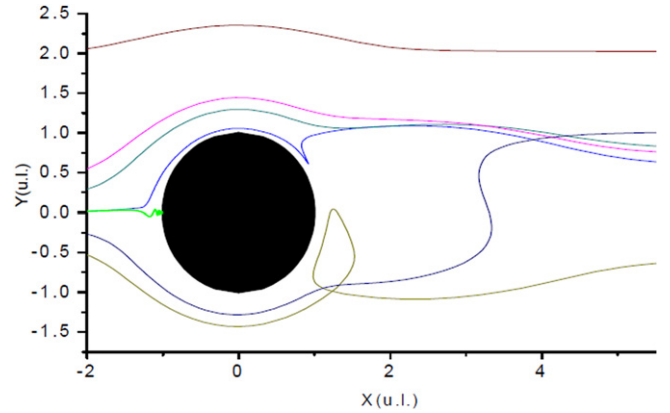


**Figure 52.** This picture shows typical trajectories of the particles for different initial conditions. Both regular and chaotic motions take place around the cylinder.

### 7.1. Hydrodynamical flows

Here we describe some phenomena related to chaotic scattering in open flows. We focus in the problem of particles moving through a cylinder obstacle. This is the Von Karman street flow [212].

**7.1.1. Introduction.** The passive transport of particles in hydrodynamical flows provides a nice application to chaotic scattering phenomena [212–215]. The case of chaotic particle transport in open chaotic flows can be relevant in problems related to mixing in continuous flow reactors. The chaotic motion of a passive particle can then be considered as a realization of transient Lagrangian turbulence. The Hamiltonian structure of the dynamics and the openness of the flow make advection analogous to particle scattering.

The typical situation for this study is the case of a straight channel containing a cylinder obstacle, as shown in figure 51. Typical trajectories of the particles in this kind of flow are shown in figure 52, in which different colors denote trajectories with different initial conditions.

On the other hand, a clear criterion for transient chaos is the occurrence of a fractal set of singularities in the scattering function [216]. Figures 53(a), (b) and (c) represent this kind of behaviour very clearly. Applications of open flows to the fate of aerosols have been shown in [217]. There, the dynamics of aerosols both in the absence and presence of gravitational effects, and both when the dynamics

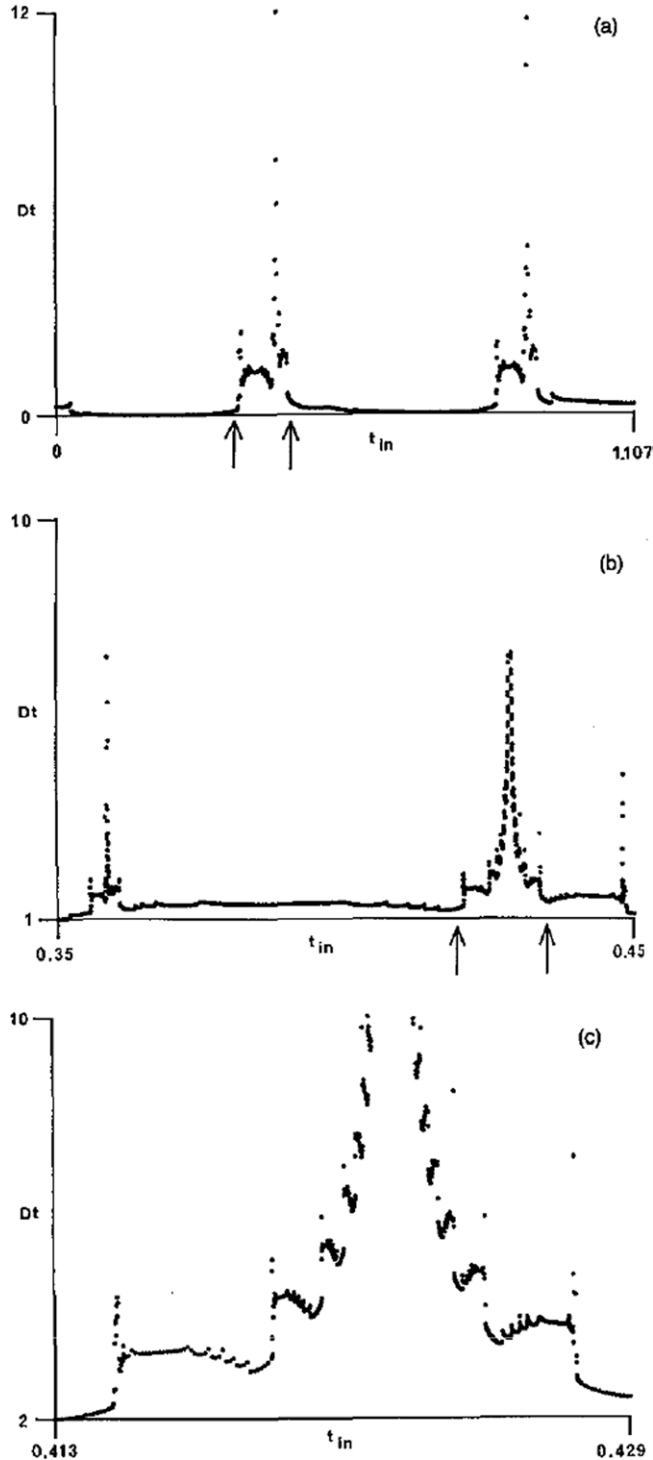


**Figure 53.** Plot of the scattering function: (a) shows this function on its whole domain, (b) and (c) show a magnification of (a). Reproduced with permission from [212]. Copyright 1993 American Institute of Physics.

of the fluid particles is hyperbolic and nonhyperbolic is carried out. The presence of multiple vortices in the flow produces permanent trapping of aerosols. Another interesting application to investigate the dynamics of passive particles in a two-dimensional incompressible open flow composed of a fixed topographical point vortex has been carried out in [218]. The motivation of this last paper was the study of topographic

vortices over mountains in the ocean and atmosphere. Here, the tracer dynamics is typically chaotic in a mixing region and regular in far upstream and downstream regions of the flow.

**7.1.2. Experimental evidence.** We present here the first experimental evidence of chaotic scattering in a fluid wake [219]. Measurements of tracer particles and dye in the stratified wake of a moving cylinder are shown to be consistent with the predictions based on numerical simulations. As we have explained throughout this manuscript, one spectacular manifestation of chaotic scattering is that a generic scattering function exhibits an uncountable number of singularities, located on a fractal support in the space of the impact parameters. In the case of a fluid wake, typically the scattering function is taken of the fluid elements passing the perturbing body to be the scattering variable. Unfortunately, exhibiting an actual scattering function is hardly practical for a real fluid wake, where an accurate determination of the impact parameter of a fluid element existing in the wake region is currently impossible. The authors in [219] present several interlocking pieces of evidence consistent with the two-dimensional scattering model introduced in [212, 220–222].

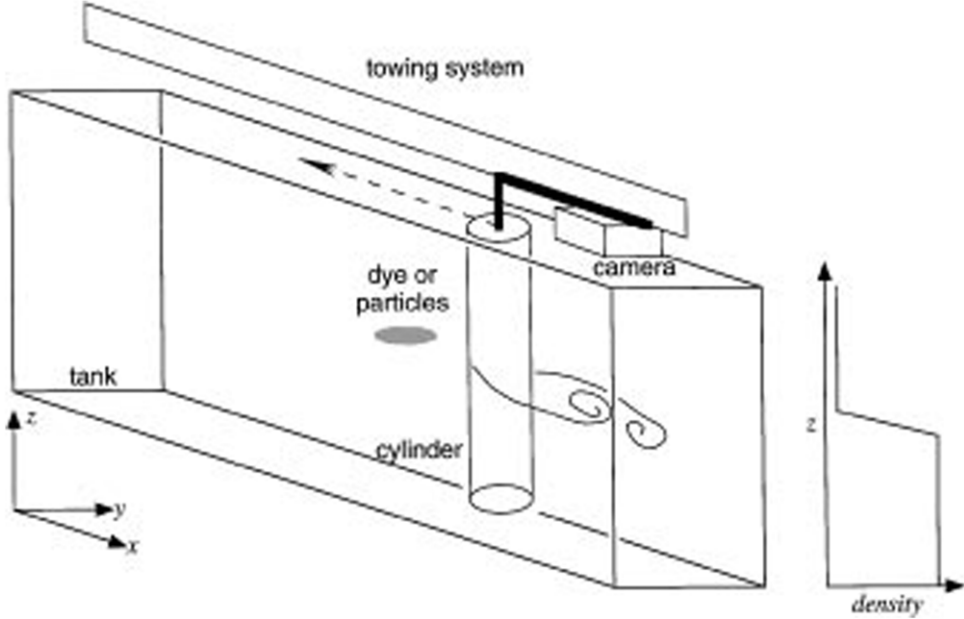
The experiments carried out in [219] were conducted in the Applied Physics Laboratory of the John Hopkins University. They used the  $1 \text{ m} \times 3 \text{ m} \times 8 \text{ m}$  stratified flow facility, which allows experiments with arbitrary stable density profiles, as shown in figure 54. The measurements have been made within the thin mixing layer. This very strong stratification suppressed motion in the vertical direction, especially on time scales characteristic of fluid motion in the horizontal directions. The fluid wake was created by a cylinder moving horizontally along the center of a channel between false walls.

The flow field in the wake is dominated by vortices formed behind the cylinder, alternating sides in the cross-stream direction. The nearby walls and viscosity quickly suppress the vorticity, so the entire von Karman street is reduced to only two vortices at any time.

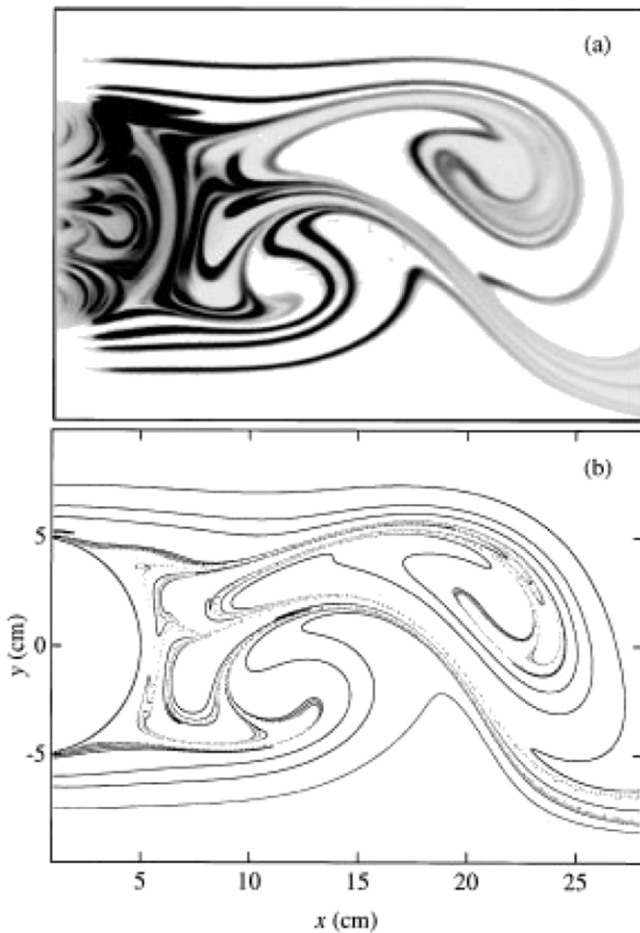
The comparison between the computed streaklines with observed dye lines produced by a comb of outlets upstream from the cylinder was excellent, as shown in figure 55.

Figure 56 shows the unstable periodic orbits in the wake of the cylinder revealed by particle tracking. Finding experimental periodic orbits is not expected since the periodic orbits predicted numerically are extremely unstable. In the experiment, the approach was to move the cylinder through a horizontal sheet of tiny tracer particles and record the particle tracks with the CCD camera.

Figure 57 shows the scattering function for dye interacting with the wake. This picture is complicated to perform experimentally by the fact that fluid elements are delayed by the chaotic saddle and the wall of the cylinder. Therefore the scattering function of the earliest fluid elements leaving the wake is considered. Longer delays show a more complicated time dependence than the predicted simple  $t^{-2}$  algebraic decays, as shown in figure 57. In any case, the discrepancy between the curves plotted in this picture is irrelevant to the argument for chaotic scattering.



**Figure 54.** Picture of the experimental setup (see text for details). Reproduced with permission from [219]. Copyright 1996 American Physical Society.



**Figure 55.** Image of experimental flow field (a) shown above corresponding numerically computed streaklines (b) at  $Re = 100$ . Reproduced with permission from [219]. Copyright 1996 American Physical Society.

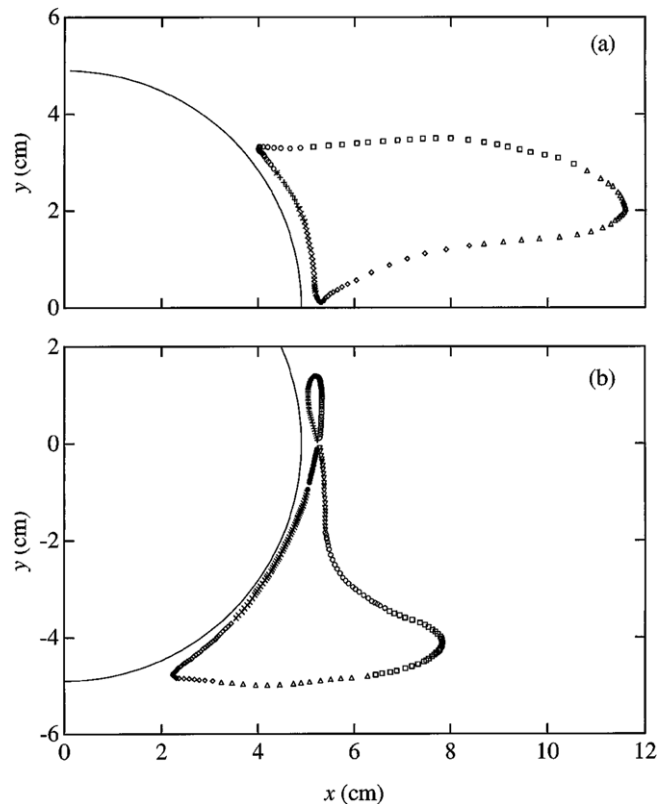


**Figure 56.** Picture of unstable periodic orbits in the wake revealed by particle tracking. (a) Period-1 orbit at  $Re = 100$ . (b) Period-1 orbit at  $Re = 250$ . Reproduced with permission from [219]. Copyright 1996 American Physical Society.

## 7.2. Optical systems

Here, experimentally observed fractal patterns of chaotic light scattering in a regular polyhedral mirror ball structure, are shown [223]. The fractal dimension of this kind of structure is also analyzed.

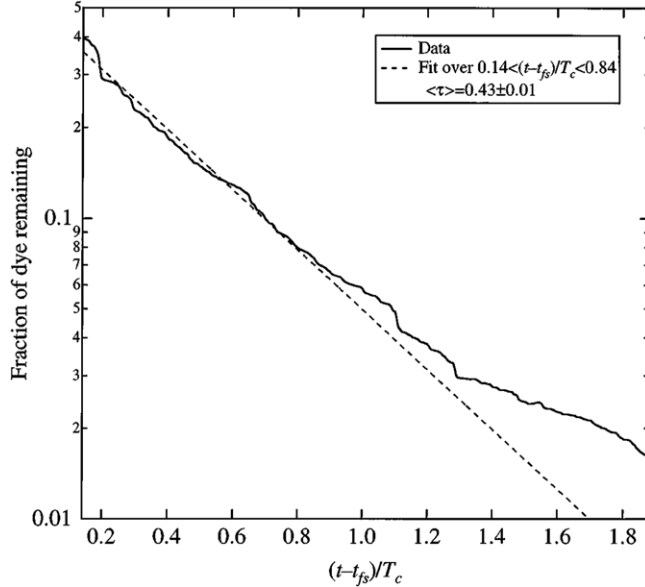


**Figure 57.** Average scattering function for dye interacting with the wake. Notice that an average is taken over eight runs with different upstream placements of this dye stripe. Notice that  $T_c$  represents the period of the velocity field. Reproduced with permission from [219]. Copyright 1996 American Physical Society.

As an example of a fractal optical device, a three-dimensional optical billiard has been proposed [178, 224], in which the centers of four spherical reflectors are located at the vertices of a regular tetrahedron. Light was injected into the optical billiard and fractal patterns of light scattering with the Wada basin property were found [126, 225, 226]. A similar configuration has been used as a chaos mirror [192], which provides free-space optical beam links for optical wireless networks. The characteristics of fractal optical devices need to be well understood to investigate the behaviour of photons in fractal optical devices. The analysis of the fractal dimension exposed in the previous section which can be found in [3], is one of the basic characteristics of fractal structures.

**7.2.1. Experimental evidence.** The idea of an extension of the optical billiard and the chaos mirror with a tetrahedral structure [178, 192, 224] to regular polyhedral mirror ball structures is carried out in [223]. Figure 58 shows five examples of regular polyhedral mirror ball structures. These ones correspond to a regular tetrahedron (a), regular hexahedron (b), regular octahedron (c), regular dodecahedron (d) and regular icosahedron (e), respectively. The centers of the spherical reflectors are located at the vertices of a polyhedron whose edge length is equal to the diameter of the spherical reflectors. Each of the spheres is in contact with the nearest-neighboring spheres.

To observe chaotic light scattering in regular polyhedral mirror structures, light emitting diodes (LEDs) with different colors are located at the center of the faces of the polyhedra. In the previous paper, the authors used  $N - 1$  LEDs with different colors on the face of the polyhedron, where  $N$  is the number of faces.

The light beams from the LEDs are injected and scattered in the mirror ball structure. Figure 59 shows the picture of the

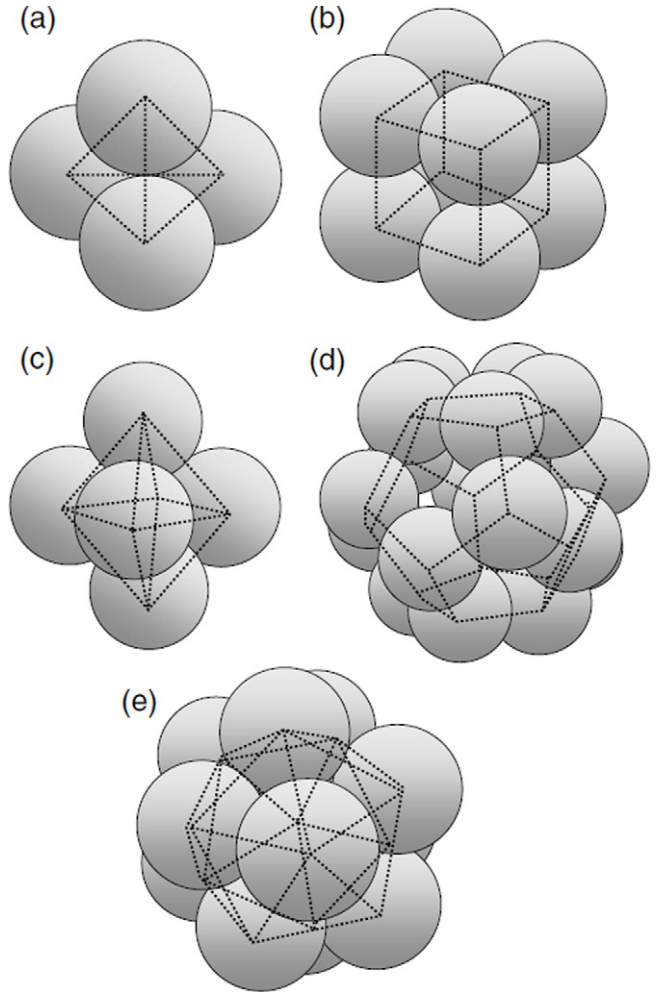


**Figure 58.** (a) Regular tetrahedron mirror ball structure, (b) regular hexahedron, (c) regular octahedron, (d) regular dodecahedron and (e) regular icosahedron. Reproduced with permission from [223]. Copyright 2007 American Physical Society.

light scattering patterns in the five regular polyhedral mirror ball structures. Self similarity of the light scattering patterns is observed as a fractal. For the tetrahedral structure shown in figure 59(a), many triangle patterns with different colors and sizes are shown in the triangle region with some contraction ratios. These triangle patterns indicate the light source coming from one of the faces of the tetrahedron, which is considered as a set of initial conditions of the light scattering. These color patterns can be called basins [178]. These basins typically have fractal structure and their boundaries are, in general, complex [3, 178]. The complexity of the basin boundaries increases, insofar as the number of faces of the polyhedral mirror ball structure increases. The fractal dimension of every kind of structure is analyzed in the next subsection.

**7.2.2. Fractal dimension.** In [223], models for the observed fractal patterns in the five regular polyhedral mirror ball structures based on the experimental observation of figure 59 were created. Those models are shown in figure 60. The color pattern indicate the basins of light scattering corresponding to the faces of the polyhedron. The corresponding basin

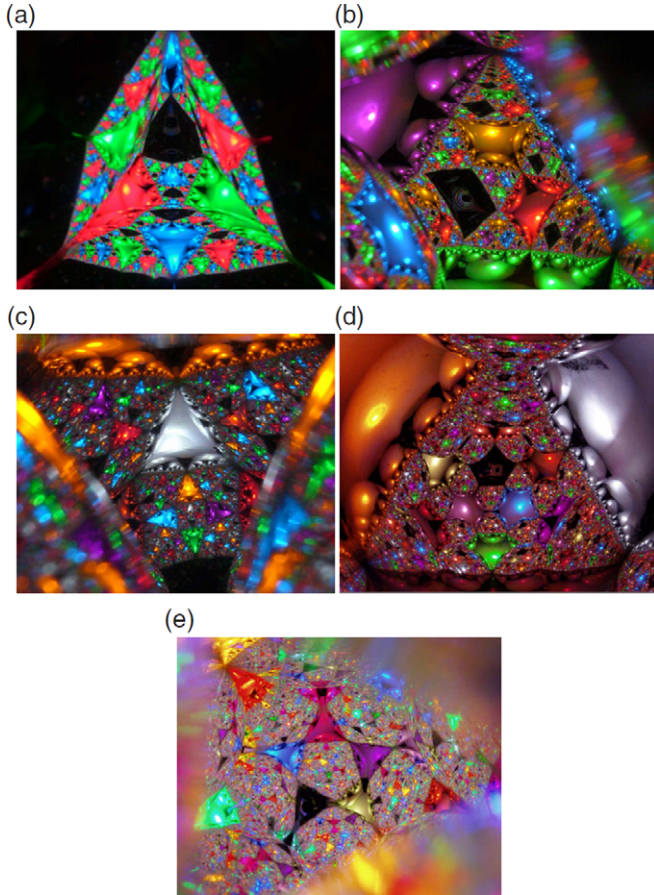


**Figure 59.** Plot of fractal patterns of chaotic light scattering in the five regular polyhedral mirror ball structures, (a) regular tetrahedron, (b) regular hexahedron, (c) regular octahedron, (d) regular dodecahedron and (e) regular icosahedron. Reproduced with permission from [223]. Copyright 2007 American Physical Society.

boundaries of these five kinds of structures are shown in figure 60.

The estimation of the fractal dimension is carried out using both, the self-similar dimension and the box-counting dimension [3]. An estimation of the fractal dimension of the basin boundaries for the five polyhedra structures is shown in figure 61. We can imagine that as the number of iterations  $n$  is increased, the box-counting dimension increases and saturates at a certain value, which corresponds to a reliable value of the box-counting dimension.

A summary of both estimations of the fractal dimension of the 5 polyhedral structures is shown in figure 61. It is found that the fractal dimension increases as the number of faces of the polyhedral structure increases, except the dodecahedral structure [223]. Finally, the fractal dimension obtained in this subsection may be an important measure to characterize optical scattering devices with fractal structures since it may be related to the  $Q$  value as optical confinement devices. Finally, recent studies have been carried out on the propagation of light in foams; patterns are created which are generated due to the reflection and refraction of light. In that work [227] the authors found that one of these patterns is observed by the formation of multiple mirror images inside a liquid bridge in a layer of bubbles in a Hele–Shaw cell [228].

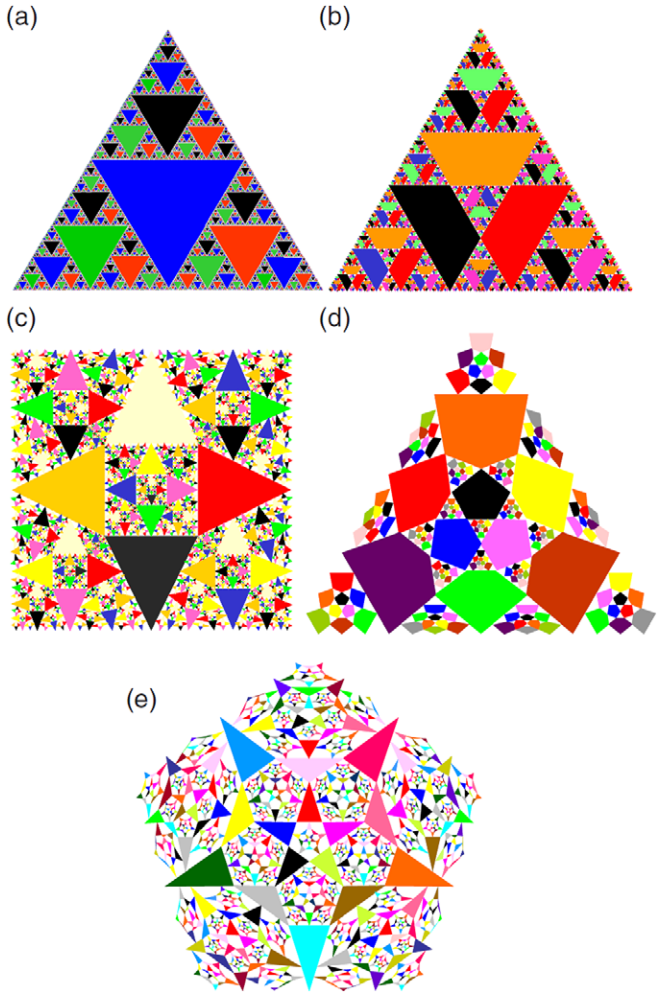


**Figure 60.** Models of fractal patterns of chaotic light scattering in the five regular polyhedral mirror ball structure, (a) regular tetrahedron, (b) regular hexahedron, (c) regular octahedron, (d) regular dodecahedron and (e) regular icosahedron. Reproduced with permission from [223]. Copyright 2007 American Physical Society.

## 8. Effects of weak perturbations in chaotic scattering

An important issue in the study of nonlinear dynamics is to understand how robust a phenomenon is against perturbations or deviations between the underlying mathematical model and the physical reality. In the case of chaotic scattering, most theoretical works focused on purely Hamiltonian or conservative systems. In this section we address the effects of physical perturbations, in particular, weak dissipation and noise on chaotic scattering.

### 8.1. Dissipative chaotic scattering

In a realistic physical situation, weak dissipation can be expected. For example, in the study of chaotic advection in two-dimensional hydrodynamical flows [229–231], a tacit assumption is that the underlying flow is incompressible and the advecting particles have zero mass and inertia. This allows the problem to be cast in the framework of Hamiltonian dynamics, as the particle velocities can be related to the flow's

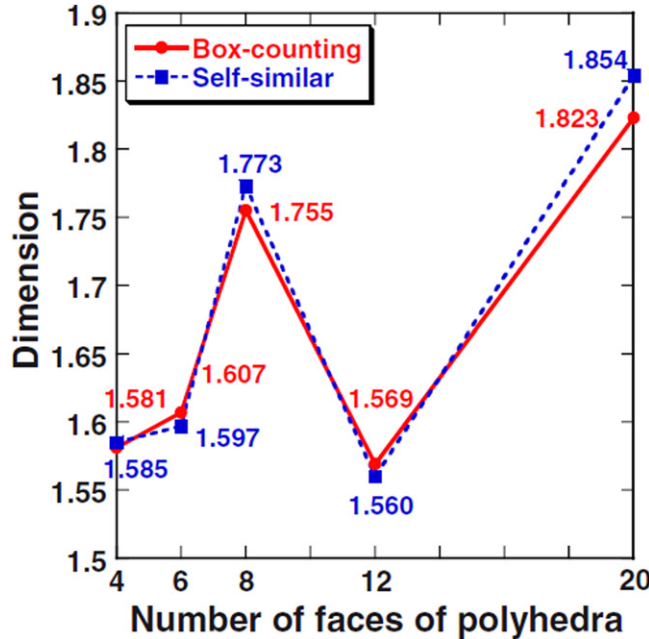


**Figure 61.** Both the self-similar dimension and the box-counting dimension for the polyhedra structures. Reproduced with permission from [223]. Copyright 2007 American Physical Society.

stream function in a way that is completely analogous to the Hamilton equations in classical mechanics. However, real hydrodynamical flows are not perfectly incompressible and particles have finite size and mass, which can effectively induce dissipation in the advective dynamics [232].

An earlier work [208] studied the effect of weak dissipation on two different types of chaotic scattering dynamics: hyperbolic and nonhyperbolic. Intuitively, since weak dissipation can be regarded as small perturbation, we expect it to have little effect on hyperbolic chaotic scattering, because of the structural stability of this type of scattering dynamics. For nonhyperbolic chaotic scattering, which is structurally unstable due to the coexistence of KAM tori and chaotic invariant sets in the phase space, weak dissipation can have a drastic effect on the scattering dynamics. It is thus only necessary to focus on nonhyperbolic chaotic scattering. A relatively complete physical understanding of the effect of weak dissipation can be obtained by addressing how it alters the following three fundamental characteristics of chaotic scattering: (a) particle-decay law, (b) fractal dimension of the set of singularities in scattering functions and (c) scattering basin topology in the phase space.

**8.1.1. Effect of weak dissipation on particle-decay law.** In nonhyperbolic chaotic scattering in Hamiltonian systems, the particle-decay law is algebraic [27, 233]. Weak dissipation can turn KAM tori into periodic attractors [208]. As a result, the original nonattracting chaotic invariant set responsible for chaotic scattering undergoes a boundary crisis bifurcation to a set that generates fractal basin boundaries [191] typically arising in dissipative dynamical systems. The algebraic-decay law in the conservative case will then become exponential in the dissipative case, no matter how weak the dissipation is.

Insights into the switch in the decay law from algebraic to exponential can be gained by considering the classical model of hierarchical construction of Cantor sets in the unit interval. First, an open subinterval in the middle of the unit interval is removed. Next, from each one of the remaining subintervals, the same fraction from the middle is removed, and so on. Each step of this scheme can be thought of as an iteration of the hyperbolic tent map with a slope larger than 2. The total length that remains decays exponentially with the number of iterations and the resulting Cantor set has a fractal dimension smaller than 1. This scenario corresponds to hyperbolic chaotic scattering. When weak dissipation is present, the skeleton of the underlying chaotic set is formed by periodic orbits. The structural stability guarantees the survival of all periodic orbits under small changes in the system parameters. Accordingly, the structure of the Cantor set in the presence of a small amount of dissipation is expected to be unchanged.

For nonhyperbolic chaotic scattering, the same construction can be applied except that the fraction removed at each step decreases with time, e.g. is inversely proportional to time. This simple reduction of the fraction removed captures the essence of the effect of KAM tori [202]. The remaining length decays algebraically with time and, even though the measure of the remaining set approaches zero asymptotically, the resulting Cantor set has dimension 1 [202]. Under weak dissipation, marginally stable periodic orbits in the KAM islands can become stable, turning nearby phase-space regions into parts of basins of attraction [234]. This means that some of the previous chaotic set now become basins of attraction. Important for the scattering dynamics is the fact that the converted subset supports orbits in the vicinity of the KAM islands that otherwise would be scattered after a long, algebraically distributed time, which were responsible for the nonhyperbolic nature of the scattering dynamics in the conservative case. Due to the existence of dense orbits in the original chaotic set, the noncaptured part of the invariant set remains in the boundaries of the basins of the periodic attractors. Consequently, the invariant set is the asymptotic limit of the boundaries between scattered and captured orbits, rather than those between scattered and trapped orbits in the conservative case. Chaos occurs on the nonattracting invariant set whose stable manifold becomes the boundary separating the basins of the attractors and of the scattering trajectories. This reasoning suggests that the structure and the meaning of the Cantor set are altered by weak dissipation. In particular, in successive steps we remove a constant instead of a decreasing fraction in the middle of each interval. The scattering dynamics becomes hyperbolic with exponential particle-decay law.

To demonstrate the effect of weak dissipation on the scattering dynamics, we use the dissipative version [208, 213, 235] of the scattering map proposed originally by Lau *et al* [202]. The map reads

$$\begin{aligned} x' &= \lambda[x - (x + y)^2/4 - \nu(x + y)], \\ y' &= \lambda^{-1}[y + (x + y)^2/4], \end{aligned} \quad (44)$$

where  $\lambda > 1$  is an energy parameter and  $\nu$  is a dissipation parameter. The conservative version of the map ( $\nu = 0$ ) has

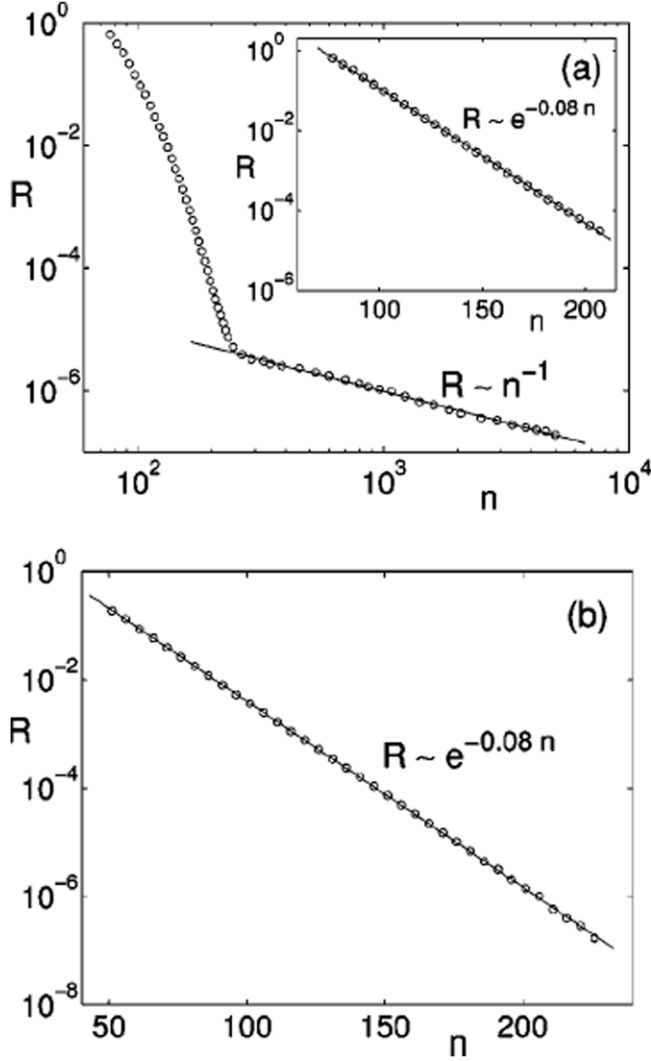


**Figure 62.** For the map equation (44) used in [208] to study the effect of weak dissipation on nonhyperbolic chaotic scattering, (a) decay law in the conservative case, where the inset depicts the short exponential decay preceding the algebraic decay and (b) exponential decay when a small amount of dissipation ( $v = 10^{-3}$  in the map model). Reproduced with permission from [208]. Copyright 2001 American Physical Society.

been used to establish that, in nonhyperbolic chaotic scattering, the fractal dimension of the set of singularities in a scattering function is unity [202]. In particular, it was demonstrated that for  $\lambda \leq 6.5$ , chaotic scattering is nonhyperbolic while it is hyperbolic for  $\lambda \geq 6.5$ . Weak dissipation can be conveniently applied to the system by setting  $v > 0$ . The particle-decay law can be calculated by approximating the survival probability of a particle in the scattering region by  $R(n)$ , the fraction of the number of particles still remaining in the scattering region (defined by  $x^2 + y^2 < 100$ ) at time  $n$ . A typical algebraic-decay behaviour for the conservative case is shown in figure 62(a) and the exponential decay in the presence of weak dissipation ( $v = 10^{-3}$ ) is shown in figure 62(b). Similar results have also been obtained for a continuous-time scattering system [19].

#### 8.1.2. How weak dissipation alters the fractal dimension.

In experimental situations, scattering functions are often

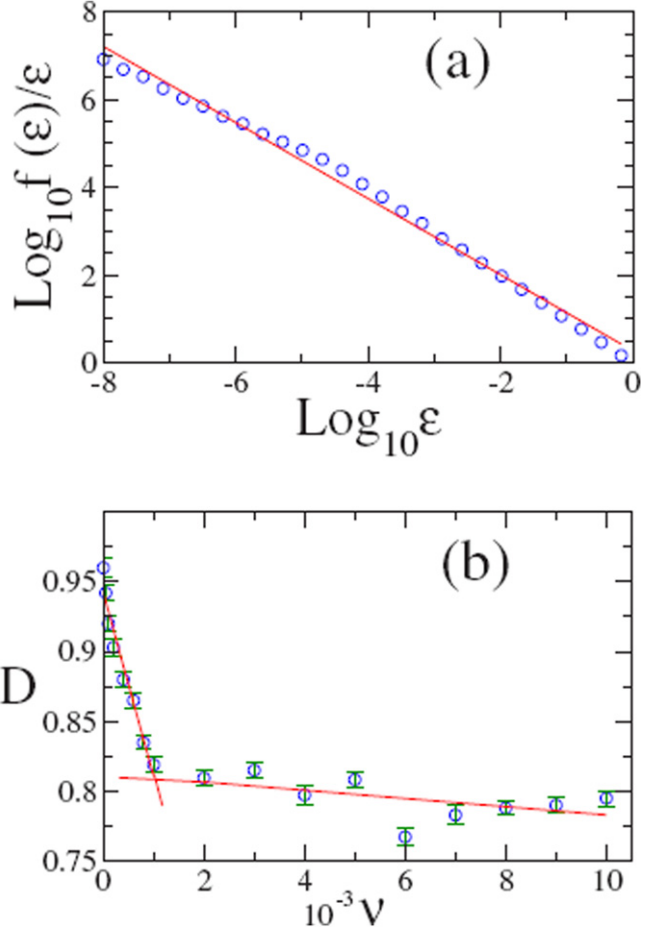


**Figure 63.** For the scattering map system equation (44) for  $\lambda = 4$ , (a) algebraic scaling of  $f(\varepsilon)/\varepsilon$  with  $\varepsilon$  for  $v = 6 \times 10^{-4}$ , which gives the dimension value  $D = 0.87 \pm 0.01$ . (b) Dependence of the dimension on the dissipation parameter  $v$ . A crossover phenomenon can be seen to occur near  $v = v_c \approx 10^{-3}$ . Reproduced with permission from [235]. Copyright 2007 American Physical Society.

measured which characterize the dependence of some physical variables after the scattering on some input variables (e.g. the impact parameter) before the scattering. These functions can be used to probe the intrinsic structure and dynamics of the underlying scattering system. When chaos is present, a scattering function typically contains an uncountably infinite number of singularities [5, 236], so the fractal dimension of the set of singularities is naturally of significant physical interest. For nonhyperbolic scattering, a previous study indicated that the ultimate value of the dimension is unity [202], due to the algebraic particle-decay law. When dissipation causes the decay law to become exponential, the fractal dimension will assume some value less than unity [208]. It is also of interest to investigate how the fractal dimension decreases as the dissipation parameter is increased from zero gradually [235].

The fractal dimension of the set of singularities in a scattering function can be most conveniently calculated by using the uncertainty algorithm [237, 238], which can be explained using the scattering map equation (44). First, one chooses a line segment, e.g., one defined by  $y_0 = -2$ , from which trajectories are launched toward the scattering region

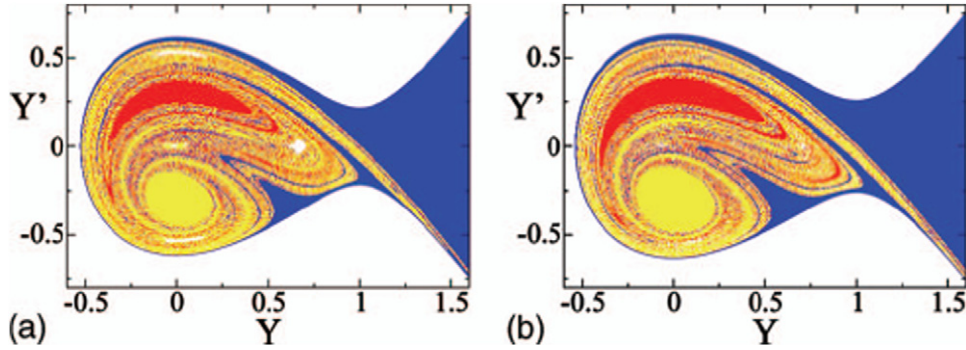


**Figure 64.** For  $E = 0.19$  in the Hénon–Heiles system, (a) the basins of scattering particles in the conservative case. In this case there are three destinations and the initial conditions going to the destinations are distinguished by three colors; the white regions inside the plotted structure denote the KAM islands. (b) The basin structure in the presence of a small amount of dissipation ( $\alpha = 10^{-4}$  and  $\beta = 10^{-4}$ ). Due to the dissipation, an additional destination arises: the fixed-point at the center of the scattering region. Four colors are then needed to distinguish the initial conditions. Reproduced with permission from [19]. Copyright 2006 American Institute of Physics.

centered about  $(x, y) = (0, 0)$ . Next, randomly choose an initial condition  $x_0$  on the line segment. A small perturbation  $\varepsilon$  leads to another nearby initial condition  $x_0 + \varepsilon$ . If the two trajectories from the pair of initial conditions escape from the system in the same number of iterations, or if both trajectories approach the same attractor, the pair of initial conditions are referred to as *certain* with respect to the perturbation  $\varepsilon$ . Otherwise they are *uncertain* with respect to  $\varepsilon$ . Among many randomly chosen initial-condition pairs, the fraction of uncertain initial conditions  $f(\varepsilon)$  scales algebraically with  $\varepsilon$  as  $f(\varepsilon) \sim \varepsilon^{1-D}$ , or  $f(\varepsilon)/\varepsilon \sim \varepsilon^{-D}$ , where  $D$  is the fractal dimension [237, 238] of the set of singularities in any scattering function defined on the line segment. Figure 63(a) shows, for  $\nu = 6 \times 10^{-4}$ , the algebraic scaling of  $f(\varepsilon)/\varepsilon$  with  $\varepsilon$ . The dimension value is  $D = 0.87 \pm 0.01$ . (In the actual computation of  $f(\varepsilon)$ , it is useful to increase the number of random initial conditions until the number of uncertain initial conditions reaches a prescribed value (say 500)). The variation of  $D$  as a function of the dissipation parameter  $\nu$  is shown in figure 63(b). It can be seen that the dimension decreases rapidly from unity as  $\nu$  is increased from zero. In addition, a crossover phenomenon occurs for  $\nu = \nu_c \approx 10^{-3}$ , after which the dimension decreases much more slowly for  $\nu > \nu_c$ . Similar behaviours have been observed in continuous-time cases, such as the Hénon–Heiles scattering system [235].

A heuristic theory for the crossover phenomenon in the fractal dimension was proposed in [235]. In particular, for scattering systems described by two-dimensional invertible maps or three-dimensional flows, the nonattracting invariant sets responsible for chaotic scattering are chaotic saddles [1, 5, 236], the stable and unstable manifolds of which are fractals [239]. Scattering particles are typically launched from a line segment straddling the stable manifold outside the scattering region; the set of singularities is nothing but the Cantor set of intersection of the stable manifold with the line segment. The starting point of the theory is the geometrical construction of the Cantor set used to argue that, in nonhyperbolic chaotic scattering, the fractal dimension of the set of singularities in the scattering function is  $D = 1$  [202].

Specifically, the construction begins with the unit interval  $[0, 1]$ . According to the procedure explained in section 5.3, we

obtain that the numerically determined value of the dimension increases toward 1.

Now consider a chaotic scattering system where particles are launched from a line segment straddling the stable manifold of the chaotic saddle. There is then an interval of input variables which lead to trajectories that remain in the scattering region for at least a duration of time, say  $T_0$ . By time  $2T_0$ , a fraction  $\eta$  of these particles leave. If the initial conditions of these escaping particles are all located in the middle of the original interval, there are then two equal-length subintervals of the input variable which lead to trajectories that remain for at least time  $2T_0$ . By time  $3T_0$ , an additional fraction  $\eta$  of the particles, whose initial conditions are located in the middles of the two subintervals remaining at time  $2T_0$ , escape. There are then four subintervals, particles initiated from which can remain in the scattering region for time at least  $3T_0$ , and so on. The resulting set is a Cantor set of Lebesgue measure zero on which particles never escape. The box-counting dimension of the Cantor set is given by

$$D = \frac{\ln 2}{\ln [(1 - \eta)/2]^{-1}}.$$

In the conservative case, if the scattering is nonhyperbolic, because of the algebraic decay:  $P(t) \sim t^{-z}$ , the fraction  $\eta$  is no longer a constant: it varies at each stage of the construction of the Cantor set. At the  $n$ th stage ( $n$  large), the fraction  $\eta_n$  is approximately given by  $\eta_n \approx -T_0 P^{-1} dP/dt \approx z/n$ , which yields a Cantor set with dimension 1, where the quantity  $a$  in the mathematical construction of the Cantor set corresponds to the algebraic-decay exponent  $z$ . For conservative hyperbolic chaotic scattering, particles escape exponentially from the scattering region:  $P(t) \sim e^{-\gamma t}$ , where the decay rate  $\gamma$  is related to the fraction  $\eta$  as  $\gamma = T_0^{-1} \ln(1 - \eta)^{-1}$ .

When there is a small amount of dissipation, the fraction  $\eta$  is no longer a constant of time [213]. Intuitively we can write

$$\eta_n = \frac{a}{n+b} - \delta, \quad (45)$$

where  $a$  and  $b$  are constants and  $\delta$  is the fraction remaining at each stage due to the dissipation-induced small attractors in the

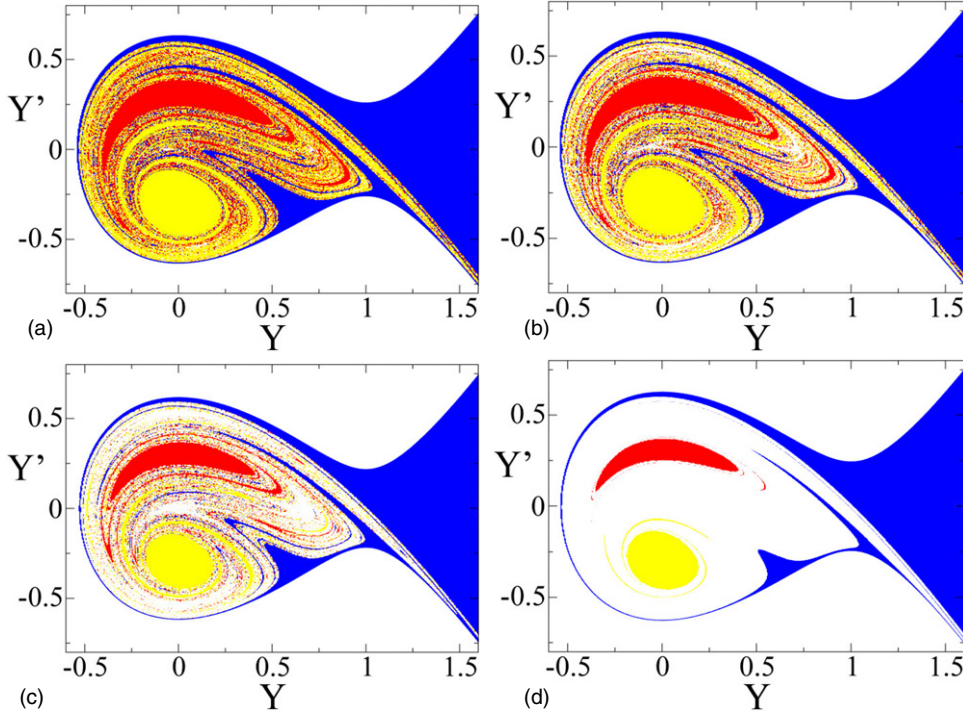


**Figure 65.** (a)–(d) Basins of scattering destinations and of the fixed-point attractor at the center of the scattering region for  $E = 0.19$  and for  $\mu = 5 \times 10^{-4}, 10^{-3}, 10^{-2}$  and  $10^{-1}$ , respectively. Reproduced with permission from [19]. Copyright 2006 American Institute of Physics.

scattering region. For weak dissipation we have  $0 < \delta \ll a/b$ . The fractal dimension is then

$$D = \ln 2 / \ln \left( \frac{2}{1 + \delta} \right). \quad (46)$$

As  $\delta \rightarrow 0$ , we have  $D \rightarrow 1$  but  $dD/d\delta = 1/\ln 2 \neq 0$ . As the dissipation parameter  $\nu$  is increased from zero,  $\delta$  also increases from zero, leading to a decrease in the fractal dimension from unity. If  $\nu$  is not too large (say  $\nu < \nu_c$ ), attractors are constantly created as  $\nu$  is increased from zero, i.e. as the system becomes more dissipative. A relatively large rate of increase in  $\delta$  can then be expected. As the system becomes sufficiently dissipative so that most of the possible attractors that the system may possess have already been created, the increase in  $\delta$  slows down as  $\nu$  is increased further (say for  $\nu > \nu_c$ ). This leads to a much slower decrease in the dimension. A crossover behaviour can then be expected when  $\nu$  passes through  $\nu_c$ . The actual value of  $\nu_c$  depends on the system details: it cannot be predicted analytically.

**8.1.3. Invariance of basin topology under weak dissipation.** We have seen that the particle-decay law and the fractal dimension associated with nonhyperbolic chaotic scattering can be drastically altered by weak dissipation. These characteristics are therefore structurally unstable under dissipation. However, a surprising phenomenon is that the complex basin topology defined with respect to distinct scattering destinations in chaotic scattering is structurally stable. This was observed in the Hénon–Heiles system [19].

The Hénon–Heiles system has a four-dimensional phase space which can be reduced to a three-dimensional phase space

due to the conservation of the Hamilton function. To calculate the basins, it is convenient to choose a two-dimensional plane and launch a large number of scattering particles from this plane. The locations of the initial particles can be distinguished by examining through which escaping channels they leave the scattering region. Figure 64(a) shows, in the absence of dissipation, distinct sets of initial conditions in the plane  $(y, \dot{y})$ , where the particle energy is set to be  $E = 0.19$  and the initial  $x$ -coordinate of the particles is  $x(0) = 0$ . To generate figure 64(a), a uniform grid of  $500 \times 500$  initial conditions was chosen in the region  $(-1 \leq y \leq 2, -1 \leq \dot{y} \leq 1)$ . In figure 64(a), the set of blue, red and yellow dots denote initial conditions resulting in trajectories that escape through channel 1, 2 and 3 and the white regions inside the plotted structure denote the KAM islands. A complex, fractal-like basin structure can be seen. In fact, it can be shown that the basins are not only fractals, but also Wada [240]. Figure 64(b) shows, for the same simulation setting but with weak dissipation ( $\alpha = 10^{-4}$  and  $\beta = 10^{-4}$ ), the exit basins.

Due to the appearance of the fixed-point attractor at the center of the scattering region, now four colors are needed to distinguish the initial conditions according to the four possible destinations: exits 1–3 and the attractor. In particular, the colors *blue*, *red* and *yellow*, denote initial conditions that escape through exits 1–3, respectively; white regions inside the structure plotted denote the basin of the fixed-point attractor.

Qualitatively, a similar mixture of basins is observed as in the conservative case, suggesting that the Wada property persists under weak dissipation. Figures 65(a)–(d) show, for  $E = 0.19$ , the basins for  $\mu = 5 \times 10^{-4}, 10^{-3}, 10^{-2}$  and  $10^{-1}$ , respectively. The Wada property can be inferred from

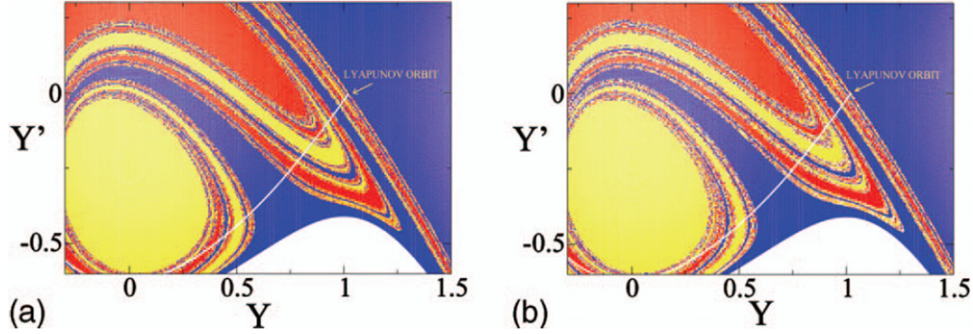


**Figure 66.** Hamiltonian case and Dissipative case. For  $E = 0.25$  in the Hénon–Heiles system, a segment of the unstable manifold of one of the three Lyapunov orbits, an unstable periodic orbit accessible to at least one basin. That the segment intersects all four basins suggests the Wada property of the basins, (a) in the Hamiltonian case, (b) in the dissipative case with  $\alpha = 10^{-4}$  and  $\beta = 10^{-4}$ . Reproduced with permission from [19]. Copyright 2006 American Institute of Physics.

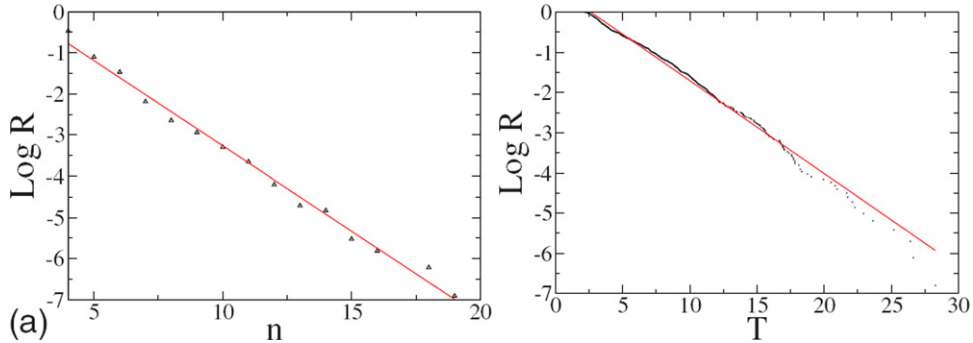


**Figure 67.** Examples of exponential decay law for model systems equations (47) and (48).  $R$  denotes the fraction of particles remaining in the scattering region. Reproduced with permission from [243]. Copyright 2009 American Physical Society.

figure 66, which shows,  $E = 0.25$ ,  $\alpha = 10^{-4}$  and  $\beta = 10^{-4}$ , a segment of the unstable manifold of a Lyapunov orbit. It can be seen that the unstable manifold intersects all four basins, so those basins must be Wada.

### 8.2. Effect of noise on chaotic scattering

Noise or random perturbations are inevitable in real-world systems for which the systems are not completely conservative [241]. It is of physical interest to explore what effects noise can have on chaotic scattering dynamics [242–244]. Since, in the presence of noise, the originally fine, fractal phase-space structure is smeared out up to a scale determined by the noise amplitude. The fractal dimension of the set of singularities in any scattering function is thus trivially one. Our discussion will thus focus on two aspects of chaotic scattering dynamics: particle decay and basin topology.

**8.2.1. Exponential particle-decay law under noise.** For hyperbolic chaotic scattering, because of the structural stability of the underlying chaotic invariant set, noise has little effect on the dynamical characteristics. For example, the particle-decay law is exponential, with or without noise. However, for nonhyperbolic chaotic scattering, noise of reasonably large amplitude can cause the originally algebraic particle decay to turn into exponential decay [243], which can be demonstrated by using, (1) in discrete time, the map model [202] but under

random perturbations [245],

$$\begin{aligned} x_{n+1} &= \lambda[x_n - (x_n + y_n)^2/4 - v(x_n + y_n)] + u\xi_n, \\ y_{n+1} &= \lambda^{-1}[y_n + (x_n + y_n)^2/4] + v\eta_n, \end{aligned} \quad (47)$$

where  $u$  and  $v$  denote the noise strength,  $\xi_n$  and  $\eta_n$  are independent random processes, or (2) in continuous-time, the random Hénon–Heiles system,

$$\begin{aligned} \ddot{x} + x + 2xy + \mu\dot{x} &= \sqrt{2\varepsilon}\xi(t), \\ \ddot{y} + y + x^2 - y^2 + \mu\dot{y} &= \sqrt{2\varepsilon}\eta(t), \end{aligned} \quad (48)$$

where  $\mu$  is a parameter characterizing weak dissipation,  $\varepsilon$  is the intensity of the noise and  $\xi(t)$  and  $\eta(t)$  are random processes. The stochastic differential equation equation (48) can be conveniently solved using the standard second-order routine [246]. Exponential decays in both equations (47) and (48) are exemplified in figure 67.

That noise leads to exponential particle decay in chaotic scattering can be heuristically argued, as follows. In general, such a decay law results from a nonattracting, Cantor-like fractal set in the phase space. Say we randomly and uniformly distribute a large number  $N$  of particles in the scattering region. In the absence of noise, after a unit time interval  $T_0$ ,  $\eta$  fraction of particles will have escaped. If noise is added at this time, and if the noise is intense enough to effectively redistribute the remaining particles randomly in the initial region, the particle distribution becomes the same as the initial random

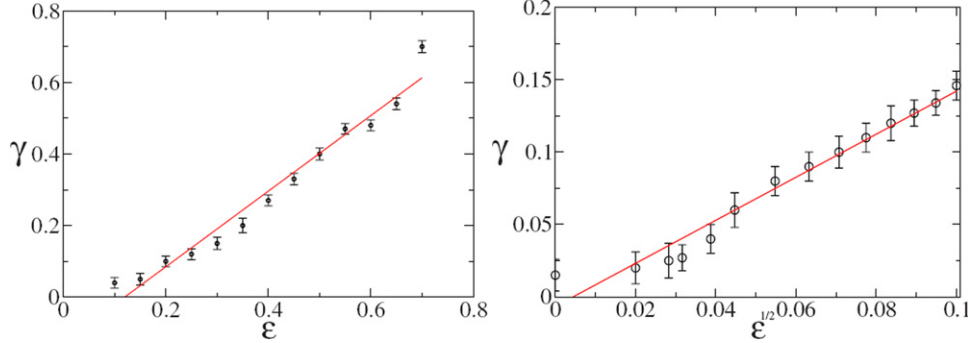


**Figure 68.** For the model systems equations (47) and (48), scaling law of the exponential decay law with the noise intensity. Reproduced with permission from [243]. Copyright 2009 American Physical Society.

distribution, with a total number of particles  $N(1 - \eta)$ . After another time  $T_0$ , the fraction of particles escaped will be the same as the previous one, which is  $\eta$ . This illustrates that the effect of noise is to redistribute particles as randomly (uniformly) as possible at different time steps. As a result, the fraction  $\eta$  of escaped particles during identical time intervals is approximately constant. This enables us to write down the evolution equation of the fraction of remaining particles  $R$  as  $dR/dt = -\eta R$ . With initial condition  $R(0) = 1$ , the solution is  $R = e^{-\eta T}$ , which is an exponential decay.

**8.2.2. Enhancement of decay rate by noise.** A previous work revealed that, when noise is present in a scattering system, particles tend to escape faster from the scattering region as compared with the noiseless case [242]. An issue is thus how the exponential decay rate scales with the noise intensity. We note that in noisy chaotic systems, different forms of scaling laws are always of interest. For instance, in an earlier work [247], it was shown that when noise is present in a dissipative chaotic system, the volume of the attractor,  $A_\varepsilon$ , scales with the noise amplitude  $\varepsilon$  as  $\varepsilon^{D-d}$ , where  $D$  is the phase-space dimension and  $d$  is the dimension of the attractor. This result was also generalized to the three-disk chaotic scattering system [248] through the scaling of the volume of the stable manifold with the noise amplitude.

Here we shall discuss the noisy scaling law of the exponential decay rate uncovered in [243] for chaotic scattering:

$$\gamma \sim \varepsilon^\kappa, \quad (49)$$

where  $\kappa > 0$  is the scaling exponent. Numerical evidence for the scaling law is shown in figure 68. To provide a theoretical understanding of the scaling law (49), we start from a purely Hamiltonian chaotic scattering system, where the decay law is algebraic in the absence of noise. If the noise intensity is sufficiently small, most KAM tori persist. In this case, the decay law is still algebraic. When the noise intensity exceeds a critical value so that KAM tori are smeared out, the decay law becomes exponential. Depending on the structures of the KAM tori of the specific dynamical system, the transition from algebraic to exponential decay may or may not be abrupt. For example, if KAM tori have a fine structure of typical scale  $l$ , then there exists a critical noise intensity  $\varepsilon_c \sim l$ , where if  $\varepsilon < \varepsilon_c$ , KAM tori can be preserved at least for a very long

time, making algebraic the scaling law. If  $\varepsilon > \varepsilon_c$ , KAM tori are destroyed so that the particles are redistributed and the scaling law becomes exponential. However, for most cases, KAM tori may not have a typical scale (self-similar structure), thus for a given noise intensity, some particles are redistributed effectively and escape in an exponential manner, while others can still be confined for a long time. For this case, since the extremely long time confinement is mainly caused by the fine structures of KAM tori, a small amount of noise will first destroy this confinement. As a result, the transition from algebraic decay to exponential decay is expected to be smooth in this case.

To be concrete, we analyze the continuous-time scattering model equation (48). Let  $v = \dot{x}$  be the velocity, the first equation can be rewritten as

$$\dot{v} + \mu v - F = \sqrt{2\varepsilon}\xi, \quad (50)$$

where  $F = -x - 2xy$  is the corresponding force from the Hénon–Heiles potential. Now assume  $F = 0$ . Equation (50) then becomes a linear stochastic equation describing damped Brownian motion. Regarding  $v$  as the output and  $\sqrt{2\varepsilon}\xi$  as the input, the transfer function is

$$H(s) = \frac{1}{(s + \mu)}, \quad (51)$$

and the power spectral density (PSD) is given by

$$S_v(f) = |H(2\pi i f)|^2 S_{\sqrt{2\varepsilon}\xi}. \quad (52)$$

Since  $\xi$  is the unit of white Gaussian noise, we have  $S_{\sqrt{2\varepsilon}\xi} = 2\varepsilon$ . Therefore, the variance of the output  $v$  is

$$\langle v^2 \rangle_T = \int_{-\infty}^{\infty} S_v df = \int_{-\infty}^{\infty} |H(2\pi i f)|^2 [S_{\sqrt{2\varepsilon}\xi}] df = \frac{\varepsilon}{\mu} \sim \varepsilon. \quad (53)$$

Thus, the energy fluctuation is proportional to  $\varepsilon$ . However, for nonzero force  $F$ , as in our case, the velocity  $v$  and the energy  $E$  have nonzero mean values and  $E \sim v^2$ . Thus  $\delta E \sim v \delta v$ . Note that the force due to the noise is proportional to  $\sqrt{\varepsilon}$ . As a result, for a small time interval  $\Delta t$ , the velocity fluctuation is of the order of  $\sqrt{\varepsilon} \Delta t$ . Since the velocity variation due to the force is much smaller, in a short time interval the velocity is approximately constant. We thus have

$$\delta E \sim v \sqrt{\varepsilon} \Delta t \sim \sqrt{\varepsilon}.$$

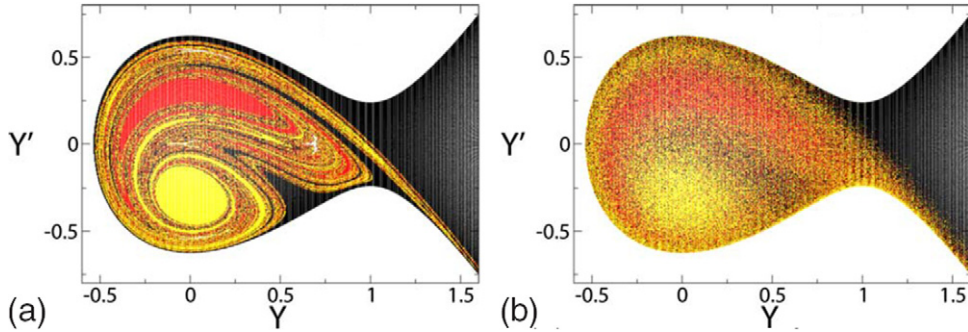


**Figure 69.** For the noisy Hénon–Heiles system equation (48) for  $E = 0.195$ , (a) three coexisting exit basins in the conservative limit in the absence of noise, where the colors denote the sets of initial conditions generating trajectories that exit through three distinct escaping channels and (b) the corresponding plot when noise intensity  $\varepsilon = 2 \times 10^{-3}$  is present. Reproduced with permission from [243]. Copyright 2009 American Physical Society.

Defining  $T_0 = 1/\gamma$ , we have  $R(t) \sim e^{-T/T_0}$ . The average lifetime of the particles is  $\langle T \rangle = \int T \cdot R(T) dT = T_0$ , which depends on the initial energy  $E$ . In general, we can write  $T_0 = g(E)$ , or  $\gamma = f(E)$ . Under energy fluctuation  $\delta E$ , we have  $\gamma \approx f(E) + f'(E)\delta E$ . Since particles escape more quickly if they have higher energies, we see that  $f'(E)$  is positive. Due to the energy scaling  $\delta E \sim \sqrt{\varepsilon}$ , we see that for fixed  $E$ ,  $\gamma$  depends linearly on  $\sqrt{\varepsilon}$ , thereby the scaling law (49). A similar argument can be made for maps. For example, in equation (47), the noise terms  $u_n$  and  $v_n$  are proportional to  $x_{n+1}$  and  $y_{n+1}$ , which leads to a linear relation between  $\gamma$  and  $\varepsilon$ .

**8.2.3. Effect of noise on scattering basin topology.** Intuitively, noise smears various scattering basins in the phase space. Figure 69 shows an example from the system equation (48), where the fine-scale, Wada characteristics of the scattering basins are destroyed by noise [242].

On the other hand, the study of noise and dissipation in the randomly driven Hénon–Heiles system has been carried out by Gan *et al* [249]. In this work the authors investigate this system with a random driven force when the energy is above  $E_e$ . The main finding of this work is that the fractal exit basins appear robust when the bounded noisy excitation is imposed on the system. Finally, recent studies on the effects of weak noise [250, 251] in the context of Hamiltonian scattering have shown that small noise can enhance the particles to be trapped in the scattering region for a long time. Reference [250] shows a universal quadratic power law relating the exponential decay to the amplitude of noise. The study of chaotic scattering, taking into account other physical effects as the Lorentz–Einstein relativistic transformation and their consequence on the basin boundaries, can be found in [252]. Other studies related to the basin boundaries in problems with escapes can be found in [253, 254].

## 9. Additional topics on chaotic scattering

### 9.1. Time-dependent Hamiltonian systems

Our discussions of chaotic scattering so far have been limited to time-independent systems. The phenomenon can occur, of course, in time-dependent systems as well. When the

Hamiltonian contains an explicit time dependence, even if the system has only one degree of freedom, the corresponding phase-space dimension will be three (or as commonly said 2+1 dimensions), the minimum dimension required for chaos to occur [3]. To demonstrate chaotic scattering in time-dependent situations, it is thus insightful to consider one-degree-of-freedom Hamiltonian systems of the following form:

$$H(x, p, t) = p^2/2m + V(x, t), \quad (54)$$

where  $x$  and  $p$  denote the position and the momentum of scattering particles, respectively, and  $V(x, t)$  is a time-dependent potential function [255–257]. To be concrete, here we discuss a class of time-dependent potential barriers whose heights are finite and constant but their positions change with time [257]:  $V(x, t) = V(x - f(t))$ , where  $f(t)$  is an oscillating function with fixed frequency but time-varying amplitude  $a(t)$ . Situations describable by this type of time-dependent potential include electron motions in the potential field of atoms, as in a crystal. To be more specific, we discuss a prototype model consisting of two collinear symmetrical potential barriers separated by a minimum distance  $2d$ , as shown in figure 70(a). The positions of the barriers oscillate periodically in time but out of phase with respect to each other by phase difference  $\pi$ , which can be described as  $\pm f(t)$ , as shown in figure 70(b). Let  $V_h$  be the barrier height and  $E_p$  be the initial energy of the particle in the potential well, defined by the region in between the potential barriers. Since the potential barriers are moving periodically in time, a particle, when interacting with the potentials, can either gain or lose energy, depending on the relative directions of its velocity and the instantaneous force exerting on it by the potential. As a result, a particle with initial energy  $E_p < V_h$  may escape and a particle with initial energy  $E_p > V_h$  may stay in the potential well for a long time. Due to the mirror-reflection symmetry, the system is equivalent to a hard wall at  $x = 0$  and an oscillating potential barrier at the distance  $d + f(t)$  away, as shown in figure 70(c). To facilitate analysis and computation, the potential barrier can be assumed to be a rectangle with height  $V_h$  and width  $W$ , as shown in figure 70(d). The system bears a certain similarity to the Fermi acceleration problem [258]. It was demonstrated that this time-dependent system can exhibit both nonhyperbolic and hyperbolic chaotic scattering [257].

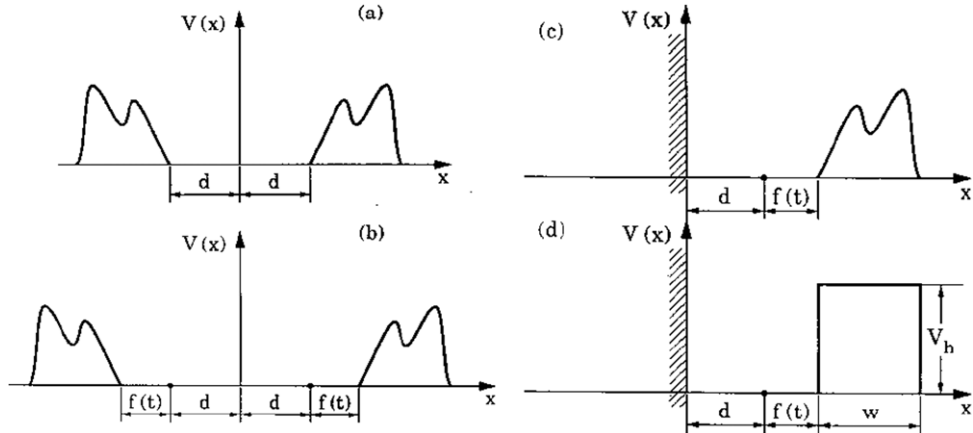


**Figure 70.** (a) A system of two oscillating potential barriers having a reflecting symmetry with respect to  $x = 0$ , (b) potential barriers displaced by  $f(t)$ , (c) equivalent system, (d) rectangular oscillating potential barrier. Reproduced with permission from [257]. Copyright 1991 World Scientific.

### 9.2. Bifurcations to chaotic scattering

A basic question that was investigated during the early stages of studying chaotic scattering is how it arises as the system parameter changes. Earlier studies suggested two main routes: abrupt bifurcation [5, 259] and saddle-center with a period-doubling like transition [260]. One type of abrupt bifurcation [5] can be conveniently illustrated by considering a system possessing four symmetric potential hills in the plane, e.g.,  $V(x, y) = x^2 y^2 \exp[-(x^2 + y^2)]$  for which the four hills are located at  $(x, y) = (\pm 1, \pm 1)$ , respectively and the local maximum value of each hill is  $E_m = e^{-1}$ . Now consider a particle interacting with the potential. If the particle energy  $E$  is greater than  $E_m$ , no bounded orbits can be formed in the scattering region. As  $E$  is decreased through  $E_m$ , suddenly an infinite number of unstable bounded orbits, periodic or aperiodic, appear. In fact, these unstable orbits constitute a nonattracting invariant set that gives rise to hyperbolic chaotic scattering [5]. For  $E$  slightly below  $E_m$ , the fractal dimension of the set of singularities in any scattering function obeys the following scaling law [5]:  $d \sim 1/\ln[(E_m - E)^{-1}]$ , where  $d$  approaches zero as  $(E_m - E) \rightarrow 0$ , so that the behaviour of  $d$  at  $E_m$  is not smooth but still continuous (note that  $d = 0$  for  $E > E_m$ ). In another type of abrupt bifurcation to chaotic scattering, the fractal dimension is discontinuous at the bifurcation point [259]. This is caused by the existence of a closed, classically forbidden region with well developed Hamiltonian chaos. For a scattering particle incident from outside, if its energy is below a critical value  $E_c$ , the forbidden region is inaccessible. As its energy is increased through  $E_c$ , the forbidden region, and hence the associated Hamiltonian chaos, suddenly becomes accessible, giving rise to chaotic scattering.

The saddle-center bifurcation route to chaotic scattering [260] is analogous to the typical period-doubling route to chaotic attractor in dissipative dynamical systems, which initiated from a saddle-node bifurcation. In the Hamiltonian counterpart, a saddle-center bifurcation first occurs, with KAM tori surrounding the center. As a parameter changes, the center undergoes a cascade of period-doubling bifurcations, leading

eventually to a nonattracting chaotic invariant set. Since, when this chaotic set appears, there are still KAM tori in the phase space, this route typically gives rise to nonhyperbolic chaotic scattering that can become hyperbolic, or fully developed, chaotic scattering as the bifurcation parameter changes further. A thorough investigation of this route can be found in Ref. [260] where the authors used a three potential-hill scattering system to explore the relevant issues such as dimension scattering and particle-decay law.

Bifurcation to chaotic scattering can also be explored from a physically more relevant approach. In a scattering experiment, it is often difficult to assess the behaviour of any individual particle and, instead, one typically launches a beam of particles toward the scattering region; the flux of particles coming out of the system is measured as a function of the impact parameter, which gives essentially the differential cross section function. In a recent work [261], the authors studied how a transition from regular to chaotic scattering is manifested in the differential cross section function. It has been found that the birth of new unstable orbits during the transition leads to a cascade of singularities in this function, which correspond to directions along which the particle flux diverges, henceforth the term *rainbow singularities* [262, 263]. In fact, the transition is accompanied by an infinitely fine sequence of occurrences of rainbow singularities in the cross section function. Further, the intervals in the bifurcation parameter separating successive births of rainbow singularities preceding the appearance of a new periodic orbit in the chaotic set decrease according to a power law [262].

Because of the physical importance of differential cross section in scattering dynamics, here we give a more detailed account of its behaviour associated with bifurcation to chaotic scattering. Following [261], we consider particle motion in a two-dimensional potential field consisting of the superposition of two attractive circularly symmetric potential wells,  $V(r)$ , as shown in figure 71(a). For a scattering function  $\Phi(b)$ , where  $\Phi$  is the scattering angle and  $b$  is the impact parameter, the differential cross section is given by

$$\frac{d\sigma}{d\Omega} = \sum_i \frac{b_i}{\sin \theta} \left| \frac{d\Phi(b_i)}{db} \right|^{-1}, \quad (55)$$

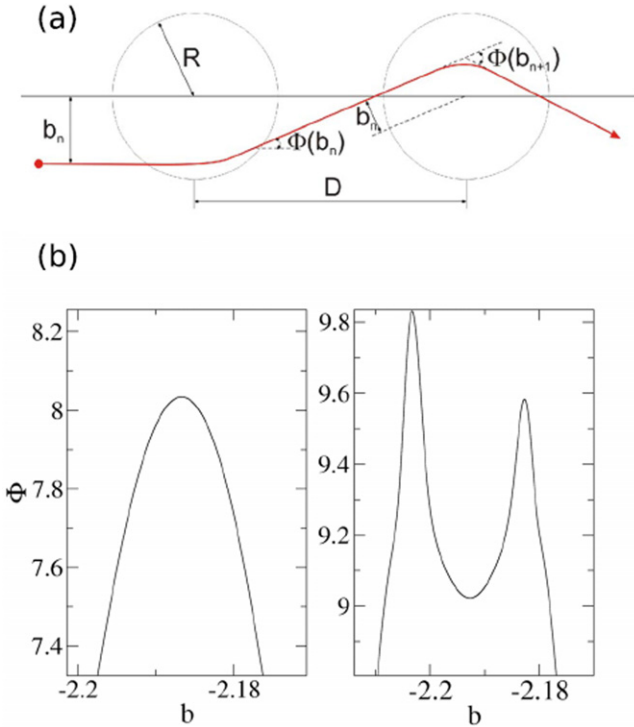


**Figure 71.** Illustration of (a) of two-dimensional scattering model and (b) creation of rainbow singularities. Reproduced with permission from [261]. Copyright 2008 American Physical Society.

where, as shown in figure 71(a),  $0 < \theta < 2\pi$  and the sum is extended over all impact parameters  $b_i$  satisfying the relation  $\Phi(b_i) + 2n\pi = \Theta$ , with  $n$ 's being an integer. For a circular potential function  $V(r)$ , the relation between  $\Phi$  and  $b_i$  can be expressed as [256, 264]

$$\begin{aligned} b_{n+1} &= b_n - D \sin(\Phi_{n+1}) \operatorname{sgn}[\cos(\Phi_{n+1})], \\ \Phi_{n+1} &= \Phi_n - \phi(b_n) \end{aligned} \quad (56)$$

where  $D$  the distance between the centers of the two hills. The particular form of the scattering angle function  $\phi(b)$  depends on the detailed shape of the potential  $V(r)$  and on the energy of the particle as well. Following [262], we have

$$\phi(b) = \phi_{\max} \exp[-2(b+1)^2] - \phi_{\max} \exp[-2(b-1)^2], \quad (57)$$

where the parameter  $\phi_{\max}$  depends on the energy of the particle; it is the bifurcation parameter of the model. When  $\phi_{\max}$  is small, particles move through the potential region with little deflection, leading to regular scattering dynamics. As the energy is lowered, particle trajectories are deflected, leading to the creation of more and more unstable periodic orbits and eventually to chaos. This route is reflected in the differential cross section function, as shown in figure 72.

The creation of rainbow singularities follows a scaling law [262]. To derive the scaling law, one first obtains the following expression relating the locations of the singularities:

$$b_{n+1} \approx b_1 + CDn^2\epsilon, \quad (58)$$

where  $\epsilon \equiv \phi_c - \phi_{\max}$  and the constant  $C$  depend on the geometry of the particular orbit. One then obtains  $\Delta\epsilon$ , the

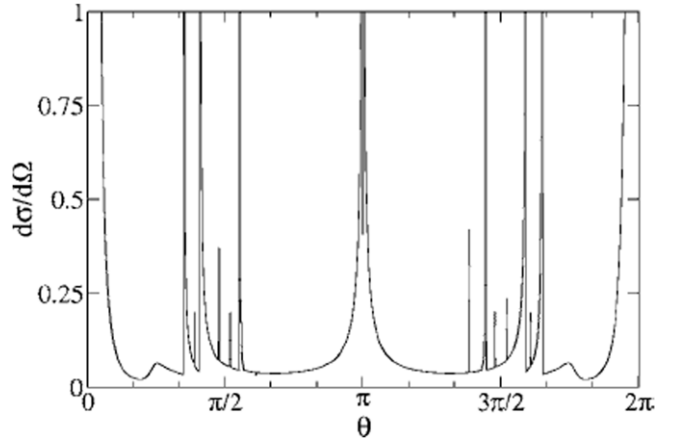


**Figure 72.** Typical scenario of the formation of an infinite number of rainbow singularities in the differential cross section. Reproduced with permission from [261]. Copyright 2008 American Physical Society.

parameter interval separating two successive appearances of rainbow singularities:

$$\Delta\epsilon = \frac{2\sqrt{D}}{K} \epsilon^{3/2}, \quad (59)$$

where, according to [262], the exponent 3/2 is universal.

### 9.3. Types of boundaries in chaotic scattering

There were previous studies concerning the structure of basin boundaries for particular systems and particular definitions of escapes [265]. The question of how the structure of the invariant set and the choice of the escapes (e.g. the surfaces in the configuration space through which scattering particles are considered to have exited the system) determine the geometry of the basin boundary was addressed in [266]. Two types of boundaries were found. Let  $B$  be the interaction of the boundary with a one-dimensional manifold in the phase space. For type I boundaries,  $B$  is a Cantor set consisting of points on the stable manifold of the invariant set; each point in  $B$  is the accumulation of other points in the set; there are no isolated points. In this case, the boundary is nonsmooth everywhere, and every magnification of neighborhoods of any boundary point reveals further structure. For type II boundaries,  $B$  consists of two components,  $B_c$  and  $B_s$ , where  $B_c$  is a Cantor set corresponding to the intersection of the one-dimensional curve used in the definition of  $B$  with the stable manifold of the invariant set, and  $B_s$  is a countable set of isolated points with a limit set on  $B_c$ .

In [266], it was shown that for a given Hamiltonian system, the occurrence of one or the other type of boundaries depends on whether there are forbidden regions in the configuration space. If there is no forbidden region for a given energy, the boundary will always be of type II, for any possibility of escape. A necessary condition for the occurrence of type I boundaries is the presence of some forbidden regions. Since the occurrence of forbidden regions depends on the energy, it is reasonable to speculate that, as the energy is varied, there can be a topological bifurcation in which the scattering boundaries

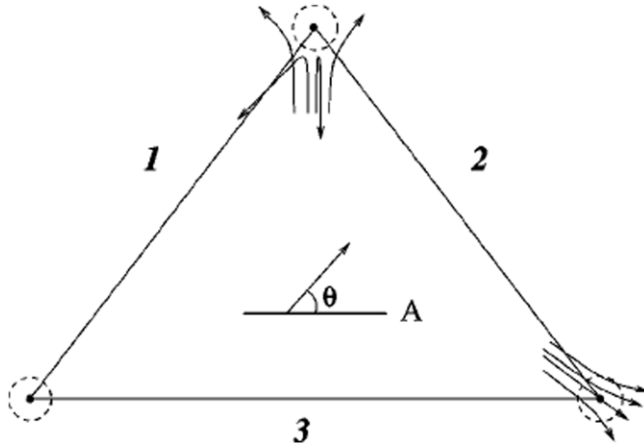


**Figure 73.** Schematic representation of the potential function in equation (60). The three hills are centered on the vertices of a triangle. The sides 1, 2 and 3 define three escapes. In the numerical simulations, the initial conditions were chosen from the segment  $A$  defined by  $y = 2$  with initial velocity in the direction  $\theta$ . Reproduced with permission from [266]. Copyright 2002 American Physical Society.

change from type I to type II. This was indeed observed [266] in a system where the potential function is the superposition of three identical potential hills, as shown in figure 73. In particular, the two-dimensional potential can be written as

$$V(x, y) = \sum_{i=0}^3 V_0(x - x_i, y - y_i), \quad (60)$$

where each hill  $V_0$  possesses a spherical symmetry and has a repulsive core surrounded by an attractive region. For example, the following form of  $V_0$  satisfies these requirements:

$$V_0(x, y) = A_+ \exp -r^2/2\sigma_+^2 - A_- \exp -r^2/2\sigma_-^2, \quad (61)$$

where  $A_+$ ,  $A_-$ ,  $\sigma_+$  and  $\sigma_-$  are positive constants, and  $r^2 = x^2 + y^2$ . For  $A_+ = 2.1$ ,  $A_- = 2$ ,  $\sigma_+ = 0.25$  and  $\sigma_- = 0.5$ ,  $V_0$  has a narrow central peak with a maximum of  $E_m = 0.1$  at the origin, surrounded by an attractive well. For particles with energy  $E \simeq 0.1$ , there is a forbidden region around the origin, into which the particle cannot penetrate. For  $E > E_c = 0.1$ , there is no forbidden region and chaos occurs [266]. Examples of exit basins are shown in figures 74(a) and (b) for energy  $E = 0.15 > E_c$  and  $E = 0.05 < E_c$ , respectively. The basin boundaries are apparently quite distinct for the two cases; there is a bifurcation in the basin topology from type I to type II that occurs as  $E$  is increased through  $E_c$ .

We remark that in most previous works on scattering basins, the boundaries were type I. However, type II boundaries were found in incompressible two-dimensional flows [267], in map models [268] and in chaotic scattering in three-dimensional physical space [269]. Moreover, type II boundaries cannot have the Wada property because they have smooth components, implying the existence of some sort of classically forbidden region in the configuration space as a necessary condition for Wada basins.

#### 9.4. Characterization of chaotic scattering by symbolic dynamics

Symbolic dynamics can often provide quite useful insights into the underlying chaotic system, which can be defined only when a suitable phase-space partition (or generalized partition) can be identified. In such a case, every trajectory can be associated with a symbolic sequence corresponding to the sequence of the partition cells visited by this trajectory. To demonstrate the use of symbolic dynamics in characterizing and understanding chaotic scattering dynamics, reference [270], considered systems described by two-dimensional maps, where the chaotic set is generated by some mechanism [271, 272] similar to Smale's horseshoe [273].

In [270], a method to partition the phase space for chaotic scattering dynamics was proposed, based on some kind of horseshoe construction in the two-dimensional Poincaré map. To avoid unnecessary complication, only the outer unstable part of the horseshoe was taken into account [274]; KAM islands were ignored. As a result, near the fractal surface of a KAM island and its surrounding secondary structures, the partition is only approximate. A requirement in defining a suitable partition is that scattering trajectories from the same interval of continuity are described by the same symbol sequence. Once a partition is defined, one can find a wealth of information about the scattering dynamics such as the number of times a trajectory enters the fundamental area  $R$  of the Poincaré map, the sequence of partition cells that the trajectory move through inside  $R$  (figure 75) and whether the trajectory reflects or transmits, etc.

To illustrate the use of symbolic dynamics, we discuss a prototypical scattering system consisting of a one-dimensional inverted Gaussian potential driven by a laser field  $E(t) = E_0 \sin(\omega t)$ , which has been used in previous studies of laser-atom interactions [275]. The Hamiltonian in the Kramers-Henneberger reference frame [276] is

$$H(x, t) = \frac{p^2}{2} - V_0 \exp(-([x + \alpha(t)]/\delta)^2), \quad (62)$$

where  $\alpha(t) = \alpha_0 \sin(\omega t)$  is the classical displacement of a free electron from its center of oscillation in the time-periodic electric field  $E(t)$  with  $\alpha_0 = -qE_0/\omega^2$ . Equation (62) can then be written as

$$H(x, t) = \frac{p^2}{2} - V_0 \exp(-([x + \alpha_0 \sin(\phi)]/\delta)^2) + I\omega, \quad (63)$$

where  $I$  and  $\phi$  are the action and angle variables of the driving field, respectively. This model can also lead to insights into the phase-space transport process in the system of hydrogen atoms under parallel electric and magnetic fields of a short laser pulse [277, 278].

A chaotic invariant set underlying scattering dynamics can usually be represented by a horseshoe construction on an appropriate Poincaré surface of section. The classical Smale horseshoe construction is accomplished by stretching a fundamental region  $R$  and folding it back onto the original region. The boundaries of  $R$  are given by segments of the invariant manifolds of the outer fixed points of the system.

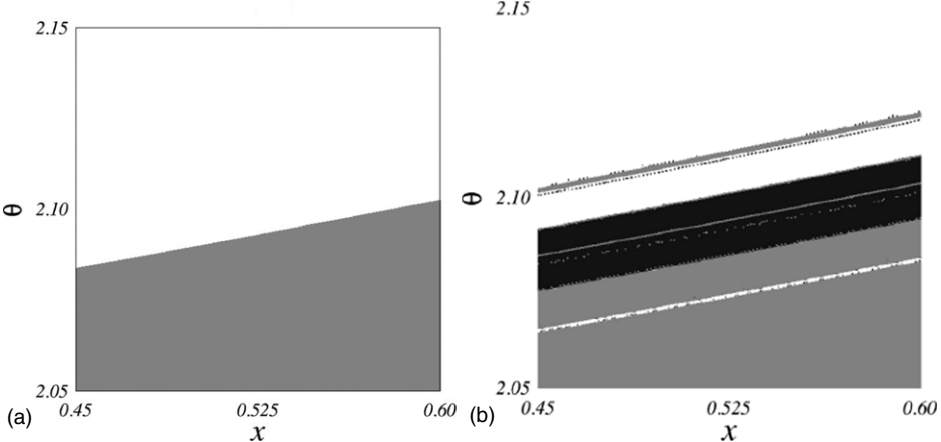


**Figure 74.** For the scattering system described by the potential function equation (60), exit basins for (a)  $E = 0.15 > E_m$  and (b)  $E = 0.05 < E_m$ . The region shown in (a) has a smooth boundary, there is a fractal structure in (b). Reproduced with permission from [266]. Copyright 2002 American Physical Society.

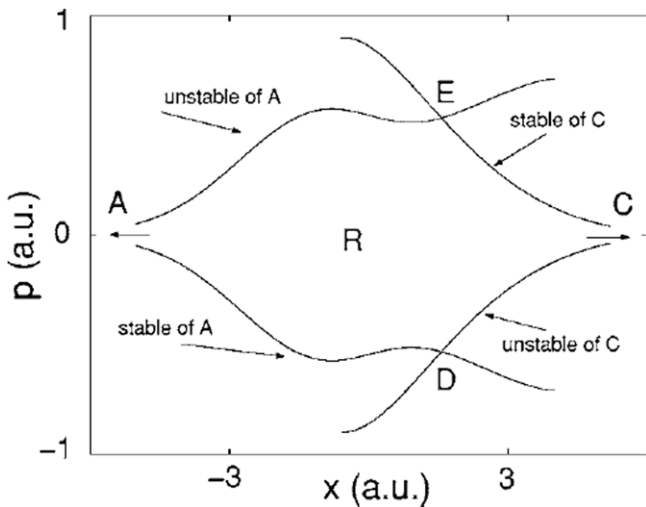


**Figure 75.** For the system described by equation (62), region  $R$  formed by the unstable manifold of the fixed point  $A$ , segment  $AE$ , the stable manifold of the fixed point  $C$ , segment  $CE$ , the unstable manifold of the fixed point  $C$ , segment  $CD$  and the stable manifold of the fixed point  $A$ , segment  $AD$ . Reproduced with permission from [270]. Copyright 2006 American Physical Society.

The system equation (62) has three *period* – 1 orbits. The inner fixed point is elliptic and the two outer ones are located at  $x \rightarrow \pm\infty$ , where the stable and unstable manifolds of the outer fixed point C (figure 75) converge to the same manifold; the same is true for the manifolds of the fixed point A at  $x \rightarrow \infty$ . As a consequence, the region  $R$  for the partition of the phase space can then be obtained. In a similar way, a structure for the scattered electrons from the left can be constructed (see figure 76). Such a construction can also be useful in different situations, e.g., lobes in fluid-transport problems [279]. The intersection points between the stable and unstable manifolds of the outer fixed points, as shown in figure 76, are called homoclinic or heteroclinic points, depending on whether the stable and unstable manifolds are associated with the same or different fixed points.

Once a proper partition is defined, we can extract the number of times a scattering trajectory entering the

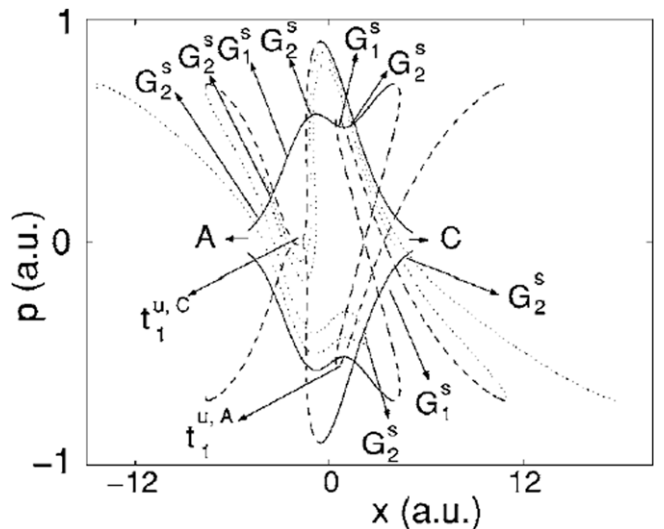


**Figure 76.** For the system described by equation (62), horseshoe construction up to level two on the Poincaré surface of section  $\Phi = \pi/2$ . Reproduced with permission from [270]. Copyright 2006 American Physical Society.

fundamental region and the sequence of partition cells it has visited in the area  $R$ . As shown in figure 77, consider particles incident from the left and a line of initial conditions that intersects one complete outer tendril, formed by the stable manifold of the fixed point C. The image of the line at each forward time step stretches and continues to intersect the stable manifold. Before entering the area  $R$ , the image of this line approaches the area  $R$  along the direction of the unstable manifold of the fixed point A; it is denoted by line  $E$  in figure 77. The line of initial conditions so chosen is thus a higher order pre-image of the line  $E$ . The part of the branching tree enclosed by a square in figure 78 describes the hierarchical structure of the intersections of the stable manifolds with the line of initial conditions  $E$ . Since all the scattering trajectories with initial conditions in the same interval of continuity of the scattering function have the same symbolic behaviour, information about the scattering dynamics can be obtained from the symbolic dynamics for each continuity interval.

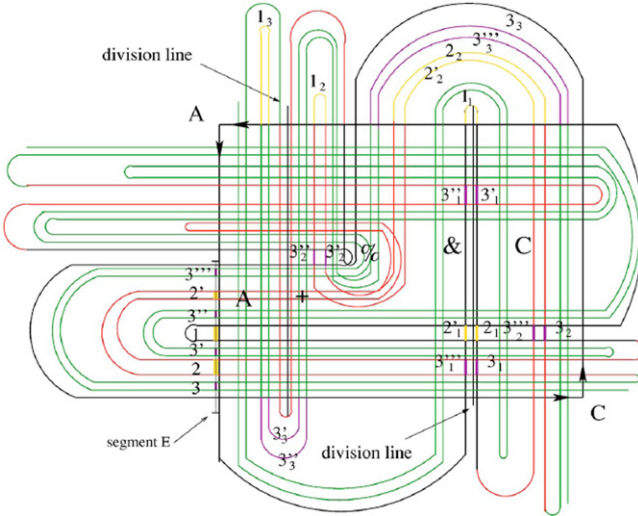


**Figure 77.** For the system described by equation (62), schematic illustration of the development scenario of chaotic scattering. Reproduced with permission from [270]. Copyright 2006 American Physical Society.

On the other hand, symbolic dynamics has been used to explain different problems related to ‘chaotic escapes’. In this sense, the works of K A Mitchell *et al* have been quite relevant in this field [280, 281]. In those papers the authors developed a new form of symbolic dynamics that establishes the existence and structure of a minimal required set of escape segments. This symbolic dynamics, which they then call homotopic lobe dynamics, has been also used to interpret the fractal structure of the escape-time plot of different physical problems. Some of the applications of this new method have been carried out in the study of the escape of trajectories from a vase-shaped cavity [282], chaotic scattering in hydrodynamics [283] and chaotic scattering in atomic physics [284], among others. Besides, homotopic lobe dynamics belongs to a larger field of research that applies symbolic techniques to the study of chaotic transport, including escape and scattering processes. The main mathematical works on that topic can be found in [274, 285–293]. Other additional topics related to chaotic scattering have been considered in recent years but they are beyond the scope of this review. Some of them concern understanding the properties of the dynamics in the interaction region and the integrability of the *S-matrix* versus integrability of the Hamiltonian [294]; others deal with the hyperbolic approximation to potentials with a mixed phase space. These have lead to a successful reconstruction of the hyperbolic component of the invariant manifold; many applications have been derived from it [110].

### 9.5. Chaotic scattering in higher dimensions

The topic of chaotic scattering has been basically dealt with in this review for two-dimensional problems. Here, we describe some of the important recent results that have been carried out in three dimensions. Some of the attempts to address chaotic scattering in higher dimensional systems have been shown in [269, 295–300].

**9.5.1. Chaotic saddles in high dimensions.** Due to the high dimensionality of the phase space, an issue of concern is whether chaotic scattering can be observed even if there is a chaotic saddle of low dimension in the scattering region. In particular, suppose in a scattering experiment one measures a scattering function for particles launched from a one-dimensional line segment. If the dimension of the chaotic saddle is not sufficiently high, its stable manifold may not have generic intersections with the line. These intersections can be observed only when the dimension of the chaotic saddle is sufficiently high.

To address this observability issue, some mathematical statement concerning the dimension of the intersection between two sets is added [1]. For that purpose, let  $S_1$  and  $S_2$  be two subsets of an  $N$ -dimensional manifold with dimensions  $D(S_1)$  and  $D(S_2)$ , respectively. The question is whether the sets  $S_1$  and  $S_2$  intersect generally in the sense that the intersection cannot be removed by small perturbations. The natural approach is to look at the dimension  $D_I$ :

$$D_I = D(S_1) + D(S_2) - N. \quad (64)$$

If  $D \geq 0$ , the intersection is generic and the dimension of the set of intersections is [301]

$$D(S_1 \cap S_2) = D_I = D(S_1) + D(S_2) - N. \quad (65)$$

If  $D_I$  is negative, then  $S_1$  and  $S_2$  do not have a generic intersection. For example, consider the intersection between two one-dimensional curves in a two-dimensional plane,  $D(S_1) = D(S_2) = 1$  and  $N = 2$ , therefore  $D_I = 0$ . It means that the intersecting set is composed of points for which the intersections are generic. It can be said that the codimension  $D - N$  is an additive for generally intersecting sets.

To apply these arguments to chaotic scattering problems, we consider a continuous-time system of phase-space dimension  $N + 2$ , that due to the energy conservation, the corresponding continuous-time flow is  $N + 1$  dimensional, so the scattering map is  $N$  dimensional. The dimensions of the stable and the unstable manifolds in the map are denoted by  $D_{s,0}$  and  $D_{u,0}$ . The box-counting dimension of the chaotic saddle is

$$D_0 = D_{s,0} + D_{u,0} - N = 2D_{s,0} - N \quad (66)$$

and, therefore

$$d_s = D_{s,0} + 1 - N, \quad (67)$$

where  $d_s$  is the box-counting dimension of the singularities of the scattering function. The relationship between both dimensions is

$$d_s = \frac{D_0 - N + 2}{2}. \quad (68)$$

Therefore, scattering singularities are observed if  $d_s > 0$ , which is fulfilled only if  $D_0 > N - 2$ .

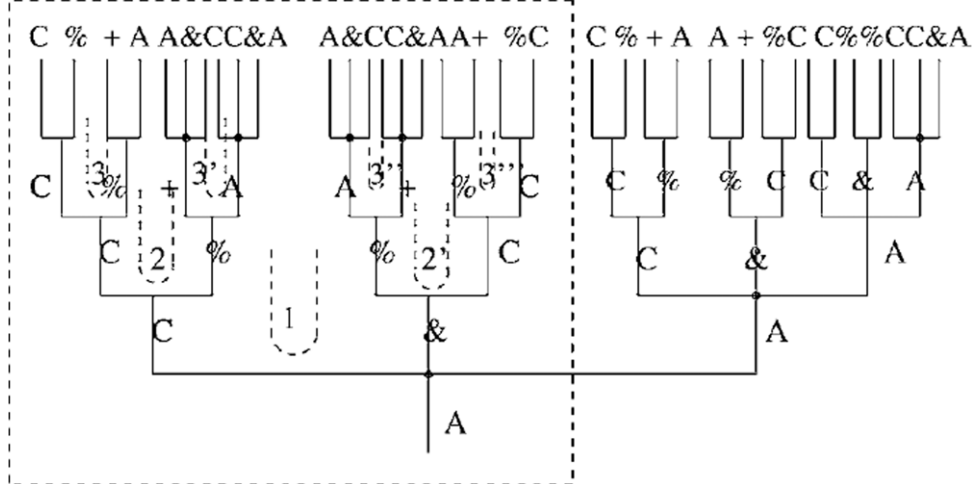


**Figure 78.** For the system described by equation (62), the branching tree and its symbolic encoding for scattering trajectories originated from the left. Reproduced with permission from [270]. Copyright 2006 American Physical Society.

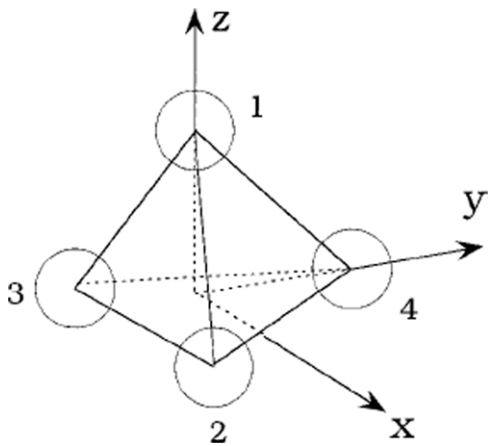


**Figure 79.** A schematic illustration of our scattering systems showing four Morse potential hills located at the vertices of a regular tetrahedron. Reproduced with permission from [269]. Copyright 2000 American Physical Society.

**9.5.2. Topology in high dimensions.** In the work by Lai *et al* [269], the authors found a change in the topology of the phase space in a three-dimensional system which exhibits chaotic scattering. For that purpose, the authors consider the following class of three degrees of freedom, time-independent Hamiltonian systems:  $H(\mathbf{x}, \mathbf{p}) = |\mathbf{p}|^2/2m + V(\mathbf{x})$ , where  $(\mathbf{x}, \mathbf{p})$  are the coordinate and momentum vectors and  $m$  is the particle mass. To be more specific and without loss of generality, we study the situation where there are four potential hills, located at the four vertices of a regular tetrahedron of unit side lengths, in the three-dimensional physical space. The locations of the vertices of the tetrahedron are  $(x_1, y_1, z_1) = (0, 0, \sqrt{2}/3)$ ,  $(x_2, y_2, z_2) = (1/2, -1/(2\sqrt{3}), 0)$ ,  $(x_3, y_3, z_3) = (-1/2, -1/(2\sqrt{3}), 0)$ , and  $(x_4, y_4, z_4) = (0, \sqrt{1/3}, 0)$ , as shown in figure 79. To mimic physical situations such as particle scattering by nonrotating diatomic molecules, we choose the Morse potential [302] for each hill, which has been a paradigm in chemical and atomic physics [303]. The potential due to each

Morse hill is  $V_M(\mathbf{x})$ , where  $\mathbf{x} = (x, y, z)$ , and

$$V_M(\mathbf{x}) = \frac{V_0}{2}[1 - e^{-\alpha(r_j - r_e)}]^2 - \frac{V_0}{2}, \quad (69)$$

where  $r_j = \sqrt{(x - x_j)^2 + (y - y_j)^2 + (z - z_j)^2}$  and  $V_0, \alpha$  and  $r_e$  are parameters of the Morse potential. The parameter  $\alpha$  is related to the steepness of the potential and  $r_e$  is the effective range of each potential hill. The constant  $-V_0/2$  ensures that the potential  $V_M(\mathbf{x}) \rightarrow 0$  as  $r \rightarrow \infty$ . Each Morse hill presents spherical symmetry and has a repulsive region, around  $\mathbf{x} = \mathbf{x}_j$ , surrounded by an attractive region. For  $r \gg r_e$ , the potential is negligible and the particles there can be considered in free motion. Notice that although we take as a prototype model the Morse potential, our results can be generalized for any other similar potential with a repulsive core and an attractive tail, such as the Lennard-Jones potential [304]. Our scattering system, in its dimensionless version, can be written as follows:

$$V_M(\mathbf{x}) = \sum_{j=1}^n V_m(\mathbf{x}), \quad (70)$$

where  $n = 4$  is the number of hills. Our phase space has a dimension equal to five since the energy is preserved. This potential is highly localized and we can consider the region around  $(x, y, z) = (0, 0, 0)$ , in which the interaction between the particle and the potential takes place, the scattering region.

The region given by  $V(\mathbf{x}) > E$  corresponds with the region of the three-dimensional physical space that is inaccessible to a particle with energy  $E$ . In the paper [269] the authors showed that for energies higher than a certain critical energy  $E_c$  and lower than  $E_0$ , the inaccessible part of space consists of four disconnected regions, each surrounding one vertex of the tetrahedron; they are approximately spherical in shape. As the energy decreases towards  $E_c$ , the inaccessible regions grow in radius; at  $E = E_c$  the previously disconnected regions touch each other. For  $E < E_c$ , the forbidden region is fully connected. This topological change in the configuration space causes a corresponding change in the dynamics of the system, as shown in [269].

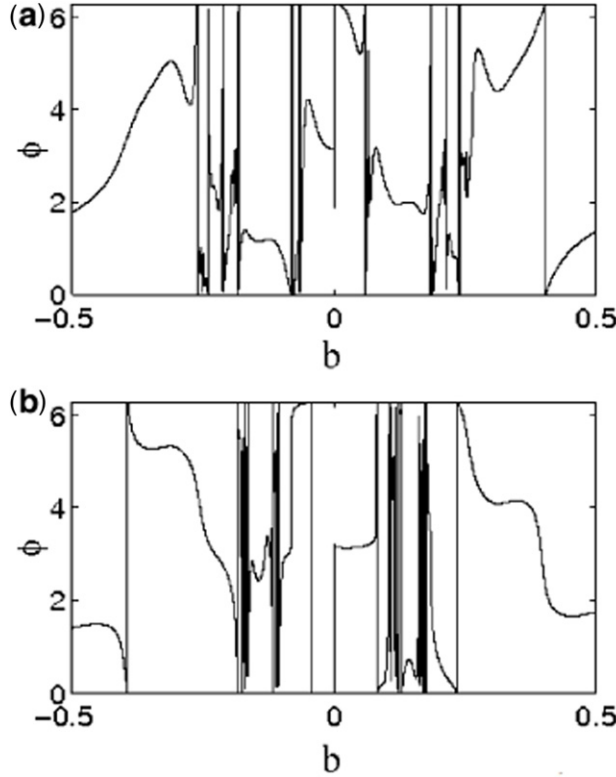


**Figure 80.** Deflection function: azimuthal angle  $\phi$  as a function of the impact parameter for (a)  $E = 4$  and (b)  $E = 1$ . Reproduced with permission from [269]. Copyright 2000 American Physical Society.

For this purpose, an exploration of the scattering function is necessary. Figure 80 shows, for  $E = 4$  and  $E = 1$  respectively,  $\phi$  after the scattering versus  $b$  and the deflection angle  $\phi(x_0)$  is recorded when the particles exit the scattering region. A Cantor set of singularities, typical in these physical situations, implies the presence of a chaotic saddle whose box-counting dimension is larger than two. The physical nature of the scattering observed at these energy values are quite different because of the topological change in the structure of the invariant set. This variation in the dimension of the chaotic saddle is shown in figure 81 in which the metamorphosis is observed at  $E = E_c$ .

We can also observe this metamorphosis if we analyze the structure of the exit basins associated with the phase space. For the tetrahedron configuration, there are four faces through which particles can exit. After the scattering, the particles in the initial face are color-coded, depending on through which side face they exit the system. Figures 82(a) and (b) show, for  $E = 4$  and  $E = 1$ , the corresponding basin structures. The transition is clearly observed since in figure 82(b) the basins are Wada.

**9.5.3. Chaotic set and cross section.** In the paper by Jung *et al* [305], they explore very important issues such as the chaotic set and the cross section in chaotic scattering with systems with three degrees of freedom. For that purpose, the authors take as a prototype model a scattering system with three degrees of freedom where one of them is open and the other two are closed. We imagine that the first degree of freedom is a

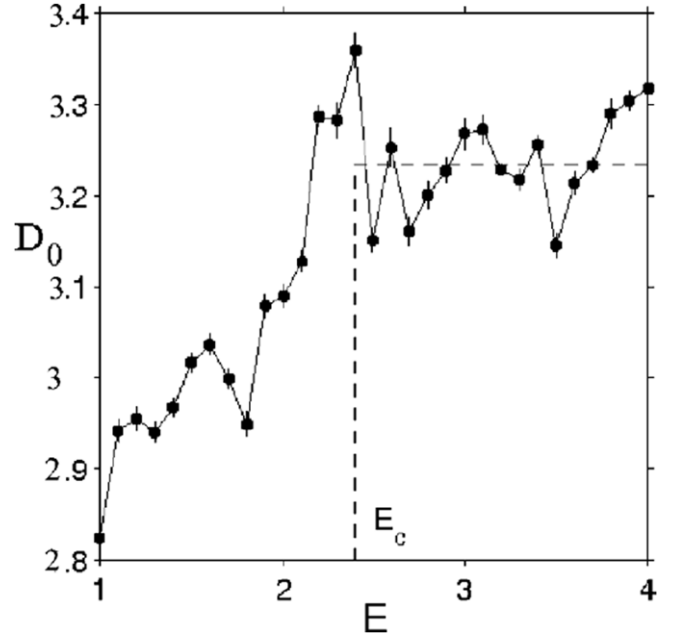


**Figure 81.** Box-counting dimension  $D_0$  of the chaotic saddle versus the energy  $E$ . The dimension remains practically constant for  $E > E_c$  and decreases as  $E$  is decreased through  $E_c$ . Reproduced with permission from [269]. Copyright 2000 American Physical Society.

translational degree of freedom between the projectile and the target, the second degree of freedom is vibrational and the third degree is a rotational degree of freedom. The corresponding Hamiltonian is written as follows

$$H = H_0 + W, \quad (71)$$

where  $H_0$  describes the asymptotic free motion and  $W$  is the short-range scattering potential. Therefore, the Hamiltonian in cylindrical coordinates reads

$$H = p^2/2 + p_\rho^2/2 + L^2/(2\rho^2) + \rho^2/2 - \frac{\exp(-D)}{D}, \quad (72)$$

where  $D^2 = q^2 + \rho^2(\sin^2(\theta) + (1+A)^2 \cos^2(\theta)) + 1$ .

Since the interaction potential of equation (72) is negative, there are trajectories with negative energy yet arbitrarily close to zero, going out extremely far and returning.

To investigate the chaotic set of this model, the authors of [305] start with the case of  $A = 0$  and later on break the symmetry. In order to show the results more clearly, the map version of our system can be written as follows

$$\begin{aligned} q_{n+1} &= q_n + p_n - (q_n + p_n/2) \\ &\times \exp(-(q_n + p_n/2)^2)(L_{\max} - L), \end{aligned} \quad (73)$$

$$p_{n+1} = p_n - 2(q_n + p_n/2) \exp(-(q_n + p_n/2)^2)(L_{\max} - L), \quad (74)$$

where, in this particular case,  $L_{\max} = 6, 23$ .

We can observe in figure 83 the horseshoe structure on the sequence of plots of the homoclinic tangle for the map. The intersection points between a stable and an unstable manifold are trajectories that converge forward and also backward in time to a fixed point of the map.

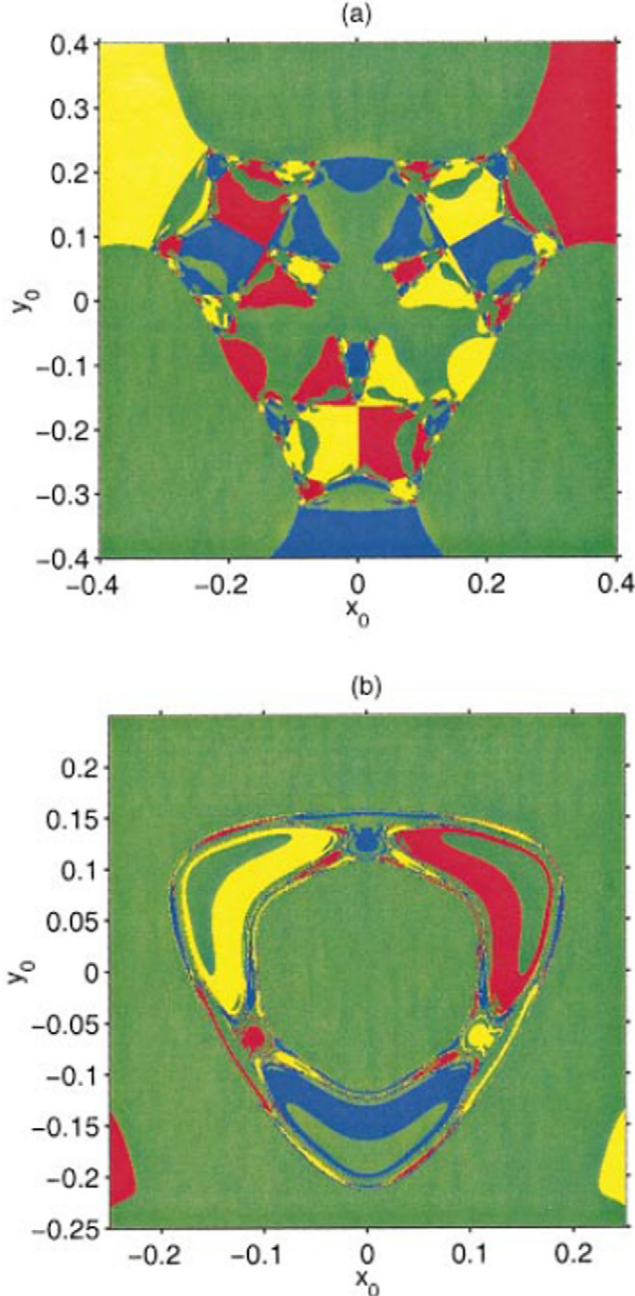


**Figure 82.** Basins of scattering trajectories for (a)  $E = 4$  and (b)  $E = 1$ . In (a) the basin boundaries common to the four colors consist of completely isolated points. In (b) the part of the basin boundary common to the four colors is connected and it is Wada. Reproduced with permission from [269]. Copyright 2000 American Physical Society.

On the other hand, scattering functions are interesting objects in their own right; we need them as an auxiliary concept to explain and motivate the ideas on the singularities in the cross sections, which are more accessible to experiments. As we have also defined in the Introduction of this review, a scattering function provides the outgoing asymptotic labels as a function of the initial asymptotic conditions. The typical scattering function for this system, with both smooth parts and singularities, is shown in figure 84, which is a characteristic in a fractal set.

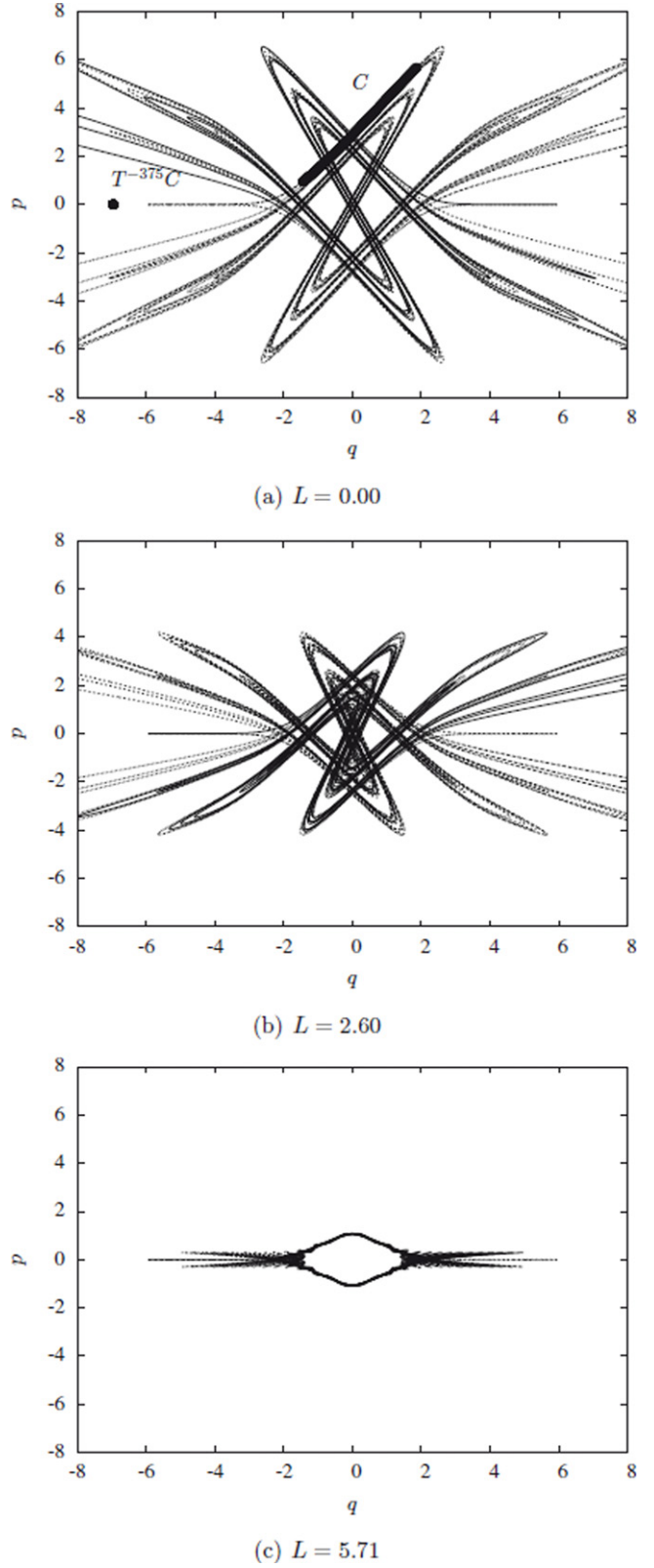


**Figure 83.** The Poincaré maps for the discrete dynamical system in the axial symmetric case ( $A = 0$ ). The  $L$  parameter regulates the degree of development of the horseshoe. Note also the reduction of the phase space occupied by the horseshoe as  $L$  increases [305].

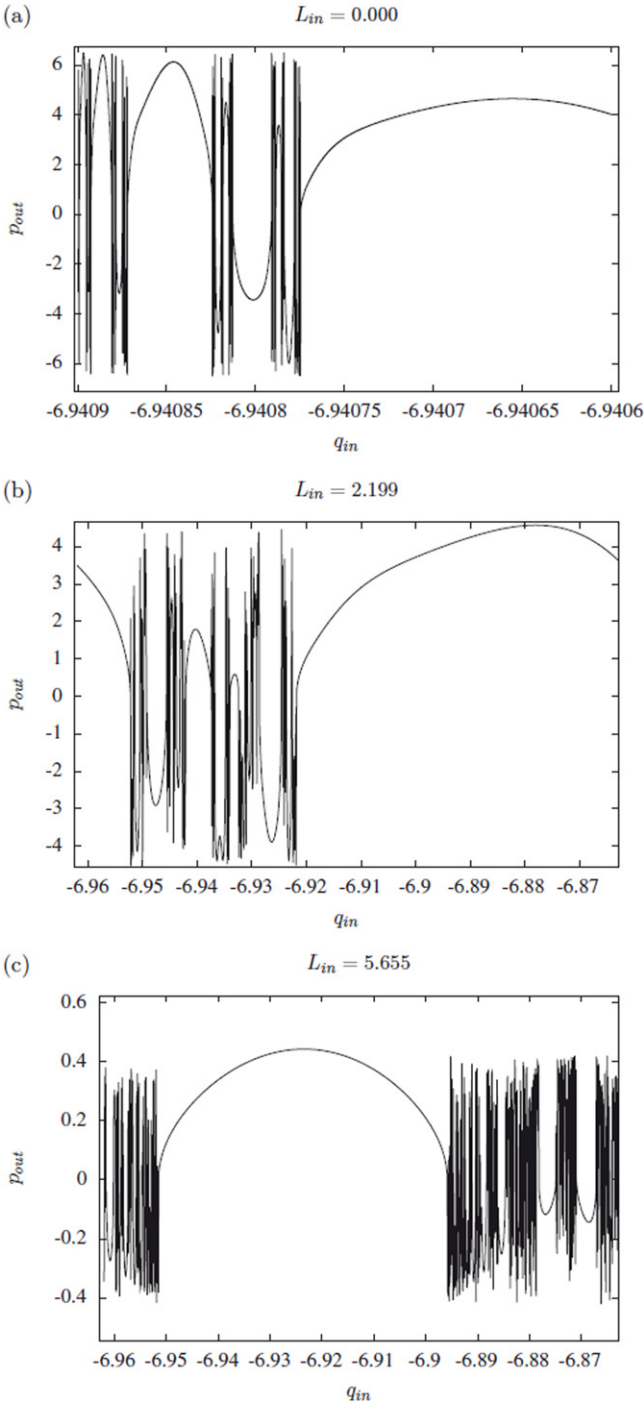


**Figure 84.** The  $p_{out}$  scattering function for the axial symmetric case in which the independent variable is the entrance phase  $q_{in}$  [305].

Finally, if we analyze the cross section of this system with three degrees of freedom, we observe rainbow singularities as we previously observed in the two-dimensional case [261], which are shown in figure 85. To obtain this figure, the authors of [305] have done a coarse graining of the domain of the cross section, which is similar to what any real detector in an experiment does. The domain is divided into many small rectangles and the counts in any one of these rectangles are registered. Each rectangle can be considered as one detector channel. After that procedure figure 85 is obtained in which

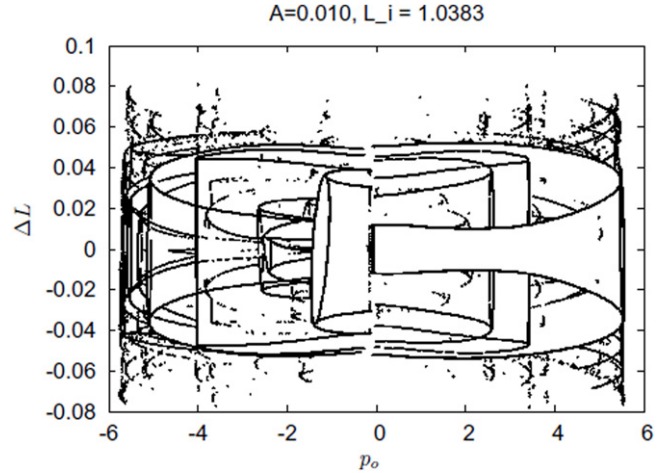


**Figure 85.** The rainbow singularities for the map system for  $A = 0.01$  and  $L_{in} = 1.0383$ . We show the structure of the projection of the half-torus repeated as far as resolution goes [305].

the shape of the half-toroidal mountains are recognized. The typical rainbow singularities are clearly shown [261].

## 10. Conclusions

There have been a lot of new developments in the last two decades in chaotic scattering phenomena. These appear in many applications in physics, including Celestial Mechanics, Atomic and Nuclear Physics, Fluid Mechanics, Nanophysics, etc, just to mention a few. In this review, we have shown and described different new aspects on chaotic scattering and the physical systems in which they can be found. We have also described some of the experiments where these phenomena have been observed. Even though most of the cases correspond to conservative systems, quite often in realistic situations the system is subjected to external perturbations. We have also included in our discussion the analysis of the effects of these kinds of perturbations on chaotic scattering phenomena, such as dissipation and noise. The typical transitions which characterize the dynamics and the topology of chaotic scattering phenomena have been also analyzed.

Among the main conclusions we can mention:

- The structure of the phase space in chaotic scattering phenomena is usually very complex, including the existence of fractal basins and Wada basins giving rise to unpredictable dynamics. These kinds of structures are very common in chaotic scattering systems, from which we can mention the Hénon–Heiles system, the Contopoulos system and the three-disk system, among others.
- Chaotic scattering is also present in billiard systems and in driven barriers for which the particles escape from the scattering region according to a power or exponential law. These kinds of systems also have implications in mesoscopic electronic semiconductor devices, phonon in quartz blocks, etc. Experimental systems concerning these phenomena are also described in some detail. Furthermore, some of the scattering

- parameters important for a correct understanding of chaotic scattering phenomena have been measured and tested experimentally.
- The effects of weak perturbations such as dissipation and noise have been also described. These perturbations are characteristics of the environment; the influence on the dynamics and topology is quite relevant. Noise helps the particles to escape from the scattering region faster as compared with the conservative noiseless case. Dissipation converts the KAM islands into attractors and drastically changes the decay law of the particles in the scattering region.
  - Finally, the importance of other topics relating to chaotic scattering has been also discussed. Issues such as the presence of time-dependent potentials, which has importance in problems of electrons in the potential fields of atoms, the different transitions in chaotic scattering phenomena and the types of boundaries, have been considered. Besides, some prospection on high-dimensional chaotic scattering has been also carried out, showing the changes produced by the topology due to higher dimensional problems.
- Finally, we expect that the results described in this review paper will be useful for a better understanding of chaotic scattering phenomena, their implications and their relevance in different fields in physics and natural sciences.
- ### Acknowledgments
- We would like to thank Professor Ying-Cheng Lai for the fruitful discussions and encouragement we have had during the development of this work. We appreciate the productive comments and advice we have received from numerous colleagues during the writing of this manuscript. Among them, we would like to mention Liang Huang, Hiroyasu Ando, Roberto Barrio, Fernando Blesa, Pinpin Li, Alessandro P S de Moura, Jaison Novick, Sergey Prants, Haris Skokos, David Guéry-Odelin, Inés P Mariño, Alexandre Wagemakers, Samuel Zambrano, Sijo K Joseph, Juan B Seoane and Carl Dettmann. This work was financed by the Spanish Ministry of Science and Innovation under project number FIS2009-09898.
- ### References
- [1] Lai Y C and Tél T 2010 *Transient Chaos: Complex Dynamics on Finite-Time Scales* (New York: Springer)
  - [2] Tél T and Gruiz M 2006 *Chaotic Dynamics: an Introduction Based on Classical Mechanics* (Cambridge: Cambridge University Press)
  - [3] Ott E 2002 *Chaos in Dynamical Systems* (Cambridge: Cambridge University Press)
  - [4] Joachain C J 1975 *Quantum Collision Theory* (Amsterdam: North-Holland)
  - [5] Bleher S, Grebogi C and Ott E 1990 *Physica D* **46** 87
  - [6] Ott E and Tél T 1993 *Chaos* **3** 4
  - [7] Tél T 1989 *J. Phys. A: Math. Gen.* **22** L691
  - [8] Jung C, Mejia-Monasterio C and Seligman T H 1995 *Phys. Lett. A* **198** 306
  - [9] Mandelbrot B 1983 *The Fractal Geometry of Nature* (New York: Freeman)
  - [10] Devaney R 1986 *An Introduction to Chaotic Dynamical Systems* (Menlo Park, CA: Benjamin/Cummings)
  - [11] Peitgen H O and Richter P H 1986 *The Beauty of Fractals* (Berlin: Springer)
  - [12] Feder J 1988 *Fractals* (New York: Plenum)
  - [13] Eckhardt B 1987 *J. Phys. A: Math. Gen.* **20** 5971
  - [14] Gaspard P and Rice S A 1989 *J. Chem. Phys.* **90** 2225
  - [15] Poon L, Campos J, Ott E and Grebogi C 1996 *Int. J. Bifurcation Chaos* **6** 251
  - [16] Altmann E and Tél T 2008 *Phys. Rev. E* **79** 1
  - [17] Dettmann C P and Georgiou O 2011 *Phys. Rev. E* **83** 036212
  - [18] Dettmann C P and Leonel E D 2012 *Physica D* **241** 403
  - [19] Seoane J M, Aguirre J, Sanjuán M A F and Lai Y C 2006 *Chaos* **16** 023101
  - [20] Narnhofer H 1980 *Phys. Rev. D* **22** 2387
  - [21] Narnhofer H and Thirring W 1981 *Phys. Rev. A* **23** 1688
  - [22] Nusse H E and Yorke J A 1996 *Science* **271** 1376
  - [23] Aguirre J, Vallejo J C and Sanjuán M A F 2001 *Phys. Rev. E* **64** 066208
  - [24] Alligood K T, Sauer T D and Yorke J A 1996 *Chaos: An Introduction to Dynamical Systems* (Berlin: Springer)
  - [25] Contopoulos G 2002 *Order and Chaos in Dynamical Astronomy* (Berlin: Springer)
  - [26] Gottesman S T, Buchler J R and Mahon M E 2005 *Nonlinear Dynamics in Astronomy and Physics* (New York: The New York Academy of Sciences)
  - [27] Karney C F F 1983 *Physica D* **8** 360
  - [28] Moser J 1973 *Stable and Random Motions in Dynamical Systems* (Princeton, NJ: Princeton University Press)
  - [29] Chirikov B V and Shepelyansky D 1984 *Physica D* **13** 395
  - [30] Lai Y C, Ding M, Grebogi C and Blümel R 1992 *Phys. Rev. A* **46** 4661
  - [31] Meiss J D and Ott E 1986 *Physica D* **20** 387
  - [32] Gaspard P 1998 *Chaos, Scattering and Statistical Mechanics* (Cambridge: Cambridge University Press)
  - [33] MacKay R S and Meiss J D 1987 *Hamiltonian Dynamical Systems: A Reprint Selection* (Bristol: Hilger)
  - [34] MacKay R S 1993 *Renormalisation in Area-Preserving Maps* (Singapore: World Scientific)
  - [35] Arnold V I 1978 *Mathematical Methods of Classical Mechanics* (New York: Springer)
  - [36] Lichtenberg A J and Lieberman M A 1983 *Regular and Stochastic Motion* (New York: Springer)
  - [37] Wiggins S 2010 *Introduction to Applied Nonlinear Dynamical Systems and Chaos* (Berlin: Springer)
  - [38] Kantz H and Grassberger P 1985 *Physica D* **17** 75
  - [39] Hsu G H, Ott E and Grebogi C 1988 *Phys. Lett. A* **127** 199
  - [40] Gaspard P 1993 *Chaos* **3** 427
  - [41] Tél T 1991 *Phys. Rev. A* **44** 1034
  - [42] Ott E, Sauer T and Yorke J A 1989 *Phys. Rev. A* **39** 4212
  - [43] Tél T 1989 *J. Phys. A: Math. Gen.* **22** L691
  - [44] Cvitanovic P 1992 *Chaos* **2** 1
  - [45] Hietarinta J and Mikkola S 1993 *Chaos* **3** 183
  - [46] Hénon M 1988 *Physica D* **33** 132
  - [47] Boyd P T and McMillan S L W 1993 *Chaos* **3** 507
  - [48] Benet *et al* 2000 *Prog. Theor. Phys. Suppl.* **139** 234
  - [49] Chernikov A A and Schmidt G 1993 *Chaos* **3** 525
  - [50] Chen J 1992 *J. Geophys. Res.* **97** 15011
  - [51] Lau Y T and Finn J M 1991 *Astrophys. J.* **366** 577
  - [52] Ohanian H C 2006 *Classical Electrodynamics* (Hingham, MA: Infinity Science Books)
  - [53] Aref H 1984 *J. Fluid. Mech.* **143** 1
  - [54] Aref H, Kadirkaraj B, Zawadski I, Campbell L J and Eckhardt B 1988 *Fluid. Dyn. Res.* **3** 63
  - [55] van Heist G J F and Flor J B 1989 *Nature* **340** 212
  - [56] Ottino J M 1988 *The Kinematics of mixing: Stretching, Chaos, and Transport* (Cambridge: Cambridge University Press)
  - [57] Aref H 1983 *Annu. Rev. Fluid. Fluid. Mech.* **15** 345

- [58] Rom-Kedar V, Leonard A and Wiggins S 1990 *J. Fluid. Mech.* **214** 347
- [59] Jones S and Aref H 1988 *Phys. Fluids* **31** 469
- [60] Jung C and Ziemniak E 1992 *J. Phys. A: Math. Gen.* **25** 3929
- [61] Jung C, Tél T and Ziemniak E 1993 *Chaos* **3** 555
- [62] Rankin C C and Miller W H 1971 *J. Chem. Phys.* **55** 3150
- [63] Agmon N 1982 *J. Chem. Phys.* **76** 1309
- [64] Noid D W, Gray S K and Rice S A 1986 *J. Chem. Phys.* **84** 2649
- [65] Pollak E and Pechukas P 1978 *J. Chem. Phys.* **69** 1218
- [66] Someda K, Ramaswamy R and Naramura H 1993 *J. Chem. Phys.* **98** 1156
- [67] Skodje R T and Davies M J 1988 *J. Chem. Phys.* **88** 2429
- [68] Koch B P and Bruhn B 1993 *Chaos* **3** 443
- [69] Lai Y C, Tél T and Grebogi C 1993 *Phys. Rev. E* **48** 709
- [70] Founariotakis M, Farantos S C, Skokos C and Contopoulos G 1997 *Chem. Phys. Lett.* **277** 456
- [71] Richter K and Kaneko K 1990 *J. Phys. B: At. Mol. Opt. Phys.* **23** L197
- [72] Yamamoto T and Kaneko K 1993 *Phys. Rev. Lett.* **70** 1928
- [73] Ezra G S, Richter K, Tanner G and Wintgen D 1991 *J. Phys. B: At. Mol. Opt. Phys.* **24** L413
- [74] Wintgen D, Richter K and Tanner G 1992 *Chaos* **2** 19
- [75] Yuan J M and Gu Y 1993 *Chaos* **3** 569
- [76] Tersigni S H, Gaspard P and Rice R S 1991 *J. Chem. Phys.* **92** 1775
- [77] Jensen R V 1982 *Phys. Rev. Lett.* **49** 1365
- [78] Beeker A and Eckelt P 1993 *Chaos* **3** 487
- [79] Rapisarda A and Baldo M 1991 *Phys. Rev. Lett.* **66** 2581
- [80] Baldo M, Lanza E G and Rapisarda A 1993 *Chaos* **3** 691
- [81] Bardou F, Bouchaud J P, Aspect A and Cohen-Toannoudji C 2002 *Lévy Statistics and Laser Cooling* (Cambridge: Cambridge University Press)
- [82] Kolovsky A R and Korsch H J 1997 *Phys. Rev. A* **55** 1
- [83] Argonov V Y and Prants S V 2003 *J. Exp. Theor. Phys.* **96** 832
- [84] Argonov V Y and Prants S V 2005 *Phys. Rev. A* **71** 053408
- [85] Argonov V Y and Prants S V 2006 *J. Russ. Laser Res.* **27** 360
- [86] Argonov V Y and Prants S V 2007 *Phys. Rev. A* **75** 063428
- [87] Prants S V 2012 *Europhys. Lett.* **99** 20009
- [88] Prants S V and Vitkovsky V O 2012 *J. Russ. Laser Res.* **33** 293
- [89] Beenakker C W J 1997 *Rev. Mod. Phys.* **69** 731
- [90] Mitchell G E, Richter A and Weidenmüller H A 2010 *Rev. Mod. Phys.* **82** 2845
- [91] Nonnenmacher S and Zworski M 2009 *Acta Math.* **203** 149
- [92] Jung C, Mejía-Monasterio C, Merlo O and Seligman T H 2004 *New J. Phys.* **6** 2004
- [93] Blümel R and Smilansky U 1989 *Phys. Rev. Lett.* **60** 477
- [94] Blümel R and Smilansky U 1989 *Physica D* **36** 111
- [95] Doron E, Smilansky U and Frenkel A 1990 *Phys. Rev. Lett.* **65** 3072
- [96] Lai Y C, Blümel R, Ott E and Grebogi C 1992 *Phys. Rev. Lett.* **68** 3491
- [97] Yang R, Huang L, Lai Y C and Grebogi C 2011 *Europhys. Lett.* **94** 40004
- [98] Huang L, Lai Y C, Ferry D K, Goodnick S M and Akis R 2009 *Phys. Rev. Lett.* **103** 054101
- [99] Coakley K J, Doyle J M, Dzhosyuk S N, Yang L and Huffman P R 2005 *J. Res. Natl Inst. Stand. Technol.* **110** 367
- [100] Lin Y D, Barr A, Na K and Reichl L E 2011 *Phys. Rev. E* **83** 056217
- [101] Gattobigio G L, Couvert A, Georgeot B and Gúery-Odelin D 2011 *Phys. Rev. Lett.* **107** 254104
- [102] Novick J, Keeler M L, Giefer J and Delos J B 2012 *Phys. Rev. E* **85** 016205
- [103] Poli J, Luna-Acosta G A and Stöckmann H-J 2012 *Phys. Rev. Lett.* **108** 174101
- [104] Yang R, Huang L, Lai Y C and Pecora L M 2012 *Appl. Phys. Lett.* **100** 093105
- [105] Gattobigio G L, Couvert A, Reinaudi G, Georgeot B and Gúery-Odelin D 2012 *Phys. Rev. Lett.* **109** 030403
- [106] Datta S 1995 *Chaos, Electronic Transport in Mesoscopic Systems* (Cambridge: Cambridge University Press)
- [107] Eckmann J P, Mejía-Monasterio C and Zabey E 2006 *J. Stat. Phys.* **123** 1339
- [108] Keller J B, Kay I and Shmoys J 1956 *Phys. Rev.* **102** 557
- [109] Newton R G 1982 *Scattering Theory of Waves and Particles* (Berlin: Springer)
- [110] Jung C, Lipp C and Seligman T H 1999 *Ann. Phys.* **275** 151
- [111] Tél T and Lao B L (ed) 1990 *Directions in Chaos* vol 3 (Singapore: World Scientific)
- [112] Tapia H and Jung C 2003 *Phys. Lett. A* **313** 198
- [113] Weissbluth M 1978 *Atoms and Molecules* (San Diego, CA: Academic)
- [114] Kovacs Z and Wiesenfeld L 1995 *Phys. Rev. E* **51** 5476
- [115] Lax P D and Phillips R S 1967 *Scattering Theory* (New York: Academic)
- [116] Ding J 1998 *Proc. Am. Math. Soc.* **126** 1355
- [117] Anosov D V 1967 *Proc. Steklov Inst. Math.* **90** 235
- [118] Sinai Ya G 1972 *Russ. Math. Surv.* **27** 21
- [119] Bowen R and Ruelle D 1975 *Invent. Math.* **29** 181
- [120] Ruelle D 1978 *Thermodynamic Formalism* (Reading, MA: Addison-Wesley)
- [121] Gaspard P and Dorfman J R 1995 *Phys. Rev. E* **52** 3525
- [122] Gaspard P and Baras F 1995 *Phys. Rev. E* **51** 5332
- [123] Bauer L and Reiss E L 1978 *SIAM J. Appl. Math.* **35** 508
- [124] Redner S 2001 *A Guide to First-Passage Processes* (Cambridge: Cambridge University Press)
- [125] Van Kampen N G 1992 *Stochastic processes in Physics and Chemistry* (Amsterdam: North-Holland)
- [126] Aguirre J, Viana R L and Sanjuán M A F 2009 *Rev. Mod. Phys.* **81** 333
- [127] Mandelbrot B B 1975 *Les Objects Fractals, Forme, Hasard et Dimension* (Paris: Flammarion)
- [128] Aguirre J and Sanjuán M A F 2002 *Physica D* **171** 41
- [129] Bellido F and Ramírez-Malo J B 2006 *Int. J. Non-Linear Mech.* **41** 860
- [130] Huisman J and Weissing F J 2001 *Am. Naturalist* **157** 488
- [131] Vandermeer J, Stone L and Blasius B 2004 *Chaos, Solitons Fractals* **12** 265
- [132] Marcos S H C, Lopes S R and Viana R L 2003 *Chaos, Solitons Fractals* **15** 417
- [133] Gong P L and Xu J X 2001 *Phys. Rev. E* **63** 031906
- [134] Grebogi C, Ott E and Yorke J A 1983 *Phys. Rev. Lett.* **50** 935
- [135] Cartwright M L and Littlewood J E 1951 *Ann. Math.* **54** 1
- [136] Levinson N 1949 *Ann. Math.* **50** 127
- [137] Levi M 1981 *Mem. Am. Math. Soc.* **32** 244
- [138] Hocking J and Young G 1961 *Topology* (Reading, MA: Addison-Wesley)
- [139] Kennedy J and Yorke J A 1991 *Physica D* **51** 213
- [140] Zhang Y and Lou G 2012 *Phys. Lett. A* **376** 3060
- [141] Toroczkai Z, Károlyi G, Péntek Á, Tél T, Grebogi C and Yorke J A 1997 *Physica A* **239** 235
- [142] Sanjuán M A F, Kennedy J, Grebogi C and Yorke J A 1997 *Chaos* **7** 125
- [143] Kennedy J, Sanjuán M A F, Yorke J A and Grebogi C 1999 *Topol. Appl.* **94** 207
- [144] Sanjuán M A F, Kennedy J, Ott E and Yorke J A 1997 *Phys. Rev. Lett.* **78** 1892
- [145] Nusse H E and Yorke J A 1996 *Science* **271** 1376
- [146] Nusse H E and Yorke J A 1996 *Physica D* **90** 242
- [147] Nusse H E and Yorke J A 2000 *Phys. Rev. Lett.* **84** 626
- [148] Sweet D, Ott E and Yorke J A 1999 *Nature* **399** 315
- [149] Newhouse S E 1980 *Dynamical Systems (C.I.M.E. Lectures)* ed J Guckenheimer *et al* (Boston, MA: Birkhäuser)
- [150] You Z, Kostelich E and Yorke J A 1991 *Int. Bifurcation. Chaos* **1** 605
- [151] Hénon M and Heiles C 1964 *Astron. J.* **69** 73

- [152] Churchill R, Pecelli G and Rod D 1975 *J. Diff. Eqns.* **17** 329
- [153] Barrio F, Blesa F and Serrano S 2010 *Int. J. Bifurcation. Chaos* **20** 1293
- [154] Blesa F, Piasecki S, Dena A and Barrio R 2012 *Int. J. Mod. Phys. C* **23** 1250014
- [155] de Moura A P S and Letelier P S 1999 *Phys. Lett. A* **256** 362
- [156] Barrio R, Blesa F and Serrano S 2008 *Europhys. Lett.* **82** 10003
- [157] Zhao H J and Du M L 2007 *Phys. Rev. E* **76** 027201
- [158] Contopoulos G 1990 *Astron. Astrophys.* **231** 41
- [159] Kandrup H E, Siopis C, Contopoulos G and Dvorak R 1999 *Chaos* **9** 381
- [160] Churchill R, Pecelli G and Rod D 1980 *Arch. Ration. Mech. Anal.* **73** 313
- [161] Sepúlveda A M and Heller E J 1994 *J. Chem. Phys.* **101** 8016
- [162] Babuška D, Wyatt R E and Frederick J H 2003 *J. Chem. Phys.* **119** 6482
- [163] Barrio R, Blesa F and Serrano S 2009 *New J. Phys.* **11** 053004
- [164] Gaspard P and Rice S A 1989 *J. Chem. Phys.* **90** 2242
- [165] Gaspard P and Rice S A 1989 *J. Chem. Phys.* **90** 2255
- [166] Gaspard P and Rice S A 1989 *J. Chem. Phys.* **91** E3279
- [167] Landau L D and Lifshitz E M 1976 *Mechanics* (Oxford: Butterworth-Heinemann)
- [168] Roukes M L and Alerhand O L 1989 *Phys. Rev. Lett.* **65** 1857
- [169] Jalabert R A, Baranger H U and Stone A D 1990 *Phys. Rev. Lett.* **65** 2442
- [170] Walker J 1988 *Sci. Am.* **259** 112
- [171] Korsch H J and Wagner A 1991 *Comput. Phys.* **5** 497
- [172] Stöckmann H J 1999 *Quantum Chaos: An Introduction* (Cambridge: Cambridge University Press)
- [173] Gräf H D, Harney H L, Lengeler H, Lewenkopf C H, Rangacharyulu C, Richter A, Schardt P and Weidenmüller H A 1992 *Phys. Rev. Lett.* **69** 1296
- [174] Stein J and Stöckmann H J 1992 *Phys. Rev. Lett.* **68** 2867
- [175] Bunimovich L A and Dettmann C P 2005 *Phys. Rev. Lett.* **94** 100201
- [176] Sridhar S 1991 *Phys. Rev. Lett.* **67** 785
- [177] Persson E, Rotter I, Stöckmann H J and Barth M 2000 *Phys. Rev. Lett.* **85** 2478
- [178] Sweet D, Zeff B W, Ott E and Lathrop D P 2001 *Physica D* **154D** 207
- [179] Ellegaard C, Guhr T, Lindemann K, Nygård J and Oxborow M 1996 *Phys. Rev. Lett.* **77** 4918
- [180] Milner V, Hanssen J L, Campbell W C and Raizen M G 2001 *Phys. Rev. Lett.* **86** 1514
- [181] Friedman N, Kaplan A, Carasso D and Davidson N 2001 *Phys. Rev. Lett.* **86** 1518
- [182] Main J 1999 *Phys. Rep.* **316** 233
- [183] Forrester P J, Snaith N C and Verbaarschot J J M 2003 *J. Phys. A* **36** R1
- [184] Taylor R P *et al* 1997 *Phys. Rev. Lett.* **78** 1952
- [185] Lenz F, Diakonos F K and Schmelcher P 2007 *Europhys. Lett.* **79** 20002
- [186] Karlis A K, Papachristou P K, Diakonos F K, Constantoudis V and Schmelcher P 2006 *Phys. Rev. Lett.* **97** 194102
- [187] Koiller J, Markarian R, Oliffson Kamphorst S and Pinto de Carvalho S 1996 *J. Stat. Phys.* **83** 127
- [188] Koiller J, Markarian R, Oliffson Kamphorst S and Pinto-de-Carvalho S 1995 *Nonlinearity* **8** 983
- [189] Berry M V 1982 *Eur. J. Phys.* **2** 91
- [190] Lenz F, Diakonos F K and Schmelcher P 2008 *Phys. Rev. Lett.* **100** 014103
- [191] McDonald S W, Grebogi C, Ott E and Yorke J A 1985 *Physica D* **17** 125
- [192] Harayama T and Davis P 1998 *Opt. Lett.* **23** 1426
- [193] Eubank S and Farmer J D 1990 *An Introduction to Chaos and Randomness* ed E Jen (Redwood City, CA: Addison-Wesley)
- [194] Di Ventra M 2008 *Electrical Transport in Nanoscale Systems* (Cambridge: Cambridge University Press)
- [195] Datta S 2005 *Quantum Transport: Atom to Transistor* (Cambridge: Cambridge University Press)
- [196] Koch F R N, Lenz F, Petri C, Diakonos F K and Schmelcher P 2008 *Phys. Rev. E* **78** 056204
- [197] Buttiker M and Landauer R 1982 *Phys. Rev. Lett.* **49** 1739
- [198] Hagmann M J 1995 *Appl. Phys. Lett.* **66** 789
- [199] Pimpale A, Holloway S and Smith R J 1991 *J. Phys. A: Math. Gen.* **24** 3533
- [200] Hanson R, Kouwenhoven L P, Petta J R, Tarucha S and Vandersypen M K 2007 *Rev. Mod. Phys.* **79** 1217
- [201] Davies J H 1998 *The Physics of Low-Dimensional Semiconductors* (Cambridge: Cambridge University Press)
- [202] Lau Y T, Finn J M and Ott E 1991 *Phys. Rev. Lett.* **66** 978
- [203] Hilborn R C 2000 *Chaos and Nonlinear Dynamics* (Oxford: Oxford University Press)
- [204] Mandelbrot B 2004 *Fractals and Chaos* (Berlin: Springer)
- [205] Ruelle D and Takens F 1977 *Commun. Math. Phys.* **20** 167
- [206] Hausdorff F 1918 *Math. Ann.* **79** 157
- [207] Peitgen H-O, Jürgen H and Saupe D 1992 *Chaos and Fractals: New Frontiers of Science* (Berlin: Springer)
- [208] Motter A and Lai Y C 2001 *Phys. Rev. E* **63** 015205
- [209] Grebogi C, Nusse H E, Ott E and Yorke J A 1988 *Dynamic Systems (Springer Lecture Notes in Mathematics)* vol 1342 p 220
- [210] Seoane J M and Sanjuán M A F 2010 *Int. J. Bifurcation Chaos* **9** 2783
- [211] Lai Y C 1999 *Phys. Rev. E* **60** R6283
- [212] Jung C and Tél T 1993 *Chaos* **3** 555
- [213] Motter A E, Lai Y C and Grebogi C 2003 *Phys. Rev. E* **68** 056307
- [214] Do Y and Lai Y C 2003 *Phys. Rev. Lett.* **91** 224101
- [215] Do Y and Lai Y C 2004 *Phys. Rev. E* **70** 036203
- [216] Eckhardt B and Jung C 1986 *Physica A* **19** L829
- [217] Vilela R D and Motter A E 2007 *Phys. Rev. Lett.* **99** 264101
- [218] Budyansky M, Uleysky M and Prants S 2004 *Physica D* **195** 369
- [219] Sommerer J C, Ku H-C and Gilreath H E 1996 *Phys. Rev. Lett.* **77** 5055
- [220] Jung C and Ziemniak E M 1992 *J. Phys. A: Math. Gen.* **25** 3929
- [221] Tél T, Ziemniak E M and Jung C 1994 *Physica D* **76** 123
- [222] Ziemniak E M and Jung C 1995 *J. Phys. Lett. A* **202** 263
- [223] Amano K, Narimatsu D, Sotome S, Tashiro S, Uchida A and Yoshimori S 2007 *Phys. Rev. E* **76** 046213
- [224] Sweet D, Ott E and Yorke J A 1999 *Nature* **399** 315
- [225] Viana R L, Da Silva E C, Kroetz T, Caldas I L, Roberto M and Sanjuán M A F 2011 *Phil. Trans. R. Soc. A* **369** 371
- [226] Kennedy J and Yorke J A 1991 *Physica D* **51** 213
- [227] Tufaile A and Tufaile A P B 2011 *Phys. Lett. E* **375** 3693
- [228] Tufaile A and Tufaile A P B 2008 *Phys. Lett. E* **372** 6391
- [229] Eckhardt B and Aref H 1988 *Trans. R. Soc. Lond. A* **326** 655
- [230] Péntek Á, Toroczkai Z, Tél T, Grebogi C and Yorke J A 1995 *Phys. Rev. E* **51** 4076
- [231] Stolovitzky G, Kaper T J and Sirovich L 1995 *Chaos* **5** 671
- [232] Maxey M R and Riley J J 1983 *Phys. Fluids* **26** 883
- [233] Lai Y C, Ding M, Grebogi C and Blümel R 1992 *Phys. Rev. A* **46** 4661
- [234] Feudel U and Grebogi C 1997 *Chaos* **7** 597
- [235] Seoane J M, Sanjuán M A F and Lai Y C 2007 *Phys. Rev. E* **76** 016208
- [236] Bleher S, Ott E and Grebogi C 1989 *Phys. Rev. Lett.* **63** 919
- [237] Grebogi C, McDonald S W, Ott E and Yorke J A 1983 *Phys. Lett. A* **99** 415
- [238] McDonald S W, Grebogi C, Ott E and Yorke J A 1985 *Physica D* **17** 125
- [239] Hsu G, Ott E and Grebogi C 1988 *Phys. Lett. A* **127** 199

- [240] Aguirre J, Vallejo J C and Sanjuán M A F 2001 *Phys. Rev. E* **64** 066208
- [241] Elyutin P V 2004 *Phys. Rev. E* **69** 026205
- [242] Seoane J M and Sanjuán M A F 2008 *Phys. Lett. A* **372** 110
- [243] Seoane J M, Huang L, Lai Y C and Sanjuán M A F 2009 *Phys. Rev. E* **79** 047202
- [244] Blesa F, Seoane J M, Barrio R and Sanjuán M A F 2012 *Int. J. Bifurcation Chaos* **22** 1230010
- [245] Aguirre J, D’Ovidio F and Sanjuán M A F 2004 *Phys. Rev. E* **69** 016203
- [246] Kloeden P E and Platen E 1999 *Numerical Solution of Stochastic Differential Equations* (Berlin: Springer)
- [247] Ott E, Yorke J D and Yorke J A 1985 *Physica D* **16** 62
- [248] Mills P 2006 *Commun. Nonlinear Sci. Numer. Simul.* **11** 899
- [249] Gan C and Yang S 2010 *Phys. Rev. E* **82** 066204
- [250] Rodrigues C S, de Moura A P S and Grebogi C 2010 *Phys. Rev. E* **82** 026211
- [251] Altmann E G and Endler A 2010 *Phys. Rev. Lett.* **105** 244102
- [252] Drake S, Dettmann C P, Frankel N E and Cornish N J 1996 *Phys. Rev. E* **53** 1351
- [253] Dettmann C P, Frankel N E and Cornish N J 1994 *Phys. Rev. D* **50** R618
- [254] Dettmann C P, Frankel N E and Cornish N J 1995 *Fractals* **3** 161
- [255] Rice S A and Gaspard P 1990 *Israel J. Chem.* **30** 23
- [256] Troll G and Smilansky U 1989 *Physica D* **35** 34
- [257] Lai Y C and Grebogi C 1991 *Int. J. Bifurcation Chaos* **3** 667
- [258] Fermi E 1949 *Phys. Rev.* **75** 1169
- [259] Lai Y C 1999 *Phys. Rev. E* **60** R6283
- [260] Ding M, Grebogi C, Ott E and Yorke J A 1990 *Physica D* **47** 87
- [261] Schelin A B, de Moura A P S and Grebogi C 2008 *Phys. Rev. E* **78** 046204
- [262] de Moura A P S and Grebogi C 2002 *Phys. Rev. E* **65** 035206R
- [263] Nussenzveig H M 1992 *Diffraction Effects in Semiclassical Scattering* (Cambridge: Cambridge University Press)
- [264] Lai Y C and Grebogi C 1994 *Phys. Rev. E* **49** 3761
- [265] Aguirre J, Viana R L and Sanjuán M A F 2009 *Rev. Mod. Phys.* **81** 333
- [266] de Moura A P S and Grebogi C 2002 *Phys. Rev. E* **66** 046214
- [267] Péntek A, Toroczkai Z, Tél, Grebogi C and Yorke J A 1995 *Phys. Rev. E* **51** 4076
- [268] Grebogi C, Kostelich E, Ott E and Yorke J A 1987 *Physica D* **25** 347
- [269] Lai Y C, de Moura A P S and Grebogi C 2000 *Phys. Rev. E* **62** 6421
- [270] Emmanouilidou A and Jung C 2006 *Phys. Rev. E* **73** 016219
- [271] Christiansen F and Politi A 1995 *Phys. Rev. E* **51** R3811
- [272] Christiansen F and Politi A 1996 *Nonlinearity* **9** 1623
- [273] Smale S 1967 *Bull. Am. Math. Soc.* **73** 747
- [274] Jung C and Emmanouilidou A 2005 *Chaos* **15** 023101
- [275] Emmanouilidou A and Reichl L E 2002 *Phys. Rev. A* **65** 033405
- [276] Kramers H A 1956 *Collected Scientific Papers* (Amsterdam: North-Holland)
- [277] Mitchell K A, Handley J P, Tighe B, Flower A and Delos J B 2004 *Phys. Rev. Lett.* **92** 073001
- [278] Mitchell K A, Handley J P, Tighe B, Flower A and Delos J B 2004 *Phys. Rev. A* **70** 043407
- [279] Bigie D, Leonard A and Wiggins S 1991 *Nonlinearity* **4** 775
- [280] Mitchell K A, Handley J P, Tighe B, Delos J B and Knudson S K 2003 *Chaos* **13** 880
- [281] Mitchell K A, Handley J P, Delos J B and Knudson S K 2003 *Chaos* **13** 892
- [282] Hansen P, Mitchell K A and Delos J B 2006 *Phys. Rev. E* **73** 066226
- [283] Budyshev M V, Uleysky M Yu and Prants S V 2004 *J. Exp. Theor. Phys.* **99** 1018
- [284] Prants S V, Uleysky M Yu and Argonov V Yu 2006 *Phys. Rev. A* **73** 023807
- [285] Rückler B and Jung C 1994 *J. Phys. A: Math. Gen.* **27** 55
- [286] Rückler B and Jung C 1994 *J. Phys. A: Math. Gen.* **27** 6741
- [287] Lipp C B and Jung C 1995 *J. Phys. A: Math. Gen.* **28** 6887
- [288] Jung C, Lipp C and Seligman T H 1999 *Ann. Phys.* **275** 151
- [289] Easton R W 1986 *Trans. Am. Math. Soc.* **294** 719
- [290] Easton R W 1998 *Geometric Methods for Discrete Dynamical Systems* (Oxford: Oxford University Press)
- [291] Rom-Kedar V 1990 *Physica D* **43** 229
- [292] Rom-Kedar V 1994 *Nonlinearity* **7** 441
- [293] Collins P and Krauskopf B 2002 *Phys. Rev. E* **66** 056201
- [294] Jung C and Seligman T H 1997 *Phys. Rep.* **285** 77
- [295] Chen Q, Ding M and Ott E 1990 *Phys. Lett. A* **145** 93
- [296] Jung C, Merlo O, Seligman T H and Zapfe 2010 *New J. Phys.* **12** 103021
- [297] Sweet D, Nusse H E and Yorke J A 2001 *Phys. Rev. Lett.* **86** 2261
- [298] Sweet D and Ott E 2000 *Phys. Rev. Lett.* **266** 134
- [299] Sweet D, Ott E and Yorke J A 2000 *Physica D* **139** 1
- [300] Wiggins S, Wiesenfeld L, Jaffé C and Uzer T 2001 *Phys. Rev. Lett.* **86** 5478
- [301] Falconer K 1990 *Fractal Geometry: Mathematical Foundations and Applications* (New York: Wiley)
- [302] Morse P M 1929 *Phys. Rev.* **34** 57
- [303] Heagy J and Yuan J M 1990 *Phys. Rev. A* **41** 571
- [304] Lennard-Jones J E 1924 *Proc. R. Soc. A* **106** 463
- [305] Jung C, Merlo O, Seligman T H and Zapfe W P H 2010 *New J. Phys.* **12** 103021